

Modeling, Design and Fabrication of  
Metal-Insulator-Metal Diodes as Rectenna Element  
for Infrared Energy Harvesting and Detection  
Applications

by

Mesut Inac

Submitted to the Graduate School of Engineering and Natural Sciences  
in partial fulfillment of  
the requirements for the degree of  
Master of Science

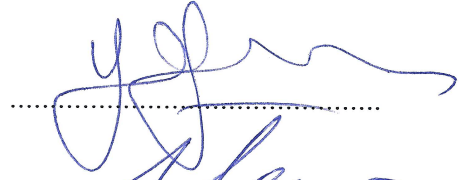
Sabanci University

Summer, 2015

Modeling, Design and Fabrication of Metal-Insulator-Metal Diodes as Rectenna  
Element for Infrared Energy Harvesting and Detection Applications

APPROVED BY

Prof. Dr. Yaşar GÜRBÜZ  
(Thesis Supervisor)



Assoc. Prof. Dr. Meriç ÖZCAN



Asst. Prof. Feysel Yalçın YAMANER



DATE OF APPROVAL: .....03.08.2015.....

© Mesut Inac 2015

All Rights Reserved

## Acknowledgements

During my graduate study, the help and inspirations from many people keep me focused on my studies. This thesis gives me an opportunity to thank the people who helped me during my graduate studies in Sabanci University.

First and foremost, I would like to thank my advisor Prof. Yaşar Gürbüz for his endless support and guidance during my studies. This is a great opportunity to thank him for his patience and confidence in me. I would not be at my current position without his support and motivation.

I would also like to thank to Prof. Meriç Özcan and Prof. Yalçın Yamaner who are serving in my thesis committee in their precious time. I am grateful for their comments and suggestions.

For their help to my work in their valuable time, I would like to thank Prof. Mehmet Ali Gülgün, Prof. Cleva Ow-Yang and Prof. Hüsnü Yenigün who gave me ideas and tricks to be used in modeling and characterization of my samples.

This work is supported by Lockheed Martin University Research Agreement. I would like to thank the Lockheed Martin Team, Dr. Ned Allen, Anthony Jacomb-Hood and Nafiz Karabudak for their suggestions and comments.

I am thankful to my friends Atia Shafique and Elif Gül Özkan for their contribution to this work. I would like to thank my companions in the SU Microelectronics Research group, Dr. Hüseyin Kayahan, Melik Yazıcı, Ömer Ceylan, Emre Özeren, Can Çalışkan, İlker Kalyoncu, Barbaros Çetindoğan, Berktuğ Üstündağ and Divya Mahalingam for creating such a friendly working environment, including the past members. Furthermore, I thank Hasan Kurt, Melike Mercan Yıldızhan and Mustafa Baysal who always listen me and try to answer my questions. I thank the laboratory staff Bülent Köroğlu, Onur Serbest, Cenk Yanık, Ali Kasal and Mehmet Doğan for their help and support. In addition, thanks to Murat Davulcu and many others for your dear friendship during my graduate studies. I would also like to thank İdil Kadioğlu, who always push me towards the best with her interest and love.

Finally, but most importantly, I would like to thank my parents Vicdan and Esat, and my brother Özgür, for their unconditional love, endless support and for always believing in me. I would not come that far without the sacrifices they made.

# Modeling, Design and Fabrication of Metal-Insulator-Metal Diodes as Rectenna Element for Infrared Energy Harvesting and Detection Applications

Mesut Inac

EE, Master's Thesis, 2015

Thesis Supervisor: Prof. Dr. Yaşar GÜRBÜZ

Keywords: Metal-Insulator-Metal (MIM) diode, tunneling, modeling, rectenna, rectenna elements, Infrared (IR) harvesting, Infrared (IR) detection.

## Abstract

Current energy harvesting and detecting devices are lacking of efficiency and they have high fabrication costs. Antenna-coupled rectifiers (rectennas) are one of the most potential candidate for future energy harvesting and detection applications due to their low cost and potential high efficiencies. In the THz region, there is a gap that the speed of the devices cannot cover. Employing THz antennas and Metal-Insulator-Metal (MIM) diodes as rectenna elements can cover the gap and potentially resulting with high efficiency harvesters and detectors. In this thesis, it is presented metal-insulator tunneling diodes as rectenna elements operating at 60 THz to have highly efficient rectennas.

Three THz antennas are modeled and simulated at 60 THz to be used in rectennas in which 95%, 45% and 70% radiation efficiencies over 10 THz bandwidth. MIM diode modeling and simulations are conducted and parametric analysis done to physical properties of MIM structure and found material sets for highly efficient rectennas. MIM diodes are fabricated with these material sets, measured and characterized. It is achieved that 0 V resistance of didoes are 2.3 k $\Omega$ , 3.6 k $\Omega$ , and 35 k $\Omega$ . -6.02 A/W and 5.68 A/W responsivities are reached. Calculated rectenna efficiency when antennas are coupled with fabricated MIM diodes are 12%, 3.5% and 3%.

# Kızılötesi Enerji Hasatı ve Algılama Uygulamaları için Rectenna Elemanlarında Kullanılacak Metal-Yalıtkan-Metal Diyotlarının Modellenmesi, Tasarımı ve Üretimi

Mesut Inac

EE, Yüksek Lisans Tezi, 2015

Tez Danışmanı: Prof. Dr. Yaşar GÜRBÜZ

Anahtar Kelimeler: Metal-Yalıtkan-Metal (MYM) diyot, tünelleme, modelleme, rectenna, rectenna elementleri, Kızılötesi (KÖ) hasatı, Kızılötesi (KÖ) algılama.

## Özet

Günümüz enerji hasatı yapan ve algılayan aygıtların verimlilikleri düşük ve üretim maliyetleri yüksektir. Gelecek enerji hasatı ve algılayıcı teknolojilerinin en öne çıkan adayı, düşük maliyetleri ve potansiyel yüksek verimlilikleri nedeniyle antenle bağlaşıklık doğrultuculardır (rectenna). Elektronik aygıtların THz frekansında çalışmadıklarından bir boşluk bulunmaktadır. Bu boşluğu THz antenler ve Metal-Yalıtkan-Metal (MYM) diyotlar doldurabilecekler ve bu alanda, enerji hasatı ve algılayıcı elemanlarında muhtemel verimlilik artışı sağlayacaklardır. Bu tezde, 60 THz'de çalışacak ve yüksek verimlilikte olacak rectenna elemanları için metal-yalıtkan-metal (MYM) diyotları sunulmaktadır.

Rectenna'larda kullanılmak üzere üç farklı anten 60 THz'de modellenmiş ve simüle edilmiştir, ve bu antenlerde 10 THz bant genişliğinde %95, %45 ve %70 ışınım verimlilikleri görülmüştür. MYM diyotları, modellenmiş, simüle edilmiş, MYM yapısı fiziksel özellikleri üzerine parametrik analizleri yapılmış, ve yüksek verimli rectenna için malzeme setleri bulunmuştur. MYM diyotları bu malzeme setlerinden üretilmiş, ölçümleri yapılmış ve özellikleri nitelendirilmiştir. Bu diyotlarda, 0V direnci olarak 2.3 k $\Omega$ , 3.6 k $\Omega$ , ve 35 k $\Omega$  dirençler gözlenmiş, -6.02 A/W ve 5.68 A/W duyarlılıklara ulaşılmıştır. Antenler MYM diyotlarıyla bağlaştırılıp rectenna verimliliği hesaplandığında %12, %3.5 ve %3 verimlilik değerlerine ulaşılmıştır.

# Contents

<b>Acknowledgements</b>	<b>iv</b>
<b>Abstract</b>	<b>v</b>
<b>Table of Contents</b>	<b>vii</b>
<b>List of Figures</b>	<b>ix</b>
<b>List of Tables</b>	<b>xii</b>
<b>List of Abbreviations</b>	<b>xiii</b>
<b>1 Introduction</b>	<b>1</b>
1.1 Rectenna . . . . .	1
1.2 A Brief History of Rectenna . . . . .	1
1.3 Antennas . . . . .	2
1.4 Antenna Operation . . . . .	4
1.5 Rectifiers . . . . .	7
1.6 MIM Diode Operation . . . . .	9
1.6.1 Electrical MIM Diode Characteristics . . . . .	10
1.6.2 MIM Circuit Model . . . . .	11
1.7 Rectenna Circuit, Efficiency and Limits . . . . .	12
1.7.1 Rectenna Circuit . . . . .	12
1.7.2 Rectenna Efficiency . . . . .	13
1.7.3 Rectenna Efficiency Limits . . . . .	13
1.8 Motivation . . . . .	14
1.9 Organization . . . . .	15
<b>2 Modeling and Simulations</b>	<b>17</b>
2.1 Antenna Design and Simulations . . . . .	17
2.1.1 Half-Wave Dipole Antenna . . . . .	17
2.1.2 Bow-tie Antenna . . . . .	19
2.1.3 Modified Dipole Antenna . . . . .	21
2.2 Metal-Insulator-Metal Diode Modeling and Simulations . . . . .	23
2.2.1 Tunneling Current . . . . .	24
2.2.2 Transfer Matrix Method (TMM) . . . . .	27
2.2.3 Effective Barrier Height . . . . .	30
2.2.4 MIM Diode Simulation Results . . . . .	31
2.3 Rectenna Simulations and GUI . . . . .	37
<b>3 Fabrication</b>	<b>40</b>
3.1 Detailed Fabrication Procedure . . . . .	40
3.1.1 Substrate Cleaning . . . . .	41
3.1.2 Electron Beam Lithography . . . . .	41
3.1.3 Material Deposition . . . . .	44
3.2 Lithography Masks . . . . .	47

<b>4</b>	<b>Measurements and Characterization</b>	<b>52</b>
4.1	Measurement Setup . . . . .	52
4.2	Electrical DC Measurements . . . . .	53
4.2.1	MM1 Measurement Results . . . . .	53
4.2.2	MM2 Measurement Results . . . . .	54
4.2.3	MM5 Measurement Results . . . . .	55
4.2.4	LM1 Measurement Results . . . . .	56
4.2.5	LM2 Measurement Results . . . . .	56
4.2.6	LM3 Measurement Results . . . . .	58
4.2.7	LM4 Measurement Results . . . . .	58
4.2.8	LMC Measurement Results . . . . .	59
4.3	Electrical DC Characteristics . . . . .	60
4.3.1	Resistance . . . . .	60
4.3.2	Non-linearity . . . . .	62
4.3.3	Responsivity . . . . .	63
4.4	Efficiency Calculations . . . . .	64
<b>5</b>	<b>Conclusion &amp; Future Work</b>	<b>66</b>
5.1	Summary of Work . . . . .	66
5.2	Future Work . . . . .	67
	<b>References</b>	<b>68</b>
	<b>Appendices</b>	<b>72</b>
A1	MATLAB Diode Model . . . . .	72
A1.1	MATLAB Transfer Matrix Method . . . . .	74
A1.2	MATLAB Effective Potential Barrier Calculation . . . . .	76

# List of Figures

1	Schematic representation of antenna-coupled rectifier (rectenna) . . .	2
2	Microwave powered helicopter in demonstration, 1964 . . . . .	3
3	Different type of planar antennas (a) dipole (b) bow-tie (c) log-periodic (d) patch (e) microstrip slot (d) spiral antennas . . . . .	4
4	Energy Band diagram of MIM diode and electron tunneling . . . . .	8
5	Energy band diagram comparison of (a) symmetric MIM diode and (b) asymmetric MIM diode . . . . .	10
6	Circuit model of a MIM diode . . . . .	12
7	Circuit model of a rectenna . . . . .	13
8	Theoretical efficiency limits . . . . .	14
9	Designed half-wave dipole antenna in HFSS environment . . . . .	17
10	Simulations result of half-wave dipole antenna in Fig. 9. (a) impedance matching, (b) antenna impedance (c) radiation efficiency . . . . .	18
11	Designed bow-tie antenna in HFSS environment . . . . .	19
12	Simulations result of bowtie antenna in Fig. 11. (a) impedance match- ing, (b) antenna impedance (c) radiation efficiency . . . . .	20
13	Designed first modified dipole antenna in HFSS environment . . . . .	21
14	Simulations result of modified dipole antenna in Fig. 13. (a) impedance matching, (b) antenna impedance (c) radiation efficiency . . . . .	22
15	MATLAB algorithm diagram of MIM tunneling diode current calcu- lation . . . . .	24
16	Potential barrier is divided to n subdivisions for TMM . . . . .	28
17	Tunneling probability of the MIM diode according to TMM method at different applied voltages. MIM have $d = 2.5$ nm, $K = 10$ , $\phi_l = 3$ eV, $\phi_r = 5$ eV and $E_{F,l} = 10$ eV . . . . .	31
18	Tunneling probability of the MIM diode according to TMM method at different insulator thicknesses. MIM have $V_{appl} = 0^+$ V, $K = 10$ , $\phi_l = 3$ eV, $\phi_r = 5$ eV and $E_{F,l} = 10$ eV . . . . .	32
19	Tunneling probability of the MIM diode according to TMM method at different insulator dielectric constants. MIM have $d = 2.5$ nm, $V_{appl} = 0^+$ V, $\phi_l = 3$ eV, $\phi_r = 5$ eV and $E_{F,l} = 10$ eV . . . . .	33
20	Barrier according to the Fermi level of the left metal, barrier heights and image forces is shown. MIM have $d = 2.5$ nm, $K = 10$ , $\phi_l = 3$ eV, $\phi_r = 5$ eV and $E_{F,l} = 10$ eV . . . . .	34
21	Current density and thickness of the barrier relation. MIM have $V_{appl} =$ $0^+$ V, $K = 10$ , $\phi_l = 3$ eV, $\phi_r = 5$ eV and $E_{F,l} = 10$ eV . . . . .	35
22	Barrier formation of MIM structures (a) $Au - AlOx - Al$ (b) $Au -$ $AlOx - Cr$ (c) $Au - CrOx - Cr$ (d) $Au - TiOx - Ti$ . . . . .	36
23	Current density of MIM structures $Au - AlOx - Al$ , $Au - AlOx - Cr$ , $Au - CrOx - Cr$ , and $Au - TiOx - Ti$ . . . . .	37
24	Rectenna GUI main screen - physical and simulation paramters input	38
25	GUI screen-shot while antenna simulations . . . . .	38
26	The output of GUI. (a) S11 vs. frequency (b) Antenna impedance vs. frequency (c) Tunneling probability vs electron energy (d) Diode $I - V$ characteristic . . . . .	39

27	Flow-charts of fabrication procedure (a) flow of three layers fabrication step (b) cross section representation of substrate in a fabrication cycle . . . . .	40
28	Electron beam lithography (EBL) system in Sabanci Univeristy SUNUM cleanroom facilities . . . . .	42
29	Spin coating equipment and materials for laying resist in yellow-room	43
30	Sample after development under light microscopy. Patch on the right hand side is metal-1 of MIM diode, and the patch on the left hand side is developed area. Other pars are PMMA resist. . . . .	44
31	PVD system in cleanroom. (a) Photo of PVD system and electrical controls (b) deposition chamber and electron and heat sources of PVD system . . . . .	45
32	Samples while lift-off process . . . . .	46
33	MIM diodes after fabrication (a) batch of MIM diodes and pads (b) MIM diode overlap;Scanning Electron Microscope (SEM) images of MIM diodes (a) single MIM diode (b) antenna coupled MIM diode . .	46
34	Mask 1: (a) pads and markers are visible (b) connection line overlaps $0.2121 \mu\text{m} \times 0.2121 \mu\text{m}$ with the metal on the right side. . . . .	50
35	Mask 2: (a) pads and markers are visible (b) connection line overlaps $0.46 \mu\text{m} \times 0.46 \mu\text{m}$ with the metal connection on the right side. . .	51
36	Mask 3: (a) pads and markers are visible (b) connection line overlaps $1.3 \mu\text{m} \times 0.5 \mu\text{m}$ with the metal connection on the right side. . . . .	51
37	Measurement setup (a) EM shielded black box in the middle and semiconductor parameter analyzer on the right (b) DC needle probes	52
38	$I - V$ characteristics of MM1: $Al/Al_2O_3/Cr/Au$ , 2 nm insulator thick MIM diode, measurement is on the left scale and the simulations are on the right scale . . . . .	53
39	$I - V$ characteristics of MM2: $Al/Al_2O_3/Cr/Au$ , 5 nm insulator thick MIM diode, measurement is on the left scale and the simulations are on the right scale . . . . .	54
40	$I - V$ characteristics of MM5: $Au/Al_2O_3/Al$ , 5 nm insulator thick MIM diode, measurement is on the left scale and the simulations are on the right scale . . . . .	55
41	$I - V$ characteristics of LM1: $Au/Cr_2O_3/Cr$ , 5 nm insulator thick MIM diode, measurement is on the left scale and the simulations are on the right scale . . . . .	57
42	$I - V$ characteristics of LM2: $Au/TiO_2/Ti$ , 5 nm insulator thick MIM diode, measurement is on the left scale and the simulations are on the right scale . . . . .	57
43	$I - V$ characteristics of LM3: $Au/Al_2O_3/TiO_2/Ti$ , 2.5/2.5 nm insulator thick MIIM diode. MIIM type of diode simulations are not available . . . . .	58
44	$I - V$ characteristics of LM4: $Au/Al_2O_3/Cr$ , 5 nm insulator thick MIM diode, measurement is on the left scale and the simulations are on the right scale . . . . .	59
45	$I - V$ characteristics of LMC: $Cr/Cr_2O_3/TiO_2/Ti$ , 2.5/2.5 nm insulator thick MIIM diode. MIIM type of diode simulations are not available . . . . .	60

46	Resistance graph of lowest four resistive fabricated MIM diodes . . .	61
47	Non-linearity graph of lowest four resistive fabricated MIM diodes . .	62
48	Responsivity graph of lowest four resistive fabricated MIM diodes . .	63

## List of Tables

1	Calculated conductivity of gold at THz frequencies . . . . .	6
2	State of the are MIM diode responsivity and resistances . . . . .	9
3	Spin coating parameters . . . . .	43
4	Deposition parameters . . . . .	48
5	Fabricated MIM diodes . . . . .	49
6	Fabricated MIM diode characteristics and calculated efficiencies . . .	65

## List of Abbreviations

<b>AC</b>	Alternating Current
<b>ACE</b>	Acetone
<b>AFM</b>	Atomic Force Microscopy
<b>ALD</b>	Atomic Layer Deposition
<b>BW</b>	Band Width
<b>CIC</b>	Conductor-Insulator-Conductor
<b>DC</b>	Direct Current
<b>DUT</b>	Device Under Test (unit)
<b>EBL</b>	Electron Beam Lithography
<b>EM</b>	Electro-Magnetic
<b>FIR</b>	Far-infrared
<b>GUI</b>	Graphical User Interface
<b>I-V</b>	Current-Voltage
<b>IPA</b>	Isopropyl Alcohol
<b>IR</b>	Infrared
<b>MIBK</b>	Methyl-isobutyl-ketone
<b>MIIM</b>	Metal-Insulator-Insulator-Metal
<b>MIM</b>	Metal-Insulator-Metal
<b>PEC</b>	Proximity Effect Correction
<b>PMMA</b>	Poly-methyl-metacrylate
<b>PVD</b>	Physical Vapor Deposition
<b>Rectenna</b>	Antenna-coupled rectifier
<b>RF</b>	Radio Frequency
<b>SEM</b>	Scanning Electron Microscope
<b>TEM</b>	Transmission Electron Microscope
<b>TMM</b>	Transfer Matrix Method
<b>WKB</b>	Wentzel–Kramers–Brillouin (approximation)

# 1 Introduction

## 1.1 Rectenna

Detailed research have being conducted and new concepts have being tried for the next generation energy collection and sensing devices [1]. Cost effective and highly efficient new generation solar and thermal energy collectors have being studied [2]. New concepts and materials bring the efficiency of these devices to thermodynamic energy conversion limits. Similar concepts and materials have being studied on sensing devices and detectors [3]. Cost effectiveness and efficiency of these devices are main concerns for both of collectors and detectors.

Antenna-coupled rectifier (rectenna) is one of the most promising candidate for future energy harvesting [4] and detection [5] applications. Rectenna is basically an antenna and a rectifier coupled to each other, which is shown in Fig. 1. Rectennas operate at any frequency where both of the antenna and rectifier operate. Hence, rectenna can be configured to single or broad-range frequency operation according to application specifications [6]. Additionally, batch fabrication of rectenna arrays would have lower cost [7].

Rectennas basically operate through the conversion of electromagnetic (EM) radiation to usable direct current (DC). First, incident EM radiation induces alternating current (AC) in the antenna arms, then AC is converted to DC by a rectifier which is positioned right on the antenna arms. The circuit elements connected to the load in Fig. 1 determine whether the rectenna acts as a detector or as an energy harvester. Recent developments in rectennas aim to fill the gap in the THz region [8, 9]. Operation in the THz region requires micron level antennas and high-speed diodes. Nanolithographic antennas and metal-insulator tunneling diodes, also known as metal-insulator-metal (MIM) diodes, capable of operating at high frequencies, are used in THz rectennas.

## 1.2 A Brief History of Rectenna

Early rectennas were developed and tested in 1963 at Raytheon by W. C. Brown [10]. Rectenna is based on the idea of wireless transmission of microwave power. In 1964 it was demonstrated that rectennas can be used as energy harvesters. A

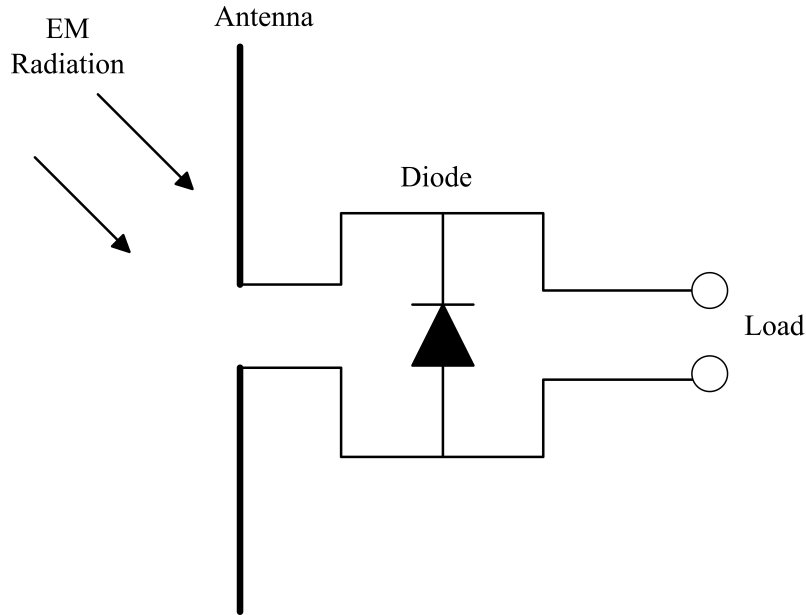


**Figure 1:** Schematic representation of antenna-coupled rectifier (rectenna)

microwave power helicopter in Fig. 2, which flew continuously 10 hours and meters above transmitting antenna, received and converted microwave power to DC power by rectenna elements. Later in 1970s rectenna power transmission demonstrated greater than 90% efficiency at radio frequencies (RF) [11].

Advances in the lithography and material deposition techniques allowed nano device fabrication in 1990s. This advance created a possibility to further the operation frequencies of rectennas. Research on the improvement of antenna characteristics in far-infrared (FIR) [12] and THz [13] region of EM spectrum was conducted. Nanometer thin film MIM diodes for detection [14] and energy harvesting applications [15] were investigated along antennas.

After the 1990s, the research mainly focused on increasing rectenna speed to THz frequencies. Experiments were conducted to improve the MIM diode characteristics [16] and use them in rectenna detectors [17] and solar energy harvesters [18]. Since then, scientists and engineers have almost reached the end of the road in closing the THz gap with rectennas.

### 1.3 Antennas

Antennas collect the EM radiation and convert them into electrical signals in rectennas. The operation frequency depends strongly on antenna operation since

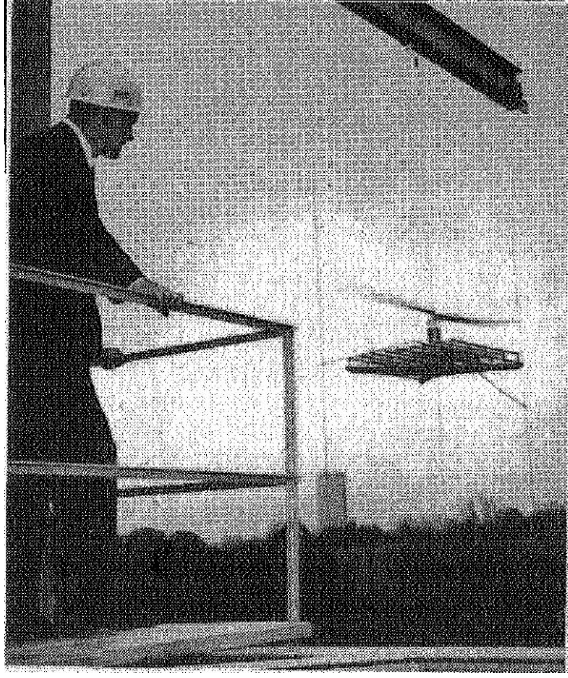


**Figure 2:** Microwave powered helicopter in demonstration, 1964 [11]

it sets the center frequency of operation in rectennas. Additionally, the power collected on the antenna affects the output power following rectification. Hence, in high frequency operations the requirement of precise fabrication in nanometer scale and conversion quality of incident power are challenging factors in development of antennas [1].

Planar antennas are easy to fabricate and couple with diodes. Directive dipole antennas [19] and wide bandwidth (BW) bow-tie antennas [8] are the most commonly used antennas. Log-periodic antenna [20], patch antenna [21] and spiral antenna [13] are used in applications that require tailored BW. In addition to the ones listed above, other novel antenna concepts have been demonstrated. For dual band rectenna detectors, microstrip slot antenna [22] has been shown to operate at 90 GHz and 28 THz. Plasmonic nanowires [23] have been used because of their controllable growth and property on enhancing electric field at the feed-point. Some of the antenna types used in rectennas are shown in Fig. 3.

In order to increase the rectenna total efficiency and operating frequency band, antenna arrays [24] were implemented. Array formation also allows to have different antenna-diode coupling techniques. In single element (antenna + rectifier) rectenna, signals collected by the antenna are not enough to turn on the rectifiers [25]. In this case, array of an antennas is connected to single rectifier to turn on the diodes or

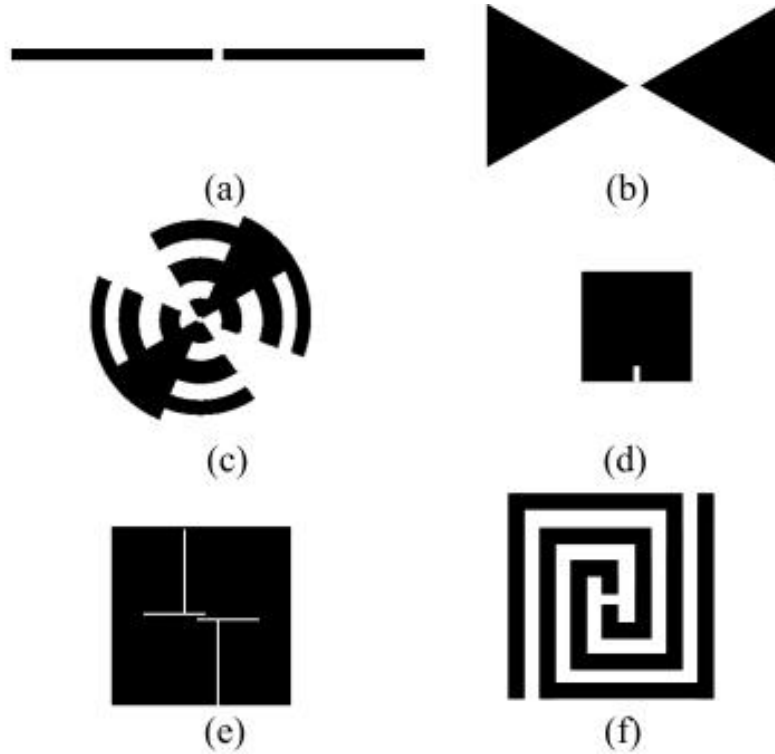


**Figure 3:** Different type of planar antennas (a) dipole (b) bow-tie (c) log-periodic (d) patch (e) microstrip slot (f) spiral antennas

operate the diode at most efficient voltage point.

Besides the planar antennas, advanced micromachining techniques enable designing 3-D antennas. Employment of 3-D antennas provides unidirectionality like 3-D tapered helix [26] structures and higher collection efficiency like pillar arrays [27].

It is important to select the antenna in the application of IR energy harvesting and detection applications. According to the literature listed above, half-wave dipole and bow-tie antennas are the most promising candidates in this field due to their simple fabrication, and highly efficient band coverage.

## 1.4 Antenna Operation

It is required an antenna to couple with incident EM radiation in IR rectennas due to the sizes of MIM diodes are much smaller than the wavelengths. Connecting diodes with antennas increase the coupling of EM radiation with the rectifier. The voltage drop across the antenna arms where MIM diodes are connected to antennas, is important for the operation of MIM diode. It is determined for MIM diode

that if the voltage across the antenna arms is higher than turn-on voltage or lower. Therefore, it directly affects diode characteristics line resistance and responsivity of diode.

The collection efficiency and the voltage drop across the antenna arms are connected to each other. According to reciprocity theorem, the receiving parameters of antenna is same for transmitting antenna [28] therefore antenna collection efficiency is:

$$\eta_a = \frac{P_{rad}}{P_{Tot}} = \frac{P_{rad}}{P_{rad} + P_{loss}} \quad (1)$$

where  $\eta_a$  is antenna efficiency,  $P_{rad}$  is radiated power,  $P_{Tot}$  is total injected power in to the antenna and  $P_{loss}$  is the lost power due to impedance of the antenna. For the maximum antenna collection efficiency, losses due to the impedance of the antenna have to be decreased. In order to decrease the losses on the antenna, the resonance frequency of the antenna has to be set to operating frequency. Therefore, for monochromatic applications, the possibility of having efficient antenna is more than wide BW applications.

Beside the antenna impedance loss in IR frequencies due to the electronic oscillations, there is another loss mechanism. Electrons in a materials cannot keep up with the oscillations close to their intrinsic plasma frequency [29]. It is calculated by:

$$\sigma = j\omega\varepsilon_0(\varepsilon_r - 1) \quad (2)$$

where  $\sigma$ ,  $j$ ,  $\omega$ ,  $\varepsilon_0$ ,  $\varepsilon_r$  represent conductivity, complex number, angular frequency, vacuum permittivity and relative permittivity respectively. For example, while gold bulk DC conductivity is  $45 \times 10^6$  S/m, at 500 THz it is calculated as  $5.3 \times 10^5$  which is 85 fold lower than the DC conductivity of gold. Table 1 shows the conductivity of gold in THz frequencies. The classification of good conductor for a material done by calculating [25]:

$$\psi = \frac{\sigma}{\omega\varepsilon_0} \quad (3)$$

and if  $|\psi| \gg 1$ , then the material is accepted as good conductor. Thus, careful

**Table 1:** Calculated conductivity of gold at THz frequencies [25]

Frequency (THz)	$ \sigma $	$ \psi $
1	$4.05 \times 10^7$	$7.29 \times 10^5$
10	$2.2 \times 10^7$	$4 \times 10^4$
30	$8.63 \times 10^6$	$5.17 \times 10^3$
70	$3.77 \times 10^6$	968.4
100	$2.64 \times 10^6$	475.55
500	$5.3 \times 10^5$	19

material selection of antenna is required for operating at IR frequencies. Once electrons are capable of oscillating at operating frequencies, than there is enough electrons to rectify the signal, otherwise the voltage drop on the antenna arms will cease to exist.

The voltage drop on the antenna arms is calculated according to [30] as first relating incident power ( $P_{inc}$ ) and incident electric field ( $E_{rms}$ ):

$$\zeta = \frac{P_{inc}}{A} = \frac{E_{rms}^2}{Z_0} = \frac{E_p^2}{2Z_0} \quad (4)$$

where  $\zeta$  is Poynting vector which is time averaged incident radiation,  $A$  is antenna aperture area and  $Z_0$  is impedance of the free space which equals to  $377\Omega$ . The relation of voltage across antenna arms ( $V_A$ ) and incident electric field peak ( $E_p$ ) is simply dependent on the effective antenna length ( $L_{eff}$ ):

$$V_A = L_{eff}E_p \quad (5)$$

The effective antenna length is stated as [28]:

$$L_{eff} = L_{ant} \sin(\theta) \quad (6)$$

where  $L_{ant}$  is antenna length and  $\theta$  is the angle between antenna plane and the incident wave. Assuming the incident EM radiation is at direct angle to the antenna plane ( $\theta = 90^\circ$ ) then  $L_{eff}$  is equal to  $L_{ant}$ . If (4) and (6) are introduced in to (5), voltage drop at the antenna arms can be stated as:

$$V_A = \sqrt{\frac{2P_{inc}Z_0L_{ant}^2}{A}} \quad (7)$$

It is important to understand that this is antenna open voltage at the antenna arms without connecting any diode. Other than that, the only parameter for the antenna to model is the geometric dimensions of antenna which is seen from (7). While the free space impedance is constant and the incident radiation is a variable for the application, the antenna collection efficiency only depend on the effective antenna length and antenna aperture area. Therefore, it can be re-stated that the efficiency of the antenna is:

$$\eta_a\eta_s = \frac{L_{ant}^2}{A} \quad (8)$$

where  $\eta_s$  is efficiency factor of loss because of the high frequency factors like conductivity change. Then inserting (8) to (7) gives:

$$V_A = \sqrt{2P_{inc}Z_0\eta_a\eta_s} \quad (9)$$

Relation between voltage drop on antenna arms, incident power and antenna efficiency is shown in (9). Due to the efficiency factor in the equation, antennas perform differently. Besides that, the power collected by the antenna is divided between antenna and diode according to their impedances. Therefore, impedance is other parameter to be considered while designing antennas which is not seen in the equations above. Therefore, there are three properties of antenna to be considered: resonance frequency, antenna efficiency and antenna impedance.

## 1.5 Rectifiers

After antenna collects EM radiation from a media and induce an AC electrical signal, rectifier converts AC signal to DC. The basic rectifier to convert AC signal to DC is only a diode. Due to the asymmetry of diode, it generates DC at the output. According to the performance of diode, the rectification efficiencies and the rectification frequency changes. In order to rectify AC signal at high frequencies, it is required to have a THz frequency-cut-off diode. Metal-insulator tunneling diode, or in another words metal-insulator-metal (MIM) diodes are capable to operate at

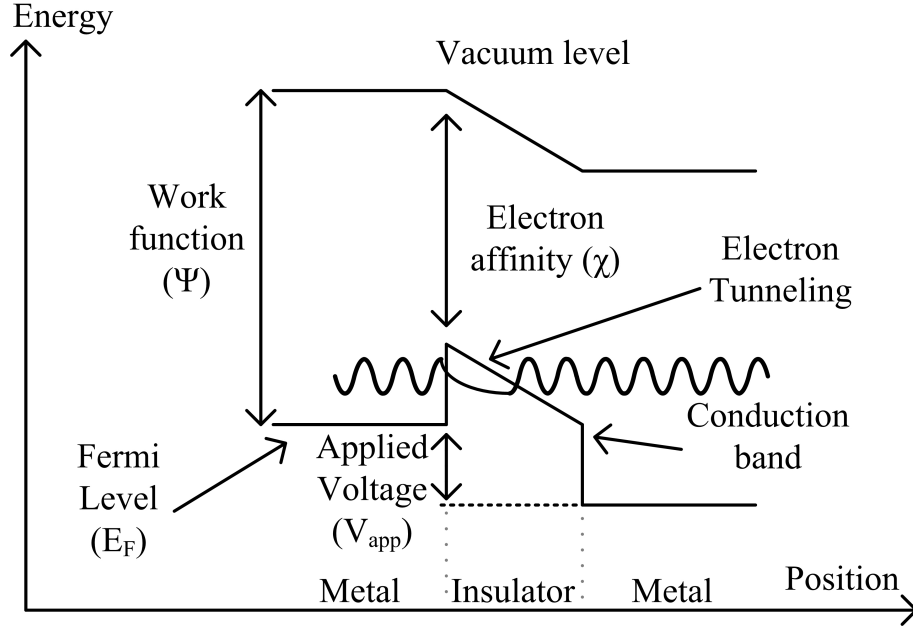


**Figure 4:** Energy Band diagram of MIM diode and electron tunneling

THz frequencies [4].

MIM diodes are fast diodes due to the electron tunneling phenomenon. The operating speed of the diodes are in the order of femto-second fast quantum tunneling mechanisms [6]. The non-linear current-voltage (I-V) characteristics of the MIM diodes occur due to the energy barrier formation at the insulator layer. The energy band diagram of MIM diodes can be seen in Fig. 4.

Engineering I-V characteristics of MIM diodes plays very crucial part in rectennas. Because for the maximum power transfer, the antenna and the MIM diode impedances have to be matched and diode capable of rectifying incoming signal. In order to satisfy the needs, engineering of I-V characteristics of the MIM diode basically done by choosing the right material combination and the geometrical parameters [31].

The characteristics of the MIM diode can be changed according to the material selection [32]. According to the material selection in MIM diode, the asymmetry and the turn-on voltage can be adjusted. Additionally, thickness of the insulator film is also an important parameter determines the tunneling probability and therefore MIM diode characteristics [17]. Not only thickness of the insulator layer, but also the surface roughness affects the MIM diode characteristics [33]. The fabrication of insulator layer can directly effect the MIM diode characteristics. It is shown that

the oxidation parameters of insulator film [34] and annealing of insulator film [35]. Resistance and responsivity characteristics of state-of-the-art MIM diodes are shown in Table 2.

**Table 2:** State of the are MIM diode responsivity and resistances

Ref.	MIM Type	MIM Area	Insulator Thickness	0 V Resp.	Max. Resp.	0V Resist.
		$[\mu\text{m}^2]$	[nm]	$[\text{V}^{-1}]$	$[\text{V}^{-1}]$	$[\Omega]$
[22]	Ni-NiO-Ni	0.075	3.5	–	1.65	179.8
[5]	Ni-NiO-Ni	0.0144	3.5	–	2.75	61
[32]	polySi-SiO <sub>2</sub> -polySi	$60 \times 10^{-6}$	1.38	–	6	–
[32]	polySi-SiO <sub>2</sub> -Au	0.35	1.38	2.5	-14.5	120 M
[36]	planar-polySi	$60 \times 10^{-6}$	1.38	12	31	–
[37]	Ni-NiO-Cr	1	2.5	1	7	–
[35]	Ni-NiO-Cr	100	3	24	42	–
[7]	Ni-NiO-Cr	1	2.5	1.8	5	500 k
[8]	Cu-CuO-Au	0.0045	0.7	4	6	505
[34]	Al-AlO <sub>x</sub> -Pt	0.5325	0.6	0.5	-2.3	220 k

MIM diodes are the most common diodes in rectennas, but also planar conductor-insulator-conductor (CIC) diodes [36], substrate micromachined MIM diode [37] and graphene geometric diode [38] are demonstrated in rectennas. In addition, metal-double insulator tunneling diodes or in another words metal-insulator-insulator-metal (MIIM) diodes were proposed in rectennas [18].

## 1.6 MIM Diode Operation

In MIM diodes, rectification occurs due to the tunneling phenomenon. The main transport mechanism in MIM diodes is tunneling. Due to the difference of tunneling probability of electron with respect to the applied voltage, linearity of the device is broken. This non-linear behavior is the reason of the rectification in these devices.

There are two different MIM diodes: symmetric and asymmetric. The difference is due to the metals on the both sides are similar [39] or dissimilar [31]. The dissimilarity of metals change the barrier heights on the both sides of the insulator

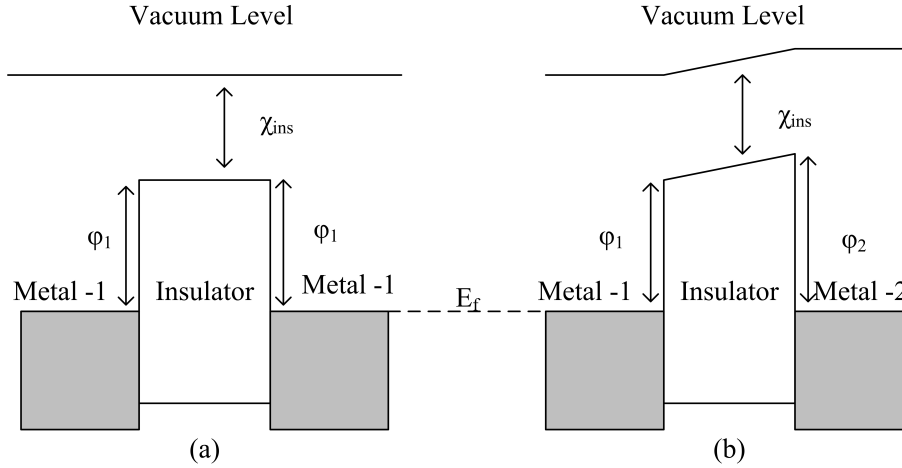


**Figure 5:** Energy band diagram comparison of (a) symmetric MIM diode and (b) asymmetric MIM diode

barrier. Because the Fermi level ( $E_F$ ) of metals are different and they have to be in equilibrium in short circuited position. This relation can be seen in the Fig 5. Symmetric MIM diodes show symmetric I-V characteristics while asymmetric MIM diodes show asymmetric I-V characteristics. That asymmetric behavior is the reason of MIM diodes rectifies. The shape of the asymmetric MIM diodes caused by three factors: Energy barrier-1 ( $\phi_1$ ) which is formed at metal-1 and insulator junction, energy barrier-2 ( $\phi_2$ ) which is formed at insulator and metal-2 junction and electron affinity ( $\chi_{ins}$ ) of insulator layer. In Fig 5, these factors can be seen.

Applied voltage to one side of the MIM diode increases the  $E_F$  of that side which disturbs the equilibrium. There is a energy difference between full electronic states where the voltage applied and empty states at other metal. If the energy difference between these two state is enough for an electron to tunnel thorough insulator energy barrier, than the electron tunnel through as in Fig. 4. As applied voltage increases, number of electrons that tunnel though the barrier increases. This is why the system shows diode behavior.

### 1.6.1 Electrical MIM Diode Characteristics

The MIM diode characteristics which is shown in Table 2, are extracted from measured current-voltage ( $I - V$ ) characteristics of MIM diode.

There are three basic characteristics extracted from I-V of MIM diodes, which are resistance, non-linearity and responsivity. Hence, diode characteristics, resis-

tance ( $R_D$ ), non-linearity ( $I''$ ) and responsivity ( $S$ ), are extracted as following [30]:

Resistance;

$$R_D = \frac{dV_D}{dI_D} \quad (10)$$

and, non-linearity;

$$I'' = \frac{d^2 I_D}{dV_D^2} \quad (11)$$

and responsivity;

$$S = \frac{d^2 I_D / dV_D^2}{dI_D / dV_D} = R_D I'' \quad (12)$$

These are the characteristics of a MIM diode. It is important to remember that all of the current and characteristics are electrical DC characteristics under no light or extreme temperatures that can contribute to tunneling or electrical current.

### 1.6.2 MIM Circuit Model

MIM diodes are nonlinear devices unlike resistors. While investigating MIM diodes in higher frequencies, a circuit model is required. From the starting point of building diode circuit model, it has to be considered that at the the model should give diode characteristics. Hence, starting point of the first order MIM diode circuit model is a variable resistor ( $R_D$ ). At very low frequencies, a simple variable resistor is enough. But at high frequencies, the diode reach its cut-off frequency ( $f_c$ ). Additionally, MIM structure is a simply parallel plate capacitor. Therefore, there should be a capacitor ( $C_D$ ) parallel to resistor. The final result can be seen in the Fig. 6.

In this model,  $f_c$  of the diode can be extracted. The cut-off frequency of the diode will be [25]:

$$f_c = \frac{1}{2\pi R_D C_D} \quad (13)$$

where  $C_D$  is parallel plate capacitor which is given by:

$$C_D = \frac{\epsilon_r \epsilon_0 A}{d} \quad (14)$$

In (14),  $\epsilon_r$  represent relative permittivity of insulator layer,  $\epsilon_0$  represents per-

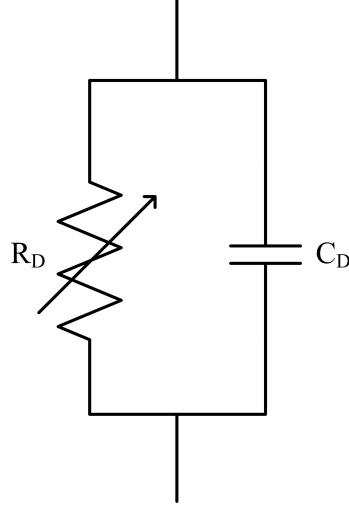


**Figure 6:** Circuit model of a MIM diode

mittivity of free space,  $A$  represents area of the MIM diode and  $d$  represents the distance between metal plates which is insulator thickness.

## 1.7 Rectenna Circuit, Efficiency and Limits

### 1.7.1 Rectenna Circuit

After all the parts connected to each other, circuit model of a rectenna developed as in Fig. 7. At DC, capacitor behaving like open circuit, leaving resistances  $R_A$  and  $R_D$ . For maximum power transfer  $R_A$  must be equal to  $R_D$ . As it is mentioned before, the importance of the impedance matching has been also seen here.

The voltage on the diode is basically found by a voltage division [40]:

$$V_D = \frac{R_D}{R_A + R_D} V_A \quad (15)$$

Then the power on the diodes becomes:

$$P_D = \frac{V_D^2}{R_D} = \frac{R_D}{(R_A + R_D)^2} V_A^2 \quad (16)$$

Now on the circuit, every node voltage and current can be calculated. Therefore the calculation of rectenna efficiency can be done easily.

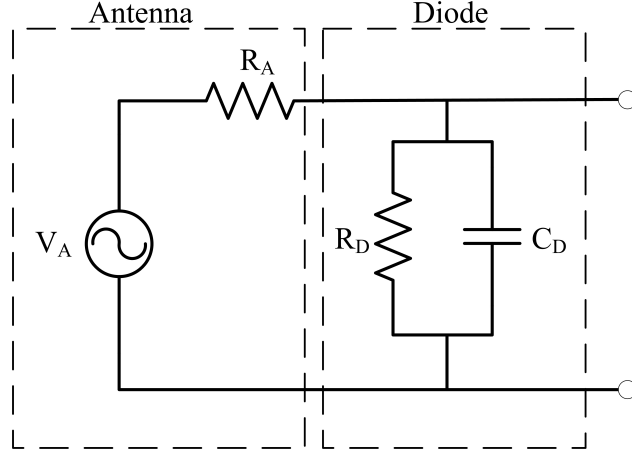


**Figure 7:** Circuit model of a rectenna

### 1.7.2 Rectenna Efficiency

Rectenna efficiency simply stated as the ratio of incident power to power dissipated by the diode. Additionally, in the rectification, the quantum efficiency ( $\eta_q$ ) of the diode has to be considered. Hence rectenna efficiency will be [30]:

$$\eta = \frac{P_D}{P_{inc}} \eta_q \quad (17)$$

If (16) and (9) introduced into (17), then the equation becomes:

$$\eta = \frac{Z_0 \eta_a \eta_s R_D}{(R_A + R_D)^2} \times \frac{\hbar \omega}{e} \times S \quad (18)$$

where;

$$\eta_q = \frac{1}{2} \frac{\hbar \omega}{e} S \quad (19)$$

Efficiency of rectenna is shown in (18). In this equation, contributions from antenna part antenna efficiency and antenna impedance while contributions from diode are diode resistance and responsivity. Generally MIM diodes resistance is more than antenna resistance. If  $R_D \gg R_A$ , then efficiency equation is simplified to coefficients times  $S/R_D$  which is equal to non-linearity of diode from (12).

### 1.7.3 Rectenna Efficiency Limits

Even though it is said to there could be more than 90% of efficiency of rectennas [4], still the device has to obey thermodynamic efficiency limitations. The first

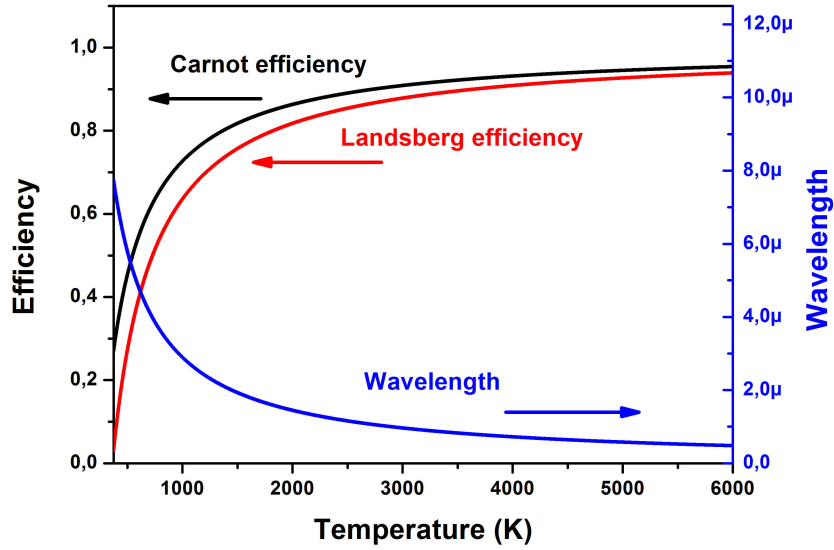


**Figure 8:** Theoretical efficiency limits

efficiency that has to be considered is Carnot Efficiency [41]:

$$\eta_{Carnot} = 1 - \frac{T_C}{T_H} \quad (20)$$

where  $T_C$  is the temperature of the cooler reservoir and  $T_H$  is the temperature of the warmer reservoir. In rectenna case, assuming the IR radiation is coming from a hot source, then rectenna's which is probably operating at room temperature, temperature is  $T_C$  and the source's temperature is  $T_H$ .

Another efficiency theoretical efficiency limit is the Landsberg efficiency [42]:

$$\eta_{Landsberg} = 1 - \frac{4}{3} \left( \frac{T_0}{T_1} \right) + \frac{1}{3} \left( \frac{T_0}{T_1} \right)^4 \quad (21)$$

where  $T_0$  is device temperature and  $T_1$  is source temperature. In Fig. 8 theoretical limitations and the wavelength equivalent of temperature can be seen.

## 1.8 Motivation

There are energy harvesting and detection applications of rectennas and they are shown as future technology in energy harvesting and detection applications. As it mentioned previous section, there are different designs for rectennas operating at high frequencies. There is a requirement of detailed search on both antenna and

rectifier front. In the antenna front, scaling down of antennas meets the minimum requirement for the applications. THz frequencies can be covered by these antennas. Additionally, in rectifier front, it is seen that MIM type of devices are solution for fast operations. Improving efficiency of rectenna requires femtosecond fast operation of diode, fine impedance matching between antenna and diode, and good electrical characteristic of diode. All of these concerns are tightly connected to each other and fine optimizations are required in modeling, designing and fabrication of these diodes in THz operations.

The objective of this thesis is model, design and characterize new MIM diodes for highly efficient THz rectennas. First, it is aimed to develop a MIM diode model to be used in rectennas. It is important to use a model to optimize material sets and geometric parameters for the MIM diode as a starting point of development of rectennas. Electrical characteristics of MIM diode can be extracted from the model and according to the characteristics of MIM diode, rectenna design and fabrications can be started. Secondly, characterizing the fabricated MIM diodes which are designed in light of the model developed is conducted. By this methodology, it is aimed to overcome the limitations of MIM to acquire higher efficiencies in IR rectennas.

## **1.9 Organization**

Chapter 2 shows the concepts of building rectenna model and simulation setup. In this chapter, antennas are simulated in commercial EM-solver separately. A MIM simulator is set up in MATLAB environment where electrical behavior analysis of MIM diodes were completed. a graphical user interface (GUI) is introduce to facilitate rectenna simulations.

In chapter 3, fabrication methods and steps of MIM diodes are presented. The equipment that are used in the fabrication steps are shown and the parameters used in these equipments are given. Fabrication masks and images between the steps are shown.

Chapter 4 includes electrical measurements of diodes. Characterization steps of diode are shown and the characteristics of fabricated diodes are extracted. From extracted characteristics of didoes, efficiency estimations of rectennas are presented.

Chapter 5 concludes the thesis with discussion about the topics in the thesis.

Statement of problems encountered regarding to the topic and the future work in the topic area are presented.

## 2 Modeling and Simulations

Rectenna simulation is separated into two main parts. The first part is antenna simulations and the second part is MIM diode modeling and simulations. Modeled rectenna is aimed to be operated at  $5 \mu\text{m}$  ( $60 \text{ THz}$ ) wavelength.

### 2.1 Antenna Design and Simulations

Antenna designed and simulated in HFSS<sup>TM</sup> environment. There are two different antennas were designed and simulated. Antennas are excited by  $50\Omega$  terminals. Due to the reciprocity as mentioned before, radiation efficiency is taken as collection efficiency. The first antenna that is designed and simulated is high efficiency, narrow BW half-wave dipole antenna. The second antenna is lower efficiency wide BW bow-tie antenna. Later, two different modified versions of dipole antenna are designed first to increase BW in half-wave dipole antenna and second to increase efficiency in bow-tie antenna. All of the antennas are designed on to Si/SiO<sub>2</sub> substrate. Thickness of Si is  $500 \mu\text{m}$  and on top of Si, there is  $100 \text{ nm}$  SiO<sub>2</sub>.

#### 2.1.1 Half-Wave Dipole Antenna

In Fig 9, designed half-wave dipole antenna can be seen. Half-wave dipole antenna arms are  $70 \text{ nm}$  thick gold and antenna is fed between the antenna arms. The

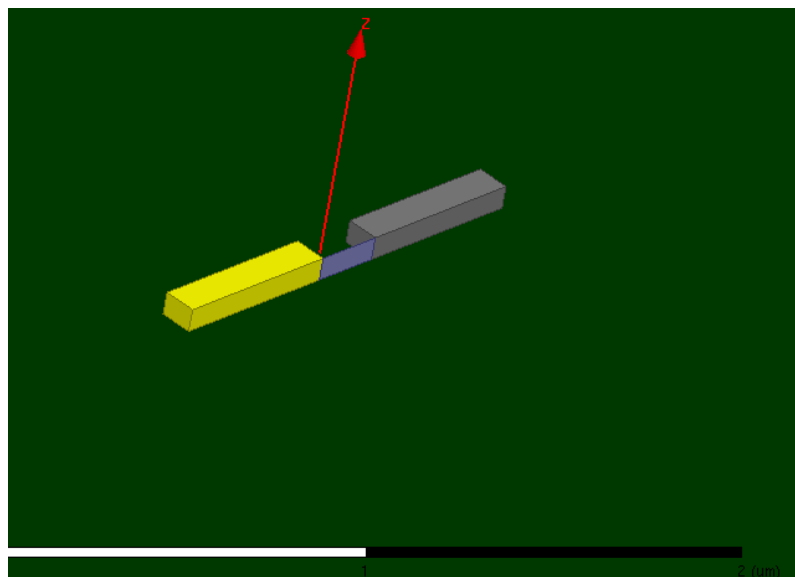
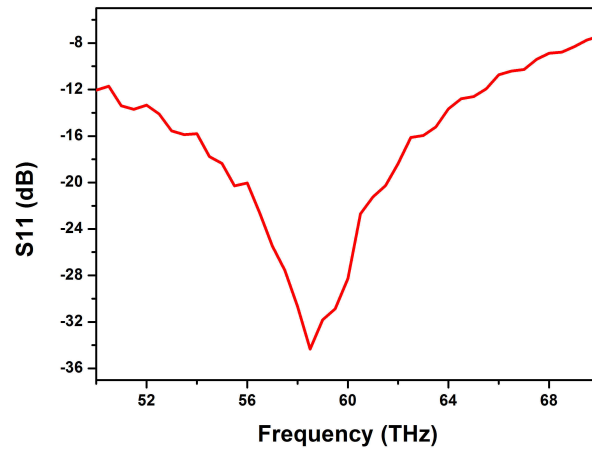
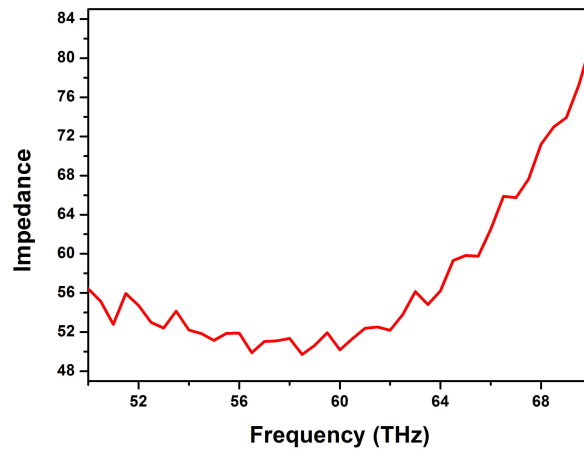


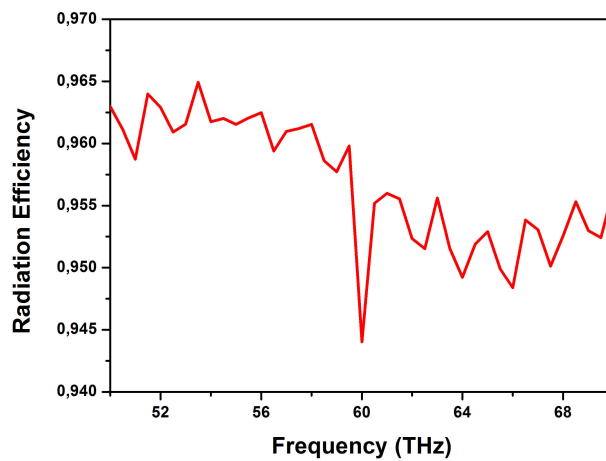
**Figure 9:** Designed half-wave dipole antenna in HFSS environment



(a)



(b)



(c)

**Figure 10:** Simulations result of half-wave dipole antenna in Fig. 9. (a) impedance matching, (b) antenna impedance (c) radiation efficiency

terminal have  $50 \Omega$  impedance.

Total length of the antenna is  $1.70 \mu\text{m}$  while the center wavelength is  $5 \mu\text{m}$ . The reason behind that is the half of the wavelength is  $2.5 \mu\text{m}$  and due to the refractive index of the  $\text{SiO}_2$ , the effective wavelength is reduces on the order of  $1.75 \mu\text{m}$ . The width of the antenna arms is around  $100 \text{ nm}$ .

In Fig. 10 simulation results of the half-wave antenna in Fig. 9 is shown. Fig. 10.a shows the impedance match of the antenna. The antenna is excited from  $50 \Omega$  terminal, therefore, it is matched according to  $50 \Omega$ . The matching occurs around  $58 \text{ THz}$ .  $10 \text{ dB BW}$  of the antenna is more than  $10 \text{ THz}$ . Impedance of the antenna is shown in Fig. 10.b. Half-wave antenna have nearly flat radiation efficiency between  $60 \text{ THz}$  and  $70 \text{ THz}$  around  $95\%$ .

### 2.1.2 Bow-tie Antenna

Bow-tie antenna design can be seen in the Fig. 11. Bow-tie antennas are broadband antennas where two triangles are pointing to each other like a bow-tie. In this design it is aimed to have wide BW while having impedance match at  $60 \text{ THz}$ . Bows have  $90^\circ$  base angle with  $2 \mu\text{m}$  base. Additional arms of  $4 \mu\text{m}$  are added to fix the center frequency. Antenna have  $70 \text{ nm}$  thickness and the arms have  $100 \text{ nm}$  of width.

Fig. 12 shows the simulation results of the bow-tie antenna. In Fig. 12.a it can be seen that center frequency of the antenna is around  $54 \text{ THz}$  and the  $10 \text{ dB BW}$  of the antenna is more than  $20 \text{ THz}$ . Impedance of the antenna is close to  $50 \Omega$ . However, different than half-wave dipole antenna, the radiation efficiency of

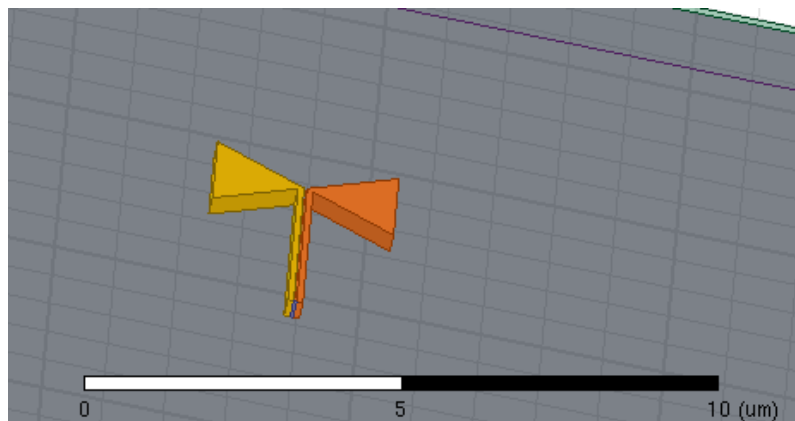
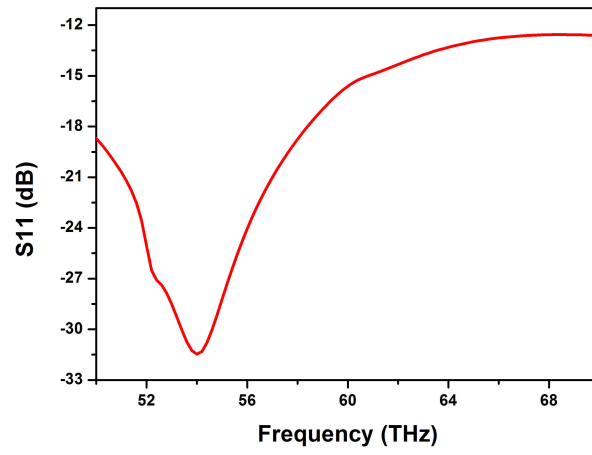
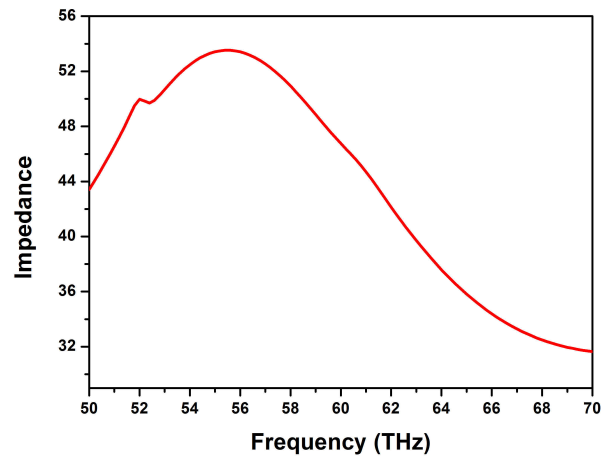


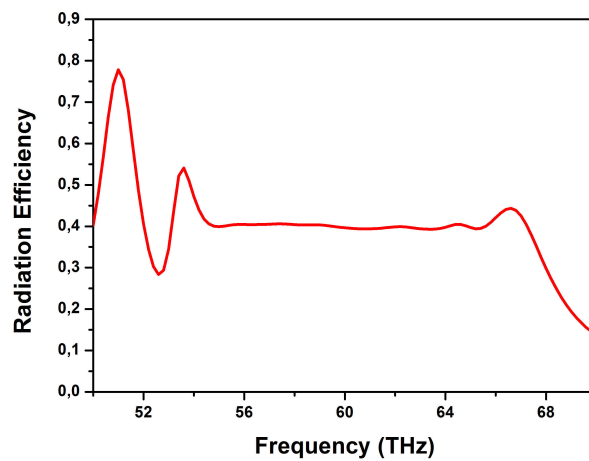
**Figure 11:** Designed bow-tie antenna in HFSS environment



(a)



(b)



(c)

**Figure 12:** Simulations result of bowie antenna in Fig. 11. (a) impedance matching, (b) antenna impedance (c) radiation efficiency

the bow-tie antenna is relatively low. Beside the efficiency spiking around 52 THz, antenna radiation efficiency is around 40% which is obvious in Fig. 12.c.

### 2.1.3 Modified Dipole Antenna

Half-wave dipole antenna is not enough BW for energy harvesting applications and bow-tie antenna is lacking of efficiency. Therefore, it is aimed to design another antenna giving out in antenna efficiency in half-wave dipole while gaining some BW.

In bow-tie antenna, additional arms into the antenna give practical impedance matching without destroying the wide BW property of the antenna. Hence additional arms can bring other frequencies into matching.

In Fig. 13, modified dipole antenna can be seen. In this antenna, there are two full-wave arms and there are two arms which connects to the measurement pads. Like other two designs, thickness of metals in this design is also 70 nm and the arm widths are 100 nm.

Simulation results of modified dipole antenna is shown in Fig. 14. It is aimed to have better matching over wide BW in this design, but impedance matching got worse. Even though impedance matching is above 10 dB, the change in the matching over wide band is low. That means that the impedance of the antenna is not changing dramatically in the 55 THz - 65 THz band. It is seen in Fig. 14.b that the antenna impedance is around  $112 \Omega$  with  $\pm 6 \Omega$  difference. Radiation efficiency dropped from 95% to 80% as expected

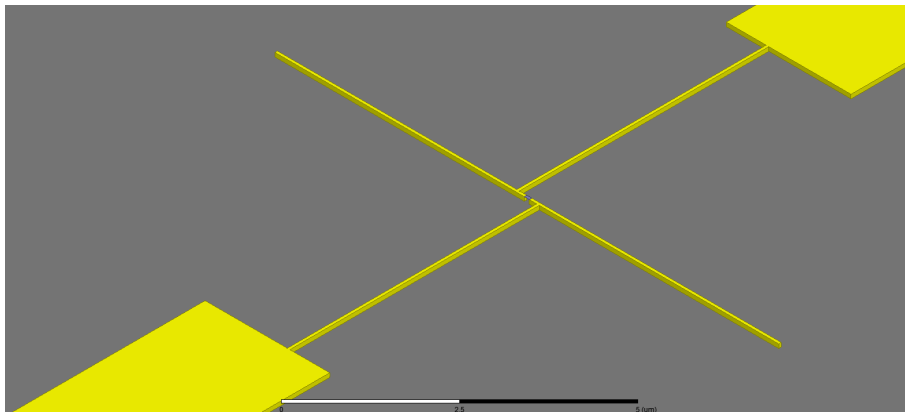
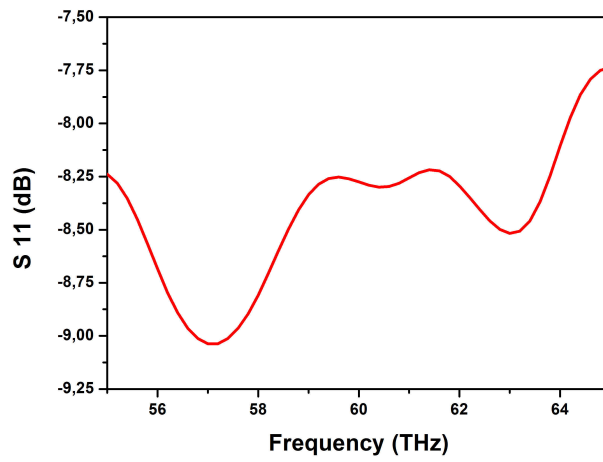
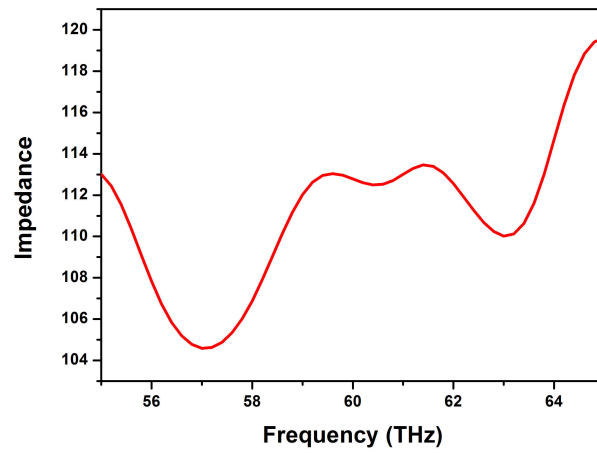


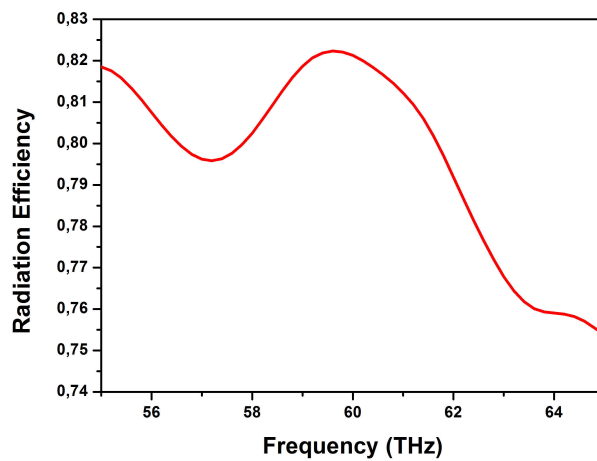
**Figure 13:** Designed first modified dipole antenna in HFSS environment



(a)



(b)



(c)

**Figure 14:** Simulations result of modified dipole antenna in Fig. 13. (a) impedance matching, (b) antenna impedance (c) radiation efficiency

## 2.2 Metal-Insulator-Metal Diode Modeling and Simulations

In order to simulate MIM diode characteristics, a simple model is built in MATLAB<sup>TM</sup> environment. In this model, it is aimed to simulate MIM diode characteristics and make parametric analysis to have optimized material selection and geometric properties.

In the model, the physical properties of the system has to be input. They are device parameters and device characteristics are calculated based on these parameters. Therefore the input of the simulation environment is only device parameters. The universal constants like Planck constant and Boltzmann constant are built-in to the model. The model calculations are consist of 4 main functions. The model algorithm can be seen in Fig. 15.

The simulation is starting from tunneling current extraction. The tunneling current is calculated according to the derivation. In this derivation required parts are calculated in separate functions on the other steps. Therefore, the second step is the tunneling probability calculations.

In the second step, tunneling probability of the electron through insulator barrier is calculated. These calculations are based on quantum electron tunneling phenomenon. The tunneling phenomenon inside the insulator layer is calculated starting form Schrödinger's equation to basically Transfer Matrix Method (TMM). While this function is calculating tunneling probability, information about barrier heights are needed. At that point simulation jumps to third step.

In the third step, barrier heights are calculated. Barriers are formed where the metal-insulator junctions exist. The energy difference between electron and the barrier height affects the tunneling probability. Additionally in this step, the image charges crated by the intense electric field at the metal-insulator junction [39]. The image charges at the junction lowers the barrier and increases the electron tunneling probability. The results form this step transferred to the tunneling probability calculation function.

Electron tunneling probability through insulator layer is calculated at the fourth step. Then in the fifth step, difference of Fermi functions of metals and tunneling probability is multiplied and current is calculated. After the current calculations, device characteristics are extracted applying by (10), (11), and (12).

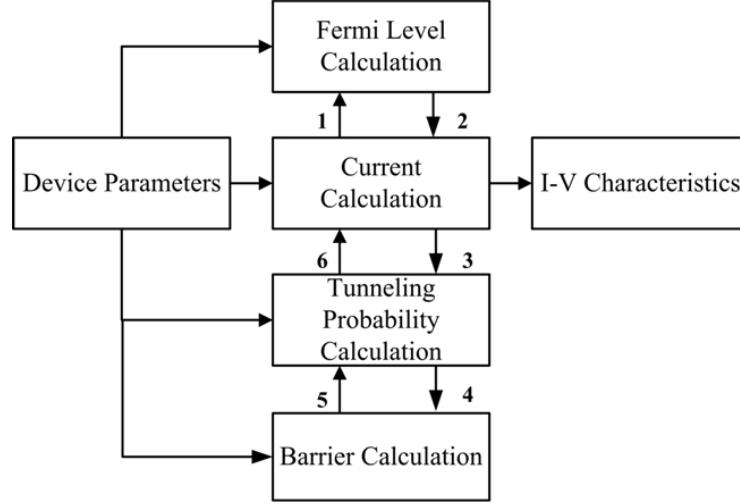


**Figure 15:** MATLAB algorithm diagram of MIM tunneling diode current calculation

### 2.2.1 Tunneling Current

In the first step of the MIM diode model, the tunneling current is calculated. The tunneling current includes tunneling probability of the electrons from the one side of the barrier. The total current is simply the number of electrons which have the probability of the tunneling in unit time. Therefore, the tunneling current can be stated as [29]:

$$J_x = -qnv = -qn_2(E)v(E)T(E_x) \quad (22)$$

where  $J_x$  is current density in direction of  $x$ ,  $q$  is charge,  $n$  is concentration of the carriers,  $E$  is electron energy,  $v$  is charge velocity and  $T(E_x)$  is tunneling probability in  $x$  direction. concentration of the carriers restated in terms of density of states  $g(E)$  and fermi distribution function  $f(E)$  as [43]:

$$n_2(E) = g_2(E)f_2(E) \quad (23)$$

where;

$$g(E) = \frac{4\pi(2m)^{\frac{1}{2}}}{h^3}\sqrt{E}dE \quad (24)$$

and [44];

$$f(E) = \frac{1}{\exp\left(\frac{E-E_F+qV_{bias}}{kT}\right) + 1} \quad (25)$$

where  $m$  denotes mass of an electron,  $h$  denotes Plank constant,  $k$  is Boltzmann constant and  $T$  is temperature.

The density of states can be expressed in terms of velocity starting from the equation of kinetic energy:

$$E = \frac{1}{2}mv^2 \therefore dE = mv dv \quad (26)$$

then substituting (26) into (24) gives:

$$g(v) = \frac{8\pi m^3}{h^3} v^2 dv \quad (27)$$

All of these equations considers charge carriers move all the directions in the space. If it is focused on tunneling though a insulator barrier as in Fig. 4, then these equations have to be reduced to 1-D forms. Assuming that tunneling only occurs on  $x$ -direction and velocity is in all  $x - y - z$  directions in Cartesian coordinate system, from the Spherical coordinate system, the other directions have to be integral out.

Integration is starting from Cartesian coordinate changing to Spherical coordinates:

$$dx = R \sin(\theta) d\phi; \quad dy = R d\theta; \quad dz = dR \quad (28)$$

Volume of a part of a sphere with radius  $R$  is:

$$dxdydz = 4\pi R^2 dr \therefore dv_x dv_y dv_z = 4\pi v_r^2 dv_r \quad (29)$$

therefore, the connection of velocity in the radial direction and Cartesian coordinates is found. If (29) is introduced to density of states equation (27), then the density of states can be stated in Cartesian coordinates as:

$$g(v) = 2 \frac{m^3}{h^3} dv_x dv_y dv_z \quad (30)$$

There is still  $y$  and  $z$  components of velocity in this equation. Using (28):

$$dv_y dv_z = v_r d\theta dv_r \quad (31)$$

in(31) differential,  $d\theta$  is taken integral form 0 to  $2\pi$ , resulting  $2\pi$ . Then from (26) and (31):

$$dv_y dv_z = \frac{2\pi}{m} dE \quad (32)$$

Then (30) and (31) are combined:

$$g(v) = 4 \frac{m^2 \pi}{h^3} dv_x dE \quad (33)$$

and continue with introducing (33) and (23):

$$n(v_x) = \frac{4\pi m^2}{h^3} \int f(E) dE dv_x \quad (34)$$

The density term in (22) can be replaced with (34):

$$J_{2 \rightarrow 1} = \int_{v_x} q v_x \frac{4\pi m_2^2}{h^3} \int_E f_2(E) dE T(E_x) dv_x \quad (35)$$

in which all the terms in  $x$  direction. But still the current density dependent to velocity and energy of electron. Due to the motion of electrons which is generally close to random, velocity term can be changed into energy by using (26), and if it is combined with (35), then:

$$J_{2 \rightarrow 1} = \frac{4\pi m_2 q}{h^3} \int_0^\infty T(E_x) \left[ \int_{E_x}^\infty f_2(E) dE \right] dE_x \quad (36)$$

is current density equation form metal-2 to metal-1. If similar procedure is applied to the reverse direction, current from metal-1 to metal-2 is simply:

$$J_{1 \rightarrow 2} = \frac{4\pi m_1 q}{h^3} \int_0^\infty T(E_x) \left[ \int_{E_x}^\infty f_1(E) dE \right] dE_x \quad (37)$$

The total current density can be found by simply subtracting the  $J_{1 \rightarrow 2}$  from  $J_{2 \rightarrow 1}$ , giving that:

$$J_{Tot} = \frac{4\pi m q}{h^3} \int_0^\infty T(E_x) \left[ \int_{E_x}^\infty f_2(E - V) - f_1(E) dE \right] dE_x \quad (38)$$

In this equation, it is assumed that effective mass of metal-1 and metal-2 equal to 1. From (38), it is clearly seen that the current strongly depend on the tunneling probability of the electron. The dominating currents is tunneling current. Only temperature dependence is inside the Fermi functions which has low effect on the general efficiency equation.

### 2.2.2 Transfer Matrix Method (TMM)

Transfer matrix method is a numerical method that used in calculation in complex systems [45]. In this method, generally system is divided into subsections in order to get more accurate results. In tunneling case, the barrier is divided to  $n$  subdivisions and for every part of the divisions, Schrödinger's equation is solved. The subsections in the insulator barrier is shown in Fig. 16. Later, all the equations are collected into nearly diagonal matrix and the output gives the equation of the electron that tunneled through the barrier.

In the first step, the wave equations of the electron have to be stated. From Schrödinger equation [44]:

$$\psi_{in} = \psi_0 = A_0^+ e^{ik_0 x} + A_0^- e^{-ik_0 x} \quad (39)$$

and;

$$\psi_{out} = \psi_{n+1} = A_{n+1}^+ e^{ik_{n+1} x} + A_{n+1}^- e^{-ik_{n+1} x} \quad (40)$$

where;

$$k_0 = \sqrt{(2m/\hbar^2) E} \quad (41)$$

and;

$$k_{n+1} = \sqrt{(2m/\hbar^2) (E + V)} \quad (42)$$

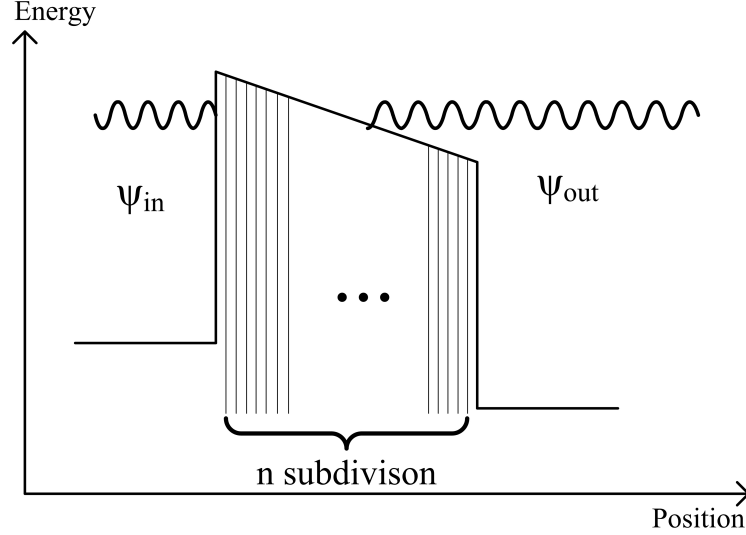


**Figure 16:** Potential barrier is divided to  $n$  subdivisions for TMM

$\psi_n$  is the wave at  $n^{th}$  division,  $A$  is the normalization factor,  $k_n$  is the wave vector at  $n^{th}$  division,  $x$  is the position,  $m$  is the particle mass,  $E$  is the energy of the particle at the junction, and  $V$  is the applied bias to one of the metals.

For every boundary, continuity of the waves have to be supported. Hence for each section;  $\psi_n = \psi_{n+1}$  and  $d\psi_n/dx = d\psi_{n+1}/dx$  have to be satisfied. Then the open form will be:

$$A_j^+ e^{\kappa_j x_j} + A_j^- e^{-\kappa_j x_j} = A_{j+1}^+ e^{\kappa_{j+1} x_j} + A_{j+1}^- e^{-\kappa_{j+1} x_j} \quad (43)$$

and;

$$A_j^+ \kappa_j e^{\kappa_j x_j} - A_j^- \kappa_j e^{-\kappa_j x_j} = A_{j+1}^+ \kappa_{j+1} e^{\kappa_{j+1} x_j} - A_{j+1}^- \kappa_{j+1} e^{-\kappa_{j+1} x_j} \quad (44)$$

where

$$\kappa_j = \sqrt{(2m/\hbar^2) (\varphi_j - E)} \quad (45)$$

$\varphi_j$  is the barrier height at  $j^{th}$  division.

The first assumption here is  $\psi_{in}$  has no component in  $-$  direction. This results  $A_0^+ = 1$ . The other assumption is simple after the first; there is no return component in  $\psi_{out}$ , which simply makes  $A_{n+1}^- = 0$ . If all other equations are brought together and collected into matrix form, the result will be following [46]:

$$\mathbf{M} \bullet \mathbf{A} = \mathbf{X} \quad (46)$$

where;

$$\mathbf{A} = (A_0^-, A_1^+, A_1^-, \dots, A_n^+ A_n^- A_{n+1}^+)^T \quad (47)$$

$$\mathbf{X} = (-1, -ik_0, 0, \dots, 0)^T \quad (48)$$

$$\mathbf{M} = \begin{pmatrix} \mathbf{M}_0^- & -\mathbf{M}_0^+ & 0 & 0 & 0 & \dots & 0 \\ 0 & \mathbf{M}_1^- & -\mathbf{M}_1^+ & 0 & 0 & \dots & 0 \\ 0 & 0 & \mathbf{M}_2^- & -\mathbf{M}_2^+ & 0 & \dots & 0 \\ 0 & 0 & 0 & \mathbf{M}_3^- & -\mathbf{M}_3^+ & \dots & 0 \\ \dots & \dots & \dots & \dots & \dots & \dots & \dots \\ 0 & 0 & 0 & 0 & 0 & \mathbf{M}_n^- & -\mathbf{M}_n^+ \end{pmatrix} \quad (49)$$

$$\mathbf{M}_j^- = \begin{pmatrix} e^{\kappa_j x_j} & e^{-\kappa_j x_j} \\ \kappa_j e^{\kappa_j x_j} & -\kappa_j e^{\kappa_j x_j} \end{pmatrix} \quad (50)$$

$$\mathbf{M}_j^+ = \begin{pmatrix} e^{\kappa_{j+1} x_j} & e^{-\kappa_{j+1} x_j} \\ \kappa_{j+1} e^{\kappa_{j+1} x_j} & -\kappa_{j+1} e^{\kappa_{j+1} x_j} \end{pmatrix} \quad (51)$$

$$\mathbf{M}_0^- = \begin{pmatrix} 1 \\ -ik_0 \end{pmatrix} \quad (52)$$

and;

$$\mathbf{M}_n^+ = \begin{pmatrix} e^{ik_{n+1} x_n} \\ ik_{n+1} e^{ik_{n+1} x_n} \end{pmatrix} \quad (53)$$

Then, the electron tunneling probability through insulator layer is simply the ratio of electron probability current at the output  $J_{out}$  to electron probability current at the input  $J_{in}$ :

$$T(E) = \frac{|J_{out}|}{|J_{in}|} = \frac{k_{n+1} |A_{n+1}^+|^2}{k_0 |A_0^+|^2} \quad (54)$$

where;

$$J = (\hbar/2mi) (\psi\partial_x\psi^* - \psi^*\partial_x\psi) \quad (55)$$

The tunneling probability is calculated according to the equations given above. At the end, (55) gives the tunneling probability of the electron tunneling through insulator barrier. Other than TMM, there is other ways to calculate tunneling probability like Wentzel–Kramers–Brillouin (WKB) approximation [44], however, TMM is giving more precise results due to it investigate the system in little pieces [45].

### 2.2.3 Effective Barrier Height

At the metal-insulator junction, complicated electronic structures exist due to the continuity disruption of electronic states. When there is applied voltage on one of the metals, then through the insulator layer, intense electric fields are formed. Therefore electrons are collected at the metal-insulator junction. These charges are called image charges and round the potential barrier and lowers it [39]. This lowering effect is increasing the tunneling current. The image potential which lowers the barrier is stated [31] below:

$$V_{image} = \frac{-1.15\lambda d^2}{x_j(d-x_j)} \quad (56)$$

where;

$$\lambda = \frac{e^2 \ln 2}{8\pi K \epsilon_0 d} \quad (57)$$

$d$  is thickness of the insulator layer,  $K$  is the dielectric constant of the insulator layer, and  $x_j$  is the distance of the position from the metal-insulator junction. Hence the effective barrier height becomes;

$$\varphi_{ef} = \varphi_j + V_{image,j} \quad (58)$$

$\varphi_{ef}$  denotes the effective barrier height where  $j^{th}$  distance to the junction.

From (56) and (57), it is clearly seen that, thickness and dielectric constant

of insulator are other parameters that affect the tunneling probability. Decrease in thickness and dielectric constant led the potential lower, which also lead the tunneling current increase due to the tunneling probability increase.

#### 2.2.4 MIM Diode Simulation Results

In order to understand the behavior of the MIM diodes and optimize them according to the applications, a basic simulation code is written in MATLAB<sup>TM</sup> environment as mentioned above.

Tunneling probability vs electron energy diagram of a MIM diode is shown in Fig. 17. In this MIM diode  $d = 2.5$  nm,  $\phi_l = 3$  eV,  $\phi_r = 5$  eV,  $E_F = 10$  eV,  $K = 10$ . Increase in the applied voltage increases the tunneling probability at same injected electron energy. Applied voltage increases one of the metals' in MIM structure Fermi level. Barrier of the insulator, which injected electrons to the system encounter, is lowering due to the applied voltage to the system. Therefore, possibility of an electron to tunnel through this energy barrier with respectively lower voltages increases. In Fig. 17 this behavior can be clearly seen. When the injected electron have 15 eV energy, if the applied voltage is -2 V, then the tunneling probability is very low around 3%, however if the applied voltage is around 2 V, then the electron

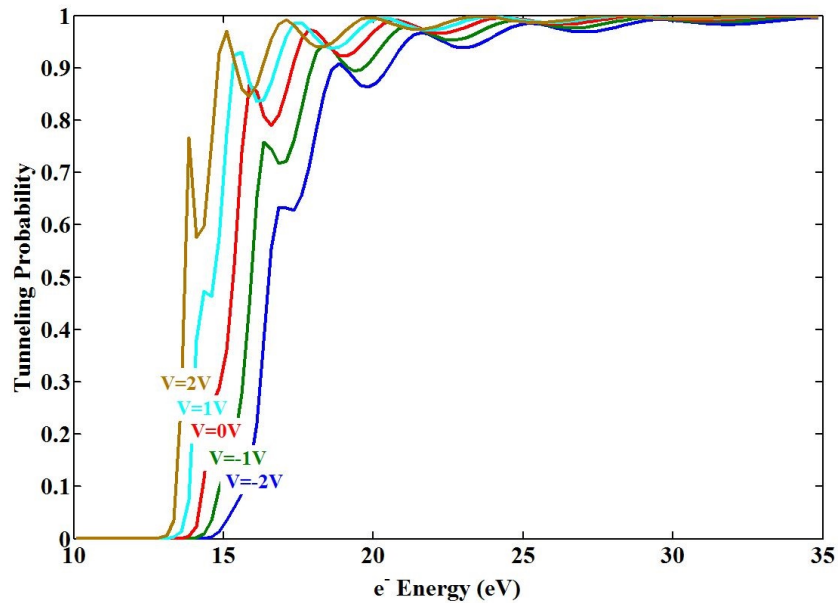


**Figure 17:** Tunneling probability of the MIM diode according to TMM method at different applied voltages. MIM have  $d = 2.5$  nm,  $K = 10$ ,  $\phi_l = 3$  eV,  $\phi_r = 5$  eV and  $E_{F,l} = 10$  eV

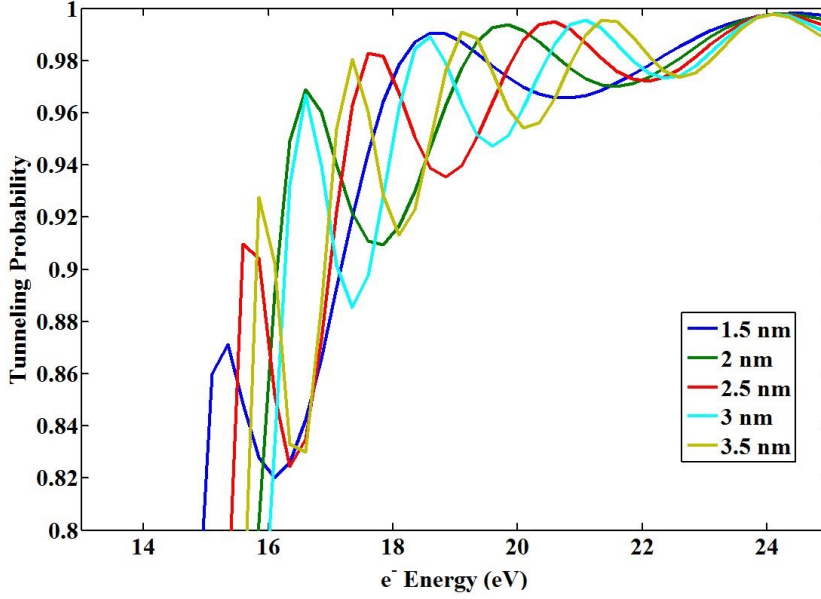


**Figure 18:** Tunneling probability of the MIM diode according to TMM method at different insulator thicknesses. MIM have  $V_{appl} = 0^+$  V,  $K = 10$ ,  $\phi_l = 3$  eV,  $\phi_r = 5$  eV and  $E_{F,l} = 10$  eV

tunneling probability increases around 70%.

Another factor effecting the tunneling probability is the thickness of the insulator barrier. It is expected that thinner barriers are easy to tunnel. In Fig. 18, simulation of tunneling probability of electron through insulators with different thickness is shown. Simulated MIM diode have same physical properties as in Fig. 17:  $\phi_l = 3$  eV,  $\phi_r = 5$  eV,  $E_F = 10$  eV,  $K = 10$  and  $V_{appl} = 0^+$  V. Increase in the insulator layer thickness decreases the tunneling probability. The tunneling probability of an electron decreases exponentially [44]. The exponential term in the wave equation in (39) shows exponential decrease. It is not clearly seen the behavior of tunneling probability under different thicknesses because of the oscillations, but it is clear around 22 eV electron energy in Fig. 18. In the high electron energies, tunneling probabilities are close to each other because electrons can jump over the potential barrier, but in the low electron energies, it is seen that there is nearly more than 10% of probability difference.

Beside the applied voltage and the thickness of the insulator layer, tunneling probability is also depend on the insulator dielectric constant. Dielectric constant states a material how good insulator and how cans store charges inside it. Therefore, good insulators tend to allow electron tunneling lower than other. It is expected that

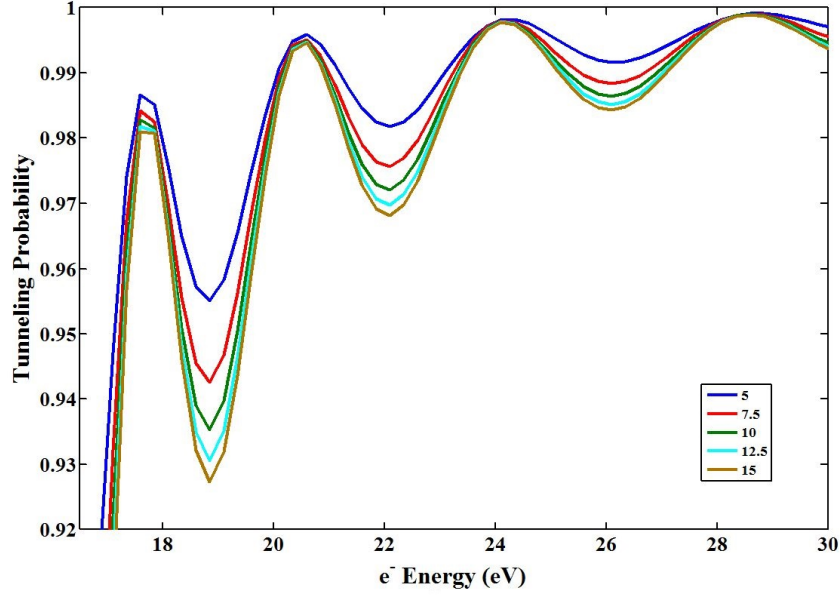


**Figure 19:** Tunneling probability of the MIM diode according to TMM method at different insulator dielectric constants. MIM have  $d = 2.5$  nm,  $V_{appl} = 0^+$  V,  $\phi_l = 3$  eV,  $\phi_r = 5$  eV and  $E_{F,l} = 10$  eV

as dielectric constant of the insulator increases, then tunneling probability decreases. In Fig. 19, it is shown the relation between dielectric constant of the insulator and electron tunneling probability. Simulated MIM diode have same physical properties as above:  $d = 2.5$  nm,  $\phi_l = 3$  eV,  $\phi_r = 5$  eV,  $E_F = 10$  eV, and  $V_{appl} = 0^+$  V. In the simulation results which can be seen in the Fig. 19, the oscillations peak at the same energy levels for different dielectric constants. The reason behind that is the thickness of the insulator is the same which only supports waves at some points. Other than that, because of the image potential and dielectric constant relation, the effective barriers are become lower in insulator with lower dielectric constant that leads higher tunneling probabilities. Around 19 eV electron energy, it is seen that there is 3% efficiency difference between the barrier having  $K=15$  and the barrier having  $K=5$ .

Barrier height behavior is also investigated in the simulations. In Fig. 20, the simulation results can be seen. In the simulations, it is aimed to observe the image force effect and the final effective barrier in (58) under different applied voltages. In this simulation, physical parameters of the MIM structure is similar to the ones above. MIM have  $d = 2.5$  nm,  $K = 10$ ,  $\phi_l = 3$  eV,  $\phi_r = 5$  eV and  $E_{F,l} = 10$  eV as physical properties. In Fig. 20 voltage sweep from -2 V to 2 V with 1 V steps is

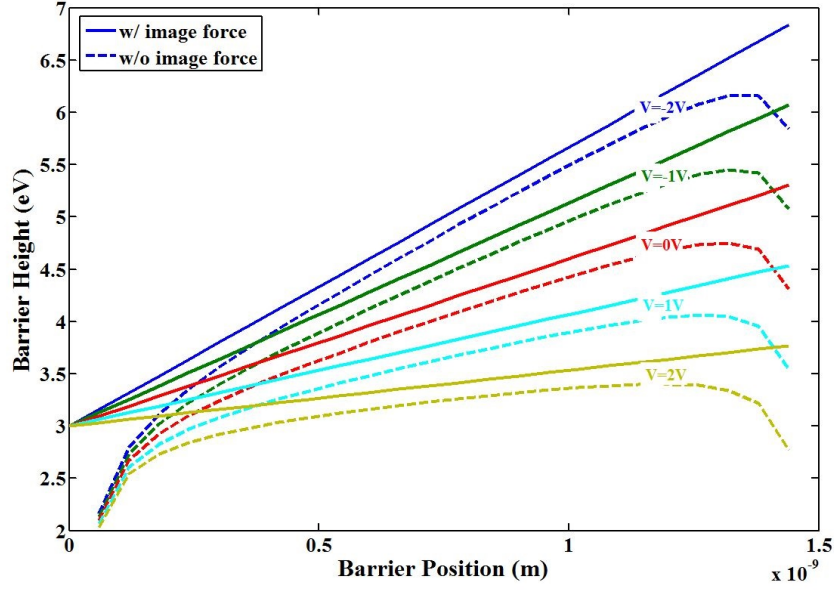


**Figure 20:** Barrier according to the Fermi level of the left metal, barrier heights and image forces is shown. MIM have  $d = 2.5$  nm,  $K = 10$ ,  $\phi_l = 3$  eV,  $\phi_r = 5$  eV and  $E_{F,l} = 10$  eV

shown. In the simulations, 0 eV energy level is set to Fermi level of left metal. As the applied voltage increases, the top of the potential barrier levels from trapezoidal shape to rectangular shape. The difference of potential barriers between left and right junctions is 2 eV. Therefore, at 2 V applied voltage, the top of the barrier levels. Additionally, the rounding of the edges and barrier lowering can be seen in the figure.

MIM diode simulations end with current-voltage characteristics. Other MIM characteristics of the MIM diode are extracted from I-V characteristics. In Fig. 21 MIM  $I - V$  characteristics is shown. The physical properties of the MIM diode simulated are listed as:  $K = 10$ ,  $\phi_l = 3$  eV,  $\phi_r = 5$  eV and  $E_{F,l} = 10$  eV. In the simulations, applied voltage is swiped from -1 V to 1 V. When a material set for insulator layer, the only parameters change for controlling diode characteristics is left is insulator layer thickness. In figure, it is clearly seen the effect of insulator layer thickness to tunneling current. Simulations are started from 1.5 nm insulator thickness to 3.5 nm insulator thickness in 0.5 nm steps. Results shows that there is linear relation between current density and insulator layer thickness. Between two steps there is more than 30 times current density difference.

The MIM simulations are required to find optimal MIM physical properties for

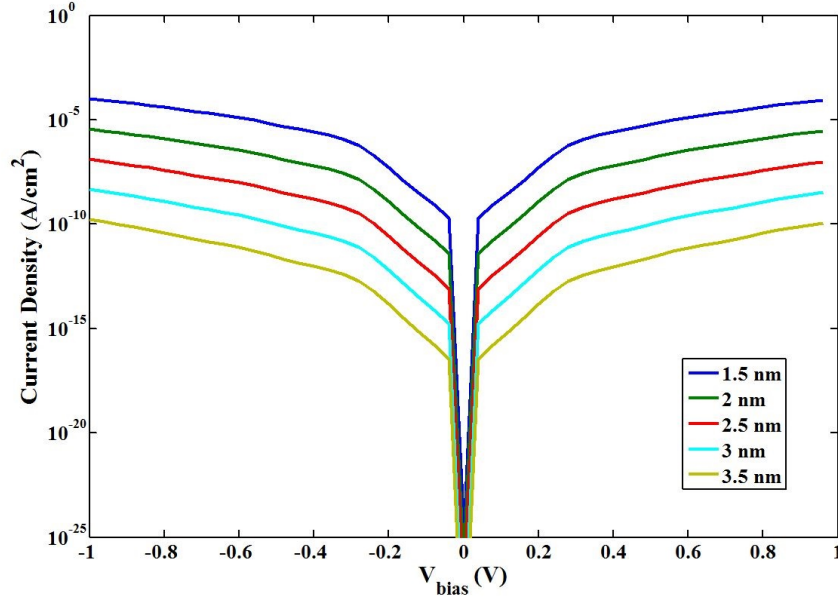


**Figure 21:** Current density and thickness of the barrier relation. MIM have  $V_{appl} = 0^+ \text{ V}$ ,  $K = 10$ ,  $\phi_l = 3 \text{ eV}$ ,  $\phi_r = 5 \text{ eV}$  and  $E_{F,l} = 10 \text{ eV}$

the application. Additionally behavioral analysis can be conducted. The simulations helps to figure out how MIM diodes work. It is important that after selecting the materials set, lots of the physical parameters that are input of the MIM diode simulation code will be set to materials' physical properties. The codes of the MIM diode simulator is open, so that simulations for similar structures like MIIM diodes can easily be conducted after configuring the code.

In the simulations real material sets are simulated.  $Au - AlOx - Al$ ,  $Au - AlOx - Cr$ ,  $Au - CrOx - Cr$ , and  $Au - TiOx - Ti$  are simulated. Insulator thickness in all the structures is 2.5 nm. The barrier formation of these structures is shown in Fig. 22. The barrier heights in  $Au - AlOx - Al$  MIM structure are 4.1 eV and 3.1 eV which is shown in Fig. 22.a. In this structure, asymmetry is low and the barriers are high to tunnel. In this type of structures, turn on voltage of the diode is expected to be at high voltages and tunneling current be low.  $Au - AlOx - Cr$  have barriers of 4.1 eV and 3.5 eV which is shown in Fig. 22.b. This structure is less asymmetric than the structure before. The barriers are higher than the first one, therefore, even lower tunneling currents are expected. 1.34 eV and 0.74 eV barrier formations are in  $Au - CrOx - Cr$  structure which can be seen in Fig. 22.c. This structure is asymmetric than the other two. It is expected from this structure that

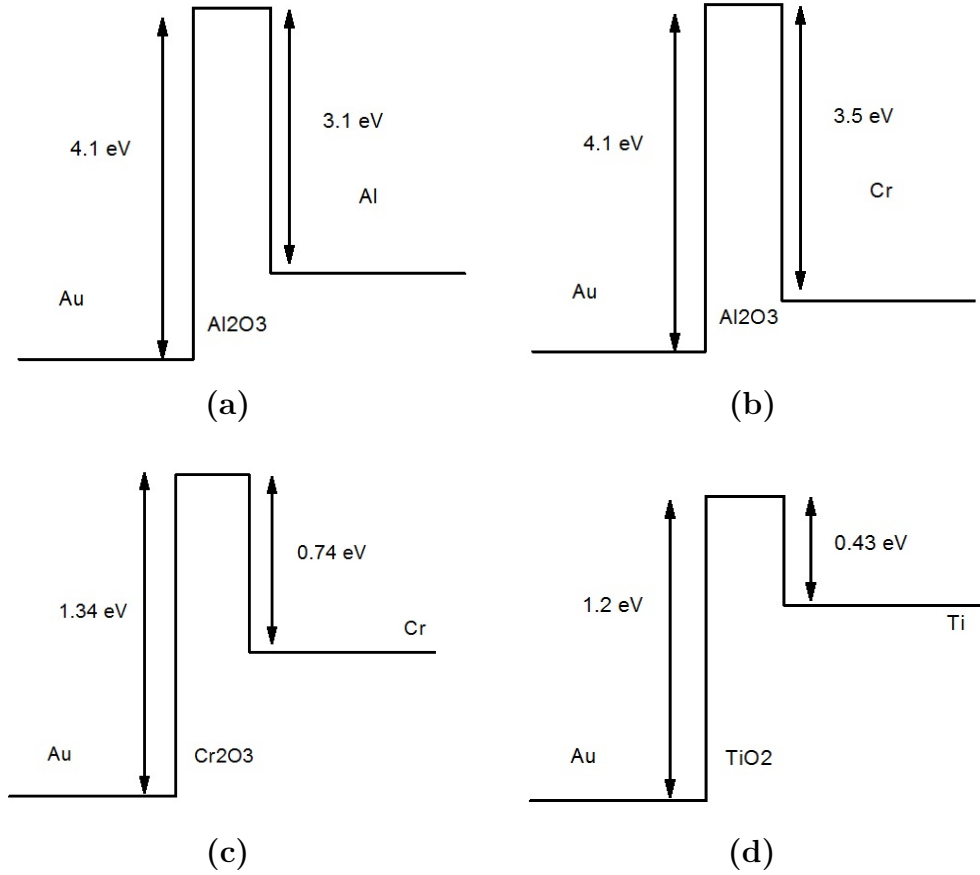


**Figure 22:** Barrier formation of MIM structures (a)  $Au - AlO_x - Al$  (b)  $Au - AlO_x - Cr$  (c)  $Au - CrO_x - Cr$  (d)  $Au - TiO_x - Ti$

tunneling current is higher than the other two and the asymmetry in the structure can be visible. In Fig. 22.d.  $Au - TiO_x - Ti$  structure can be seen with 1.2 eV and 0.43 eV. It is most asymmetric structure and it has lowest barrier heights. Hence, highest current is expected from this structure.

Fig. 23 shows the simulation result of the structures stated above. The voltage range in the simulation is set so be  $\pm 1$  V. In this range current densities of  $Au - AlO_x - Al$ ,  $Au - AlO_x - Cr$ ,  $Au - CrO_x - Cr$ , and  $Au - TiO_x - Ti$  MIM diodes are shown in the figure. The lowest current in the figure is from  $Au - AlO_x - Cr$  MIM diode. The barrier heights in this structure are the highest among others. As expectations, the current is the lowest in this structure. The current density of  $Au - AlO_x - Al$  MIM diode is very close to  $Au - AlO_x - Cr$  MIM diode. The barrier formation of two structures are very similar to each other, only on the one side of the barrier there is 0.4 eV difference.

Highest current is from  $Au - TiO_x - Ti$  MIM diode in Fig. 23. From the

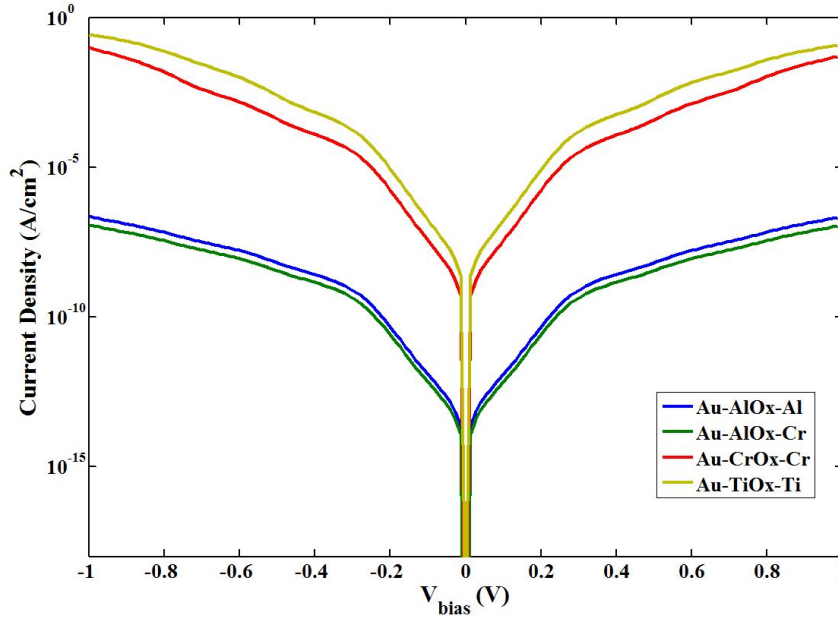


**Figure 23:** Current density of MIM structures  $Au - AlOx - Al$ ,  $Au - AlOx - Cr$ ,  $Au - CrOx - Cr$ , and  $Au - TiOx - Ti$

barrier formations shown in Fig. 22, it is expected that this structure yields in more current density because of its lowest barrier heights. It is clear that this structure has more current than the others.  $Au - CrOx - Cr$  barrier formation is close to  $Au - TiOx - Ti$  barriers and therefore the current densities are close to each other.

In these simulations it is seen that the model met the expectations about the current densities of the MIM structures. Although, the current density levels seem very low and the asymmetric is not clear on the current density plots. At least the current density differences and structural dependences are visible on the graph.

### 2.3 Rectenna Simulations and GUI

The simulations of antenna and MIM diode of rectenna is conducted in separate environments. It is aimed to design a graphical user interface (GUI) that both of the simulations can be conducted simultaneously and for the overall rectenna characteristics, to collect their results in same environment. Therefore, it is designed a GUI in MATLAB that two separate simulations can be conducted inside.

Fig. 24 shows rectenna simulator GUI. It is consist of 4 panels which are MIM-SIM inputs, HFSS inputs, MIM Materials and 3-D Model. Additionally there are 3 push buttons which start MIM simulation, antenna simulation and rectenna sim-

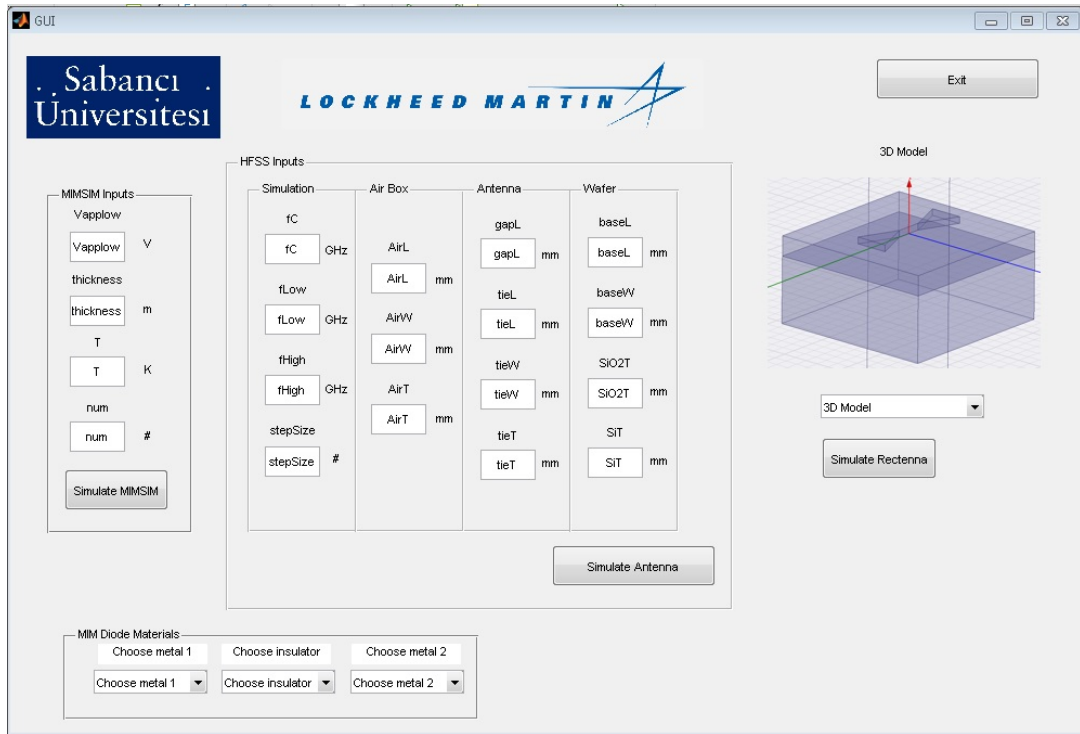


**Figure 24:** Rectenna GUI main screen - physical and simulation parameters input

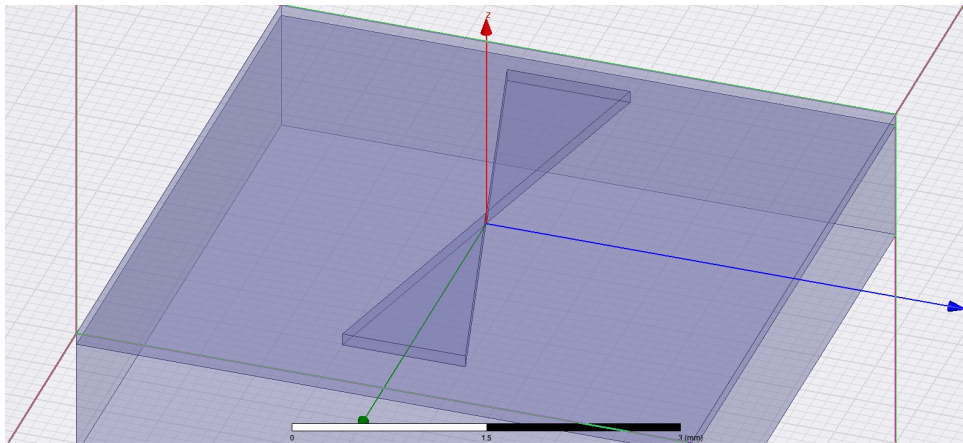


**Figure 25:** GUI screen-shot while antenna simulations

ulation. The results from the simulations are popping up as a separate MATLAB figures, and there is no need to be open up the simulation to see the results.

Before starting any of the simulations, it is required to fill the inputs in MIM diode materials panel. The materials in antenna and MIM simulations are directly assigned from this panel. In this panel, metal-1, insulator and metal-2 have to be selected. The physical properties of materials are directly send to the simulations.

HFSS Inputs panel consist of 15 inputs starting from center meshing frequency of antenna simulation, higher and upper limits of frequency, step size of frequency,

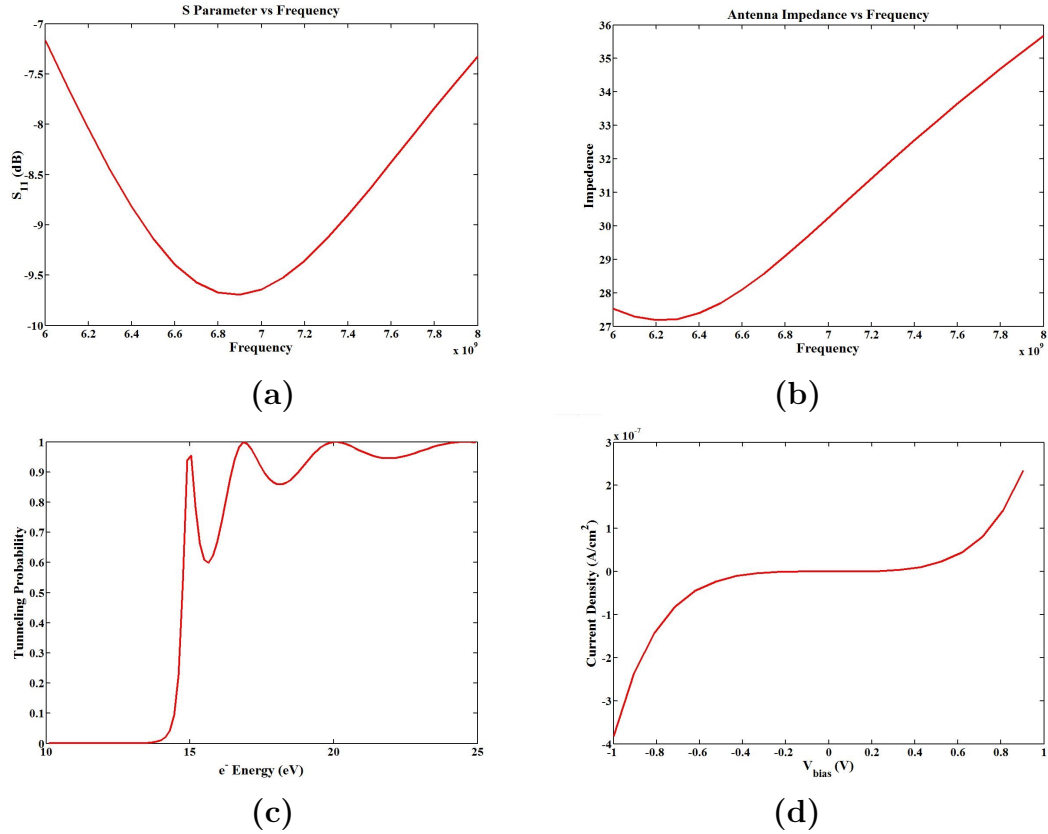


**Figure 26:** The output of GUI. (a)  $S_{11}$  vs. frequency (b) Antenna impedance vs. frequency (c) Tunneling probability vs electron energy (d) Diode  $I - V$  characteristic

simulation box  $x - y - z$  dimension sizes, bow-tie antenna geometrical parameters as tie length and width and substrate thickness. There are only bow-tie antenna and  $Si/SiO_2$  substrate exist in the first version of the simulations. Fig. 25 shows the HFSS simulation that is controlled form MATLAB GUI. Simulation of sinle antenna can be started from "Simulate Antenna" push button.

In MIMSIM input panel, there are 4 different inputs: minimum applied voltage, insulator thickness, temperature and insulator division number. After entering the inputs, the simulation can be started form "Simulate MIMSIM" push button.

Results from simulations using GUI is shown in Fig. 26. Antenna simulation results are shown in Fig. 26.a-b. In the first graph it is shown that the impedance matching of the antenna. The antenna is tried to matched to  $30 \Omega$ . The second graph is antenna impedance graph. As seen in the figure, antenna impedance is around  $30 \Omega$ . Fig. 26.c-d are tunneling probability and current density of MIM diode. MIM diode have  $K = 10$ ,  $\phi_l = 4.1$  eV,  $\phi_r = 3.1$  eV and  $E_{F,l} = 10$  eV ( $Al/AlOx/Au$ ). Around 15 eV, the first harmonic of the electron tunneling probability is reached.

## 3 Fabrication

### 3.1 Detailed Fabrication Procedure

After the modeling design and simulation of MIM diodes, these diodes are fabricated in Sabancı University SUNUM cleanroom facilities. Microelectronic fabrication tools in SUNUM facilities are capable of fabricating features of tens of nm size, which are the right choice for nano size MIM diode and antenna fabrication.

The fabrication of MIM diodes are completed in 3 steps. Metal-1, insulator and metal-2 are fabricated in different layers in separate steps. Each steps are consist of 5 substeps, which are shown in Fig. 27.a. The fabrication of MIM diodes starts with cutting into  $1.5 \text{ cm} \times 1.5 \text{ cm}$  pieces of  $100 \text{ nm SiO}_2$  coated  $Si$  substrate by mechanical diamond cutter equipment in cleanroom. After that, substrates are cleaned and prepared for resist coating. Resist is spin-coated on top of the substrates and after coating step, substrates and resist are baked for make them ready to lithography. Electron beam lithography (EBL) is employed for lithography step in order to achieve nm size feature resolutions. Later, resist on samples is developed and materials are deposited on the samples. Physical vapor deposition (PVD) system is

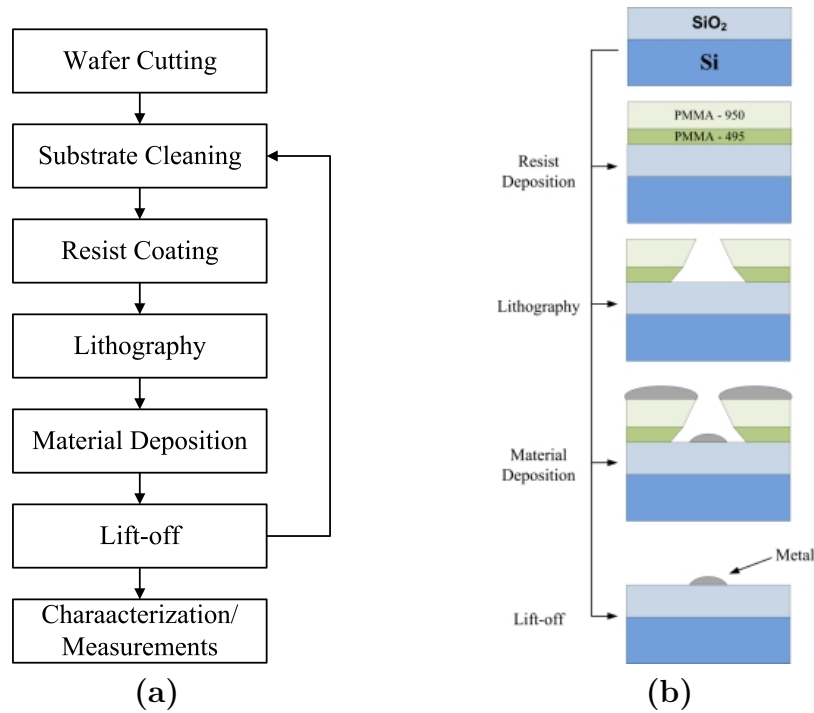


**Figure 27:** Flow-charts of fabrication procedure (a) flow of three layers fabrication step (b) cross section representation of substrate in a fabrication cycle

employed for deposition. The final features are given on to substrates after applying a lift-off process on the samples. If there is another layer on top of the fabricated layer, fabrication steps are applied from cleaning procedure again. If it is the last layer, then sample is prepared for characterizations or device measurements.

More detailed procedure is given below under specific fabrication steps.

### 3.1.1 Substrate Cleaning

Before starting the fabrication of any layer, the substrates have to be cleaned properly. Dust particles from wafer cutting or resist residuals from last step decrease the quality and the yield of the fabrication. Therefore a cleaning process is applied before each fabrication step. The cleaning is only applied to remove dusts and resist residuals on the surface. Hence, it can be only applied soft cleaning to the surface. Because, if there is other cleaning procedures applied on the surface, it can damage the  $Si/SiO_2$  substrate or even worse, the device layers.

Acetone (ACE) and Isopropyl alcohol (IPA) are used in the cleaning procedure. Firstly, the substrates are rinsed in ACE and kept in ACE filled petri dish. Then, it is floated on ultrasonic cleaner. The substrates are sonicated at 100% power and 40 °C for 10 minutes. After ten minutes, substrates are rinsed with ACE again and rinsed with IPA. After rinse, substrates are put into IPA filled petri dish and sonicated again at 100% power and 40 °C for 10 minutes. The substrates are rinsed with IPA again and dried with  $N_2$  purge.

After cleaning substrates with these steps, they are controlled under light microscope to see if there is any residue or dust left. If there is any residue or dust left on the surface of the substrate, then cleaning procedure is repeated until the surface of the substrate is clean and ready for the next fabrication cycle or step.

### 3.1.2 Electron Beam Lithography

The features of the antenna and the MIM diode are in nm sizes. Optical lithography does not capable of operating to give nm feature sizes. Therefore EBL system is used in MIM fabrications. The system which is used in fabrication is shown in Fig. 28.

Negative lithography is selected in lithography step. The reason behind this is



**Figure 28:** Electron beam lithography (EBL) system in Sabanci Univeristy SUNUM cleanroom facilities

nano features with etch-back mechanism is not suitable in MIM diodes. In order to apply negative lithography, two layer resist is coated. 495-k and 950-k polymethyl-metacrylate (PMMA) are used as EBL resist. Two layer resist enables have negative profile at the exposed areas which is essential for negative lithography. Negative profile can be seen in Fig. 27.b.

Before beginning of the lithography exposure, PMMA resists are laid. Resists are spin-coated on top of the substrate in yellow-room. The tools and the spinner used in spin coating can be seen in Fig. 29. On the first layer, 495-k PMMA and 950-k PMMA are used for first and second layer respectively. The reason of this is mass of 495-k PMMA is lower than 950-k which developed more than 950-k PMMA. This difference creates negative profile on the edges which is required for lift-off process.

The spin coating starts with 495-k PMMA laying on to substrate. Spinning takes 3 steps: The first step is 1000 rpm for 10 seconds with 100 rpm ramp, the second step is 6000 rpm for 50 seconds with 1000 rpm ramp and the last step is ending with 1000 rpm slowing down rate. The spin coating parameters can be seen in the Table 3. After spinning, the substrates are baked at 175 °C for 5 minutes. After bake, second layer is spin with same spinning parameters and baked at same temperature for 5 minutes. Resulting resist layer thickness is around 150 nm and it is enough for lift-off process of 70 nm thick layers.



**Figure 29:** Spin coating equipment and materials for laying resist in yellow-room

**Table 3:** Spin coating parameters

Spin Step	Ramp	Speed	Duration
	rpm	rpm	s
1	100	1000	10
2	1000	6000	50
3	-1000	0	6

After spin coating, the substrates are ready to expose electron beam. The tool in Fig. 28 is EBL system that is in use in SUNUM cleanroom facility. The samples are exposed under  $750 \mu\text{C}/\text{cm}^2$  electron dose with 12 nA filament current. The beam has 10 nm resolution and to give the shape exactly, beforehand of the exposure, proximity effect correction (PEC) is undertaken.

Samples are developed inside methyl-isobutyl-ketone (MIBK) solution. Development of the samples is done under a fume hood. First samples are dipped into 1:3 MIBK:IPA solution for 60 seconds. Then immediately, the samples are dipped into 1:1 MIBK:IPA solution for 5 seconds. After this step, to stop the development, samples are dipped into IPA for 60 seconds. Then the samples are rinsed with IPA, and dried with  $\text{N}_2$  purge. After this step, they are ready for material deposition.

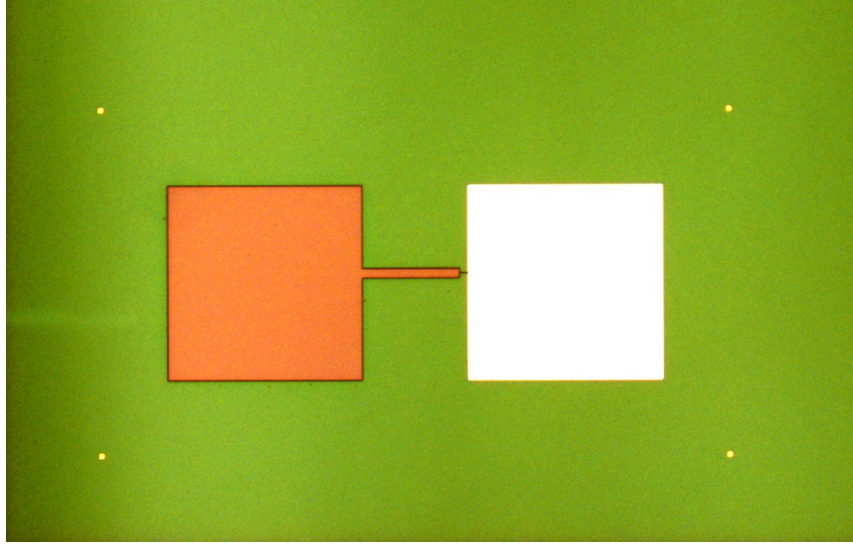


**Figure 30:** Sample after development under light microscopy. Patch on the right hand side is metal-1 of MIM diode, and the patch on the left hand side is developed area. Other parts are PMMA resist.

### 3.1.3 Material Deposition

The materials are deposited after the development in PVD system. There are 3 different layers in MIM structure and all of them are deposited in PVD. Metals are deposited with thermal evaporation system and insulators and some metals like  $Ti$  are evaporated with electron beam evaporation system. The PVD system in SUNUM cleanroom facilities can be seen in Fig. 31.

Thermal evaporation is used in depositing metals. In fabrication of MIM diodes  $Au$ ,  $Al$ ,  $Cr$ , and  $Ti$  is used as metals. Except  $Ti$ , all of the metals can be deposited by thermal evaporation method. Thermal evaporation method is a method that by heating the material, it is evaporated and the evaporated material sticks on the surface of samples due to the temperature difference.  $Ti$  cannot be evaporated in PVD system in Fig. 31.a because of high evaporation temperatures of  $Ti$  which cannot be supported by this system. In thermal evaporation system, metal pieces are put into Tungsten (W) boats and electrical current is flown through the boat. Due to the currents flowing, boat gets heated and it heats up the metals up to their evaporation temperature. By controlling the current, temperature is kept under control and therefore evaporation and deposition rates.

Electron beam evaporation is similar to the thermal evaporation. In e-beam evaporation, the material is not evaporated by the heat applied from a boat, but

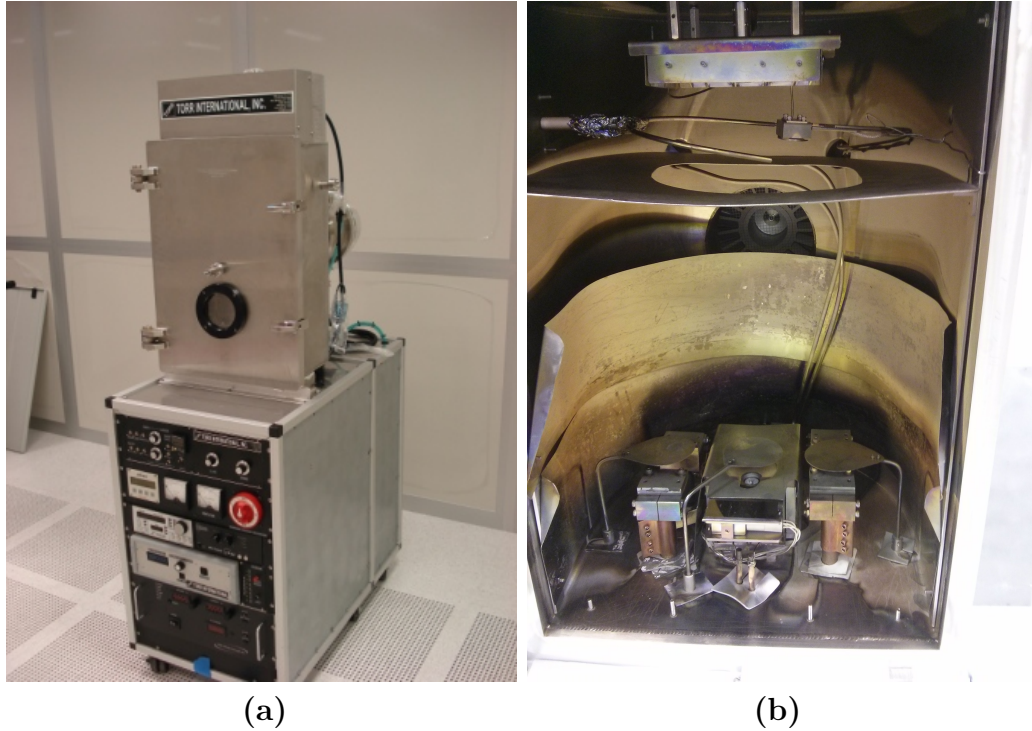


**Figure 31:** PVD system in cleanroom. (a) Photo of PVD system and electrical controls (b) deposition chamber and electron and heat sources of PVD system

it is evaporated by electron beams. This method can be applied both metals and insulator. The chemical ratio of ceramic can be kept after evaporation by e-beam evaporation because it is directly evaporating all the materials where e-beam hits. It is also used in metals with high melting points. *Au* and *Ti* which are used in MIM structures can be evaporated by this system. In this system, electrons which are emitted from a filament are deflected by a magnet and hit the material surface. Where the electrons hit evaporated and deposited on the sample. Density of electron flux emitted from filament can be controlled by changing the filament current. It is the way to control the evaporation rates.

The evaporation parameters of materials deposited can be seen in Table 4. According to the chamber pressure and the temperature, the evaporation parameters change in small orders every time. This trend can be seen in the 4.

Some of the diodes are sent for atomic layer deposition (ALD) for depositing  $Al_2O_3$ . The samples are deposited at 200 °C, in  $Al(CH)_3$  and  $H_2O$  precursors with  $N_2$  carrier gas. 2 nm, 5 nm and 8 nm depositions are completed in 20, 50, and 80 cycles of reaction where deposition rate is 1 Å/cycle.

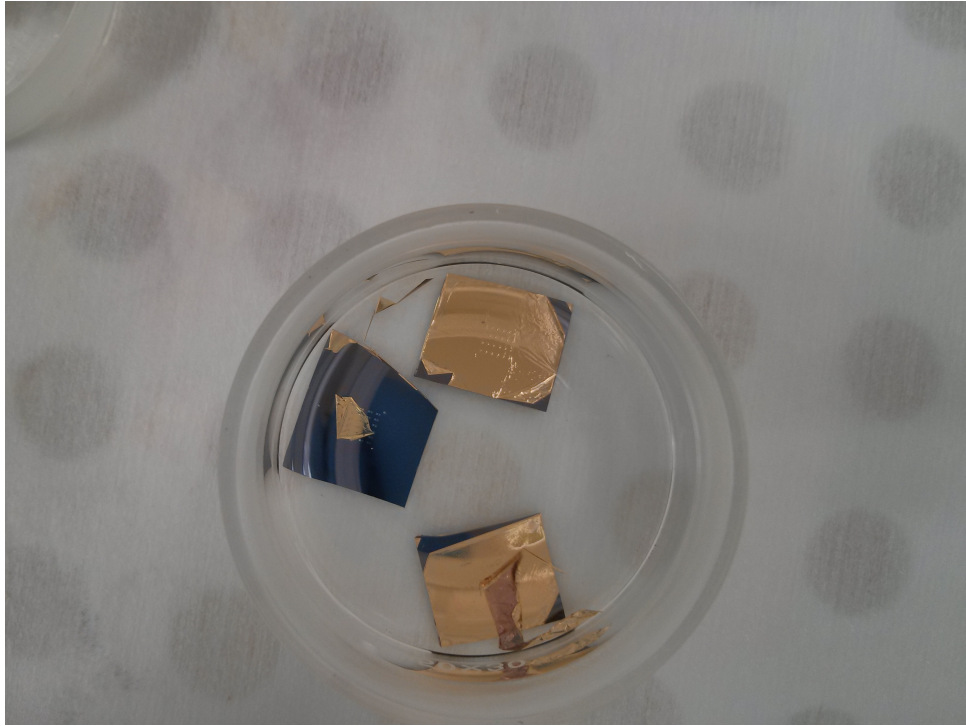


**Figure 32:** Samples while lift-off process

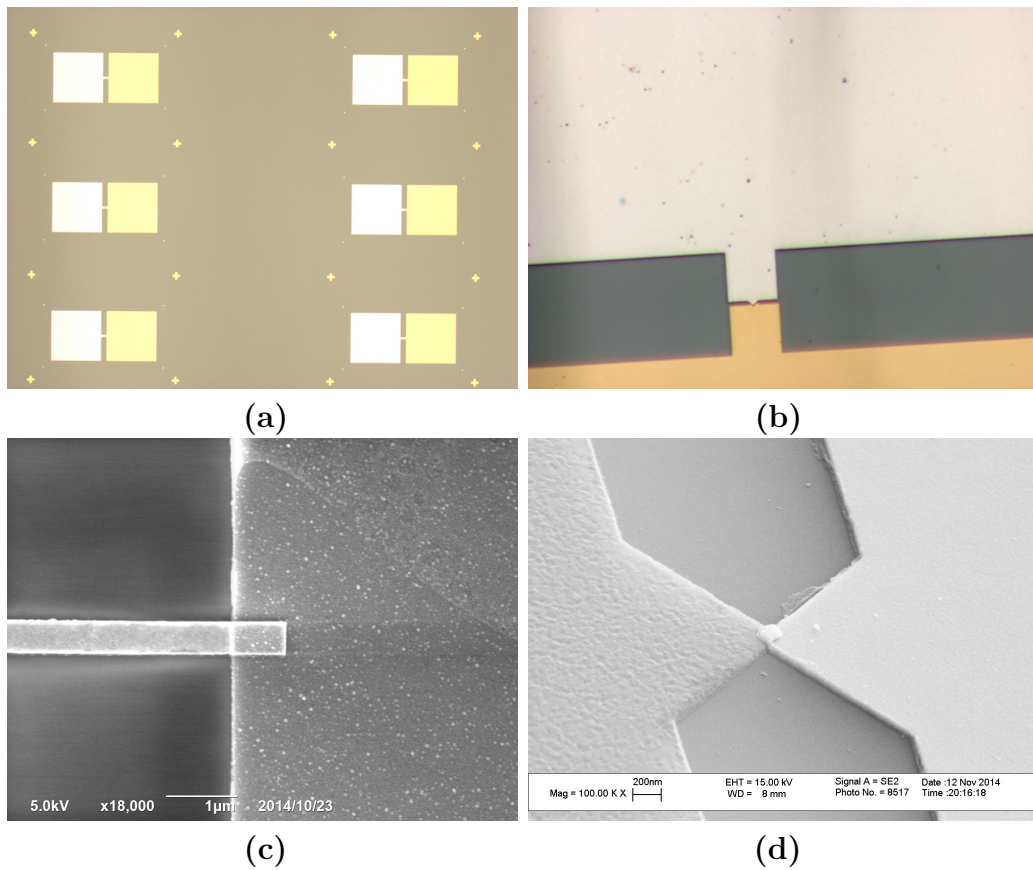


**Figure 33:** MIM diodes after fabrication (a) batch of MIM diodes and pads (b) MIM diode overlap; Scanning Electron Microscope (SEM) images of MIM diodes (a) single MIM diode (b) antenna coupled MIM diode

After deposition of materials, in order to give the final shape to the layer, lift-off process is applied on the samples. Due to the negative profile of the resist, deposited materials are discontinuous at the feature edges which can be seen in Fig. 27.b at fourth step. Solving the resist off the surface lifts the material which is on the resist. The material which can stick on the surface still sticks on the surface and the feature is written by this method on the substrate.

The final shape of the layer is given by lift-off process. The samples are washed with ACE and put into a petri dish which is filled with ACE. Then the petri dish is closed by a lid and it is heated up to 50 °C. In Fig. 32 the samples in the lift-off process can be seen. In the figure, it is clear that the metal sheet is lifting from the surface remaining only the metal which stuck on directly to surface in the developed areas.

Results from last lift-off process can be seen in Fig. 33. In this figure, it is shown the final state of the samples. Optical microscopy images of the samples are in Fig. 33.a.b. In this figure, the pads of the MIM diode can be seen. The size of the pads are  $200 \mu\text{m} \times 200 \mu\text{m}$  while the dimensions of the MIM diode is smaller than  $0.212 \mu\text{m} \times 0.212 \mu\text{m}$ . The sharpness of the shapes after lift-off process can be seen in Scanning Electron Microscopy images, shown in Fig. 33.c.d. Metal overlaps which can be seen in the middle of the figures are MIM diodes. They are basically consist of two metals overlapping and at the overlap, there is an insulator layer between them. Therefore MIM diodes are fabricated.

Fabricated MIM diode names and fabrication parameters is shown in Table 5. Some of the MIM diodes have same materials set and some of them have double insulator layers. In order to see the effects of materials and the geometrical parameters, they are built in different parameters.

## 3.2 Lithography Masks

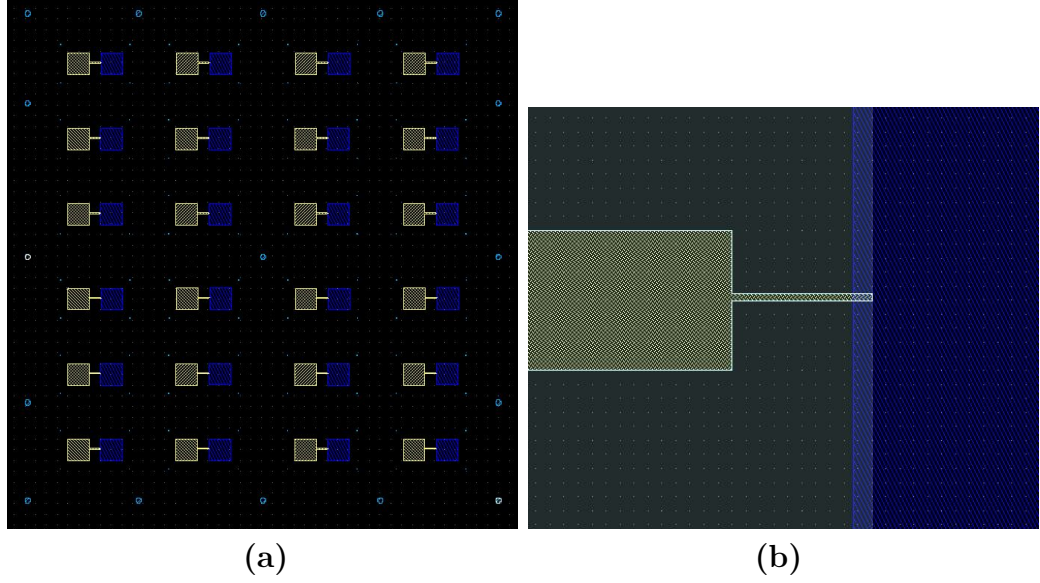
The features on the substrate is given by EBL. EBL is directly writing on the substrate without any shadow masks. It uses mask files and deflect its beam in  $x - y$  direction in order to write the correct features on the substrates. There are two major advantages of electronic masks. The first one is that they are on computers therefore nearly no cost of drawing them. The second one is changing

Table 4: Deposition parameters

Source	Type	Pressure	Current	Rate	Thickness	On
<i>Al</i>	Thermal	$7.70 \times 10^{-6}$ Torr	240 A	1.5 Å/s	90 nm	<i>Si/SiO<sub>2</sub>/Cr/Au/Al<sub>2</sub>O<sub>3</sub></i>
<i>Al</i>	Thermal	$5 \times 10^{-6}$ Torr	220 A	1.5 Å/s	90 nm	<i>Si/SiO<sub>2</sub>/Cr/Au/Al<sub>2</sub>O<sub>3</sub></i>
<i>Al</i>	Thermal	$6.08 \times 10^{-6}$ Torr	210 A	1.5 Å/s	65 nm	<i>Si/SiO<sub>2</sub>/</i>
<i>Au</i>	Thermal	$7.6 \times 10^{-6}$ Torr	210 A	2.3 Å/s	60 nm	<i>Si/SiO<sub>2</sub>/Cr</i>
<i>Au</i>	E-beam	$7.6 \times 10^{-6}$ Torr	55 mA	2.5 Å/s	65 nm	<i>Si/SiO<sub>2</sub>/Cr</i>
<i>Au</i>	E-beam	$8 \times 10^{-6}$ Torr	50 mA	2.5 Å/s	60 nm	<i>Si/SiO<sub>2</sub>/Cr</i>
<i>Cr</i>	Thermal	$5 \times 10^{-6}$ Torr	70 A	2 Å/s	5 nm	<i>Si/SiO<sub>2</sub></i>
<i>Cr</i>	Thermal	$5.3 \times 10^{-6}$ Torr	66 A	1.7 Å/s	65 nm	<i>Si/SiO<sub>2</sub></i>
<i>Cr</i>	Thermal	$8.14 \times 10^{-6}$ Torr	66 A	1.7 Å/s	65 nm	<i>Si/SiO<sub>2</sub>/Cr/Au/Cr<sub>2</sub>O<sub>3</sub></i>
<i>Cr</i>	Thermal	$8.14 \times 10^{-6}$ Torr	66 A	1.7 Å/s	65 nm	<i>Si/SiO<sub>2</sub>/Cr/Au/Al<sub>2</sub>O<sub>3</sub></i>
<i>Cr</i>	Thermal	$8.5 \times 10^{-6}$ Torr	60 A	1.5 Å/s	65 nm	<i>Si/SiO<sub>2</sub>/Cr/Au</i>
<i>Cr</i>	Thermal	$8 \times 10^{-6}$ Torr	60 A	2 Å/s	77 nm	<i>Si/SiO<sub>2</sub></i>
<i>Cr</i>	E-beam	$8 \times 10^{-6}$ Torr	30 mA	0.8 Å/s	5 nm	<i>Si/SiO<sub>2</sub></i>
<i>Cr</i>	E-beam	$5.8 \times 10^{-6}$ Torr	23 mA	0.3 Å/s	5 nm	<i>Si/SiO<sub>2</sub></i>
<i>Ti</i>	E-beam	$6.35 \times 10^{-6}$ Torr	75 mA	1.2 Å/s	70 nm	<i>Si/SiO<sub>2</sub></i>
<i>Ti</i>	E-beam	$9.8 \times 10^{-6}$ Torr	65 mA	1.7 Å/s	90 nm	<i>Si/SiO<sub>2</sub>/Cr/Cr<sub>2</sub>O<sub>3</sub>/TiO<sub>2</sub></i>
<i>Al<sub>2</sub>O<sub>3</sub></i>	E-beam	$8 \times 10^{-6}$ Torr	22 mA	0.4 Å/s	2.5 nm	<i>Si/SiO<sub>2</sub>/Cr/Au</i>
<i>Al<sub>2</sub>O<sub>3</sub></i>	E-beam	$8 \times 10^{-6}$ Torr	19 mA	0.3 Å/s	5 nm	<i>Si/SiO<sub>2</sub>/Cr/Au</i>
<i>Al<sub>2</sub>O<sub>3</sub></i>	E-beam	$8.7 \times 10^{-6}$ Torr	25 mA	0.2 Å/s	2.5 nm	<i>Si/SiO<sub>2</sub>/Cr/Cr<sub>2</sub>O<sub>3</sub></i>
<i>Al<sub>2</sub>O<sub>3</sub></i>	E-beam	$7 \times 10^{-6}$ Torr	26 mA	0.1 Å/s	1 nm	<i>Si/SiO<sub>2</sub>/Al</i>
<i>Cr<sub>2</sub>O<sub>3</sub></i>	E-beam	$8 \times 10^{-6}$ Torr	21 mA	0.2 Å/s	5 nm	<i>Si/SiO<sub>2</sub>/Cr/Au</i>
<i>Cr<sub>2</sub>O<sub>3</sub></i>	E-beam	$9 \times 10^{-6}$ Torr	24 mA	0.2 Å/s	2.5 nm	<i>Si/SiO<sub>2</sub>/Cr</i>
<i>TiO<sub>2</sub></i>	E-beam	$8 \times 10^{-6}$ Torr	20 mA	0.2 Å/s	5 nm	<i>Si/SiO<sub>2</sub>/Cr/Au</i>
<i>TiO<sub>2</sub></i>	E-beam	$9 \times 10^{-6}$ Torr	27 mA	0.3 Å/s	2.5 nm	<i>Si/SiO<sub>2</sub>/Cr/Cr<sub>2</sub>O<sub>3</sub></i>
<i>TiO<sub>2</sub></i>	E-beam	$8 \times 10^{-6}$ Torr	24 mA	0.2 Å/s	2.5 nm	<i>Si/SiO<sub>2</sub>/Cr/Au</i>

Table 5: Fabricated MIM diodes

Sample Name	Composition	Thicknesses	Mask No.	Area
MM1	Al/Al <sub>2</sub> O <sub>3</sub> /Cr/Au	65-2-5-65	1	1.3 $\mu\text{m}^2$ — 0.65 $\mu\text{m}^2$ — 0.13 $\mu\text{m}^2$
MM2	Al/Al <sub>2</sub> O <sub>3</sub> /Cr/Au	65-5-5-65	1	1.3 $\mu\text{m}^2$ — 0.65 $\mu\text{m}^2$ — 0.13 $\mu\text{m}^2$
MM3	Al/Al <sub>2</sub> O <sub>3</sub> /Cr/Au	65-8-5-65	1	1.3 $\mu\text{m}^2$ — 0.65 $\mu\text{m}^2$ — 0.13 $\mu\text{m}^2$
MM4	Al/Al <sub>2</sub> O <sub>3</sub> /Cr/Au	90-5-5-60	2	0.005 $\mu\text{m}^2$ — 0.02 $\mu\text{m}^2$ — 0.45 $\mu\text{m}^2$
MM5	Au/Al <sub>2</sub> O <sub>3</sub> /Al	60-5-90	2	0.005 $\mu\text{m}^2$ — 0.02 $\mu\text{m}^2$ — 0.45 $\mu\text{m}^2$
Alu-1	Au/Al <sub>2</sub> O <sub>3</sub> /Al	70-2-90	2	0.005 $\mu\text{m}^2$ — 0.02 $\mu\text{m}^2$ — 0.45 $\mu\text{m}^2$
Alu-2	Au/Al <sub>2</sub> O <sub>3</sub> /Al	70-5-90	2	0.005 $\mu\text{m}^2$ — 0.02 $\mu\text{m}^2$ — 0.45 $\mu\text{m}^2$
Alu-3	Au/Al <sub>2</sub> O <sub>3</sub> /Al	70-8-90	2	0.005 $\mu\text{m}^2$ — 0.02 $\mu\text{m}^2$ — 0.45 $\mu\text{m}^2$
N-1	Au/Al <sub>2</sub> O <sub>3</sub> /Al	70-2-90	2	0.005 $\mu\text{m}^2$ — 0.02 $\mu\text{m}^2$ — 0.45 $\mu\text{m}^2$
N-2	Au/Al <sub>2</sub> O <sub>3</sub> /Al	70-5-90	2	0.005 $\mu\text{m}^2$ — 0.02 $\mu\text{m}^2$ — 0.45 $\mu\text{m}^2$
N-3	Au/Al <sub>2</sub> O <sub>3</sub> /Al	70-8-90	2	0.005 $\mu\text{m}^2$ — 0.02 $\mu\text{m}^2$ — 0.45 $\mu\text{m}^2$
Ox-1	Au/Al <sub>2</sub> O <sub>3</sub> /Al	70-2-90	2	0.005 $\mu\text{m}^2$ — 0.02 $\mu\text{m}^2$ — 0.45 $\mu\text{m}^2$
Ox-2	Au/Al <sub>2</sub> O <sub>3</sub> /Al	70-5-90	2	0.005 $\mu\text{m}^2$ — 0.02 $\mu\text{m}^2$ — 0.45 $\mu\text{m}^2$
Ox-3	Au/Al <sub>2</sub> O <sub>3</sub> /Al	70-8-90	2	0.005 $\mu\text{m}^2$ — 0.02 $\mu\text{m}^2$ — 0.45 $\mu\text{m}^2$
LM1	Au/Cr <sub>2</sub> O <sub>3</sub> /Cr	60-5-65	2	0.005 $\mu\text{m}^2$ — 0.02 $\mu\text{m}^2$ — 0.45 $\mu\text{m}^2$
LM2	Au/TiO <sub>2</sub> /Ti	60-5-65	2	0.005 $\mu\text{m}^2$ — 0.02 $\mu\text{m}^2$ — 0.45 $\mu\text{m}^2$
LM3	Au/Al <sub>2</sub> O <sub>3</sub> /TiO <sub>2</sub> /Ti	60-2-5-2-5-65	2	0.005 $\mu\text{m}^2$ — 0.02 $\mu\text{m}^2$ — 0.45 $\mu\text{m}^2$
LM4	Au/Al <sub>2</sub> O <sub>3</sub> /Cr	60-5-65	2	0.005 $\mu\text{m}^2$ — 0.02 $\mu\text{m}^2$ — 0.45 $\mu\text{m}^2$
LMC	Cr/Cr <sub>2</sub> O <sub>3</sub> /TiO <sub>2</sub> /Ti	77-2-5-2-5-70	3	0.212 $\mu\text{m}^2$



**Figure 34:** Mask 1: (a) pads and markers are visible (b) connection line overlaps  $0.2121 \mu\text{m} \times 0.2121 \mu\text{m}$  with the metal on the right side.

them is done on computer, so it is simple to change them.

In fabrication of MIM diodes, three different masks are used. The first mask used is shown in Fig. 34. This mask consist of 24 MIM diodes with three different sizes. The areas of MIM diodes are  $1.3 \mu\text{m} \times 1 \mu\text{m}$ ,  $1.3 \mu\text{m} \times 0.5 \mu\text{m}$ , and  $1.3 \mu\text{m} \times 0.1 \mu\text{m}$  therefore diodes areas are  $1.3 \mu\text{m}^2$ ,  $0.65 \mu\text{m}^2$ , and  $0.13 \mu\text{m}^2$ .

In the second mask used in the fabrications, MIM diodes are coupled with bow-tie antennas. This mask is shown in Fig. 35. On this mask there are 60 antenna-coupled MIM diodes exist. Similar to 1st mask, there are three different diode sizes on the mask which are,  $0.0707 \mu\text{m} \times 0.0707 \mu\text{m}$ ,  $0.1414 \mu\text{m} \times 0.1414 \mu\text{m}$ , and  $0.2121 \mu\text{m} \times 0.2121 \mu\text{m}$ . The diodes areas are  $0.005 \mu\text{m}^2$ ,  $0.02 \mu\text{m}^2$ , and  $0.45 \mu\text{m}^2$ .

like the second mask, third mask is also having antenna-coupled MIM diodes. In this mask there are 50 dipole antenna-coupled MIM diodes and diodes are on  $0.46 \mu\text{m} \times 0.46 \mu\text{m}$  overlap area. This mask is shown in Fig. 36. The pads and the markers are visible in Fig. 36.a. In Fig. 36.b. diode and the antenna are visible.

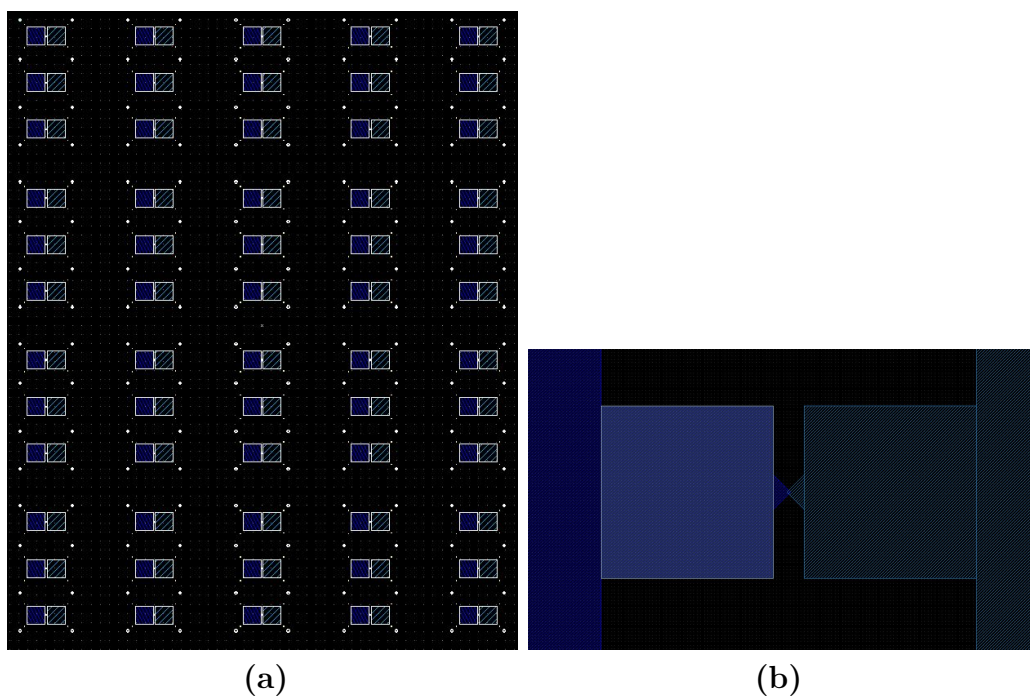


**Figure 35:** Mask 2: (a) pads and markers are visible (b) connection line overlaps  $0.46 \mu\text{m} \times 0.46 \mu\text{m}$  with the metal connection on the right side.

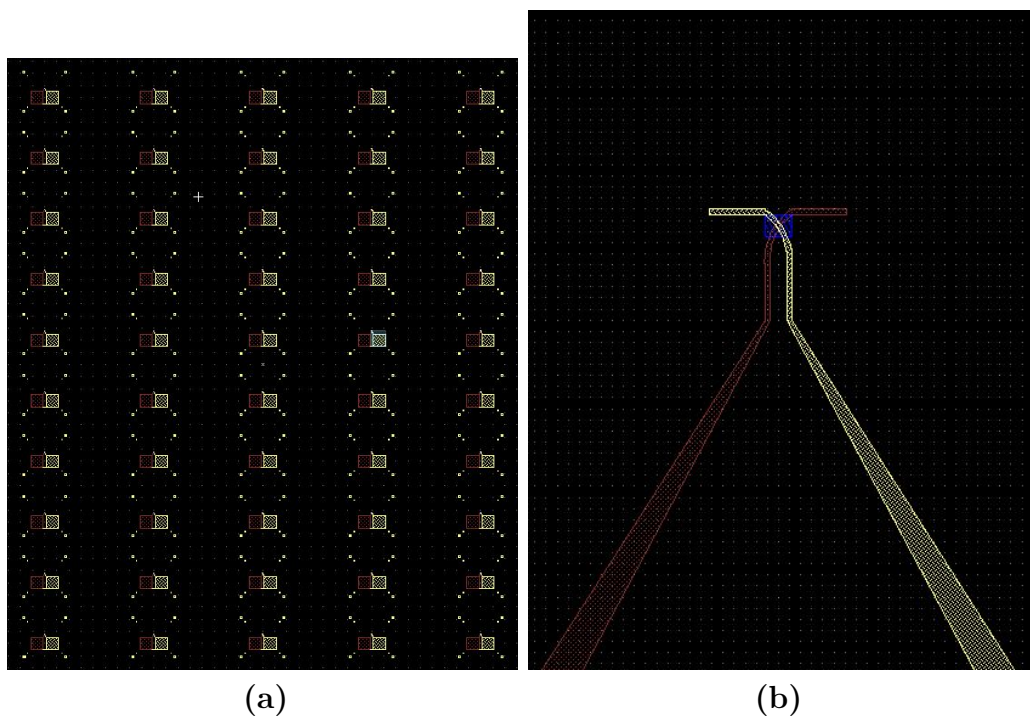


**Figure 36:** Mask 3: (a) pads and markers are visible (b) connection line overlaps  $1.3 \mu\text{m} \times 0.5 \mu\text{m}$  with the metal connection on the right side.

## 4 Measurements and Characterization

### 4.1 Measurement Setup

Fabricated MIM diodes are measured by Agilent B1500A Semiconductor Parameter Analyzer inside of an EM shielded black box environment. The measurement setup can be seen in Fig. 37. The setup is built the DC  $I - V$  characteristics of MIM diodes. Additionally, there is 1.5  $\mu\text{m}$  laser to observe the behavior of MIM diodes under EM radiation. The laser source can be seen on the left hand side in the Fig. 37.a. A fiber is used to direct the light from the source to EM shielded probe station. The fiber which is coupled to the source is used to shine light on the MIM diodes which can be seen on the left hand side in Fig. 37.b. There is no 5  $\mu\text{m}$  light source to do optical measurements of the rectenna a design frequency.

Fabricated MIM diodes are measured with tungsten DC needle probes. Needle probes are controlled by micro-manipulator system in order to make contact on the pads of the MIM diodes. The positions of the needle probes are watched over a optical microscope which is positioned right on top of the substrates. Needle probes are connected to a device under test (DUT) unit by coaxial cables and then to semiconductor parameter analyzer.

Once the probes and pads are contacted, the door of the probe station is closed and the measurements start. Several different measurements are taken form a MIM diode. Results are collected from semiconductor analyzer and MIM diode characteristics are extracted.

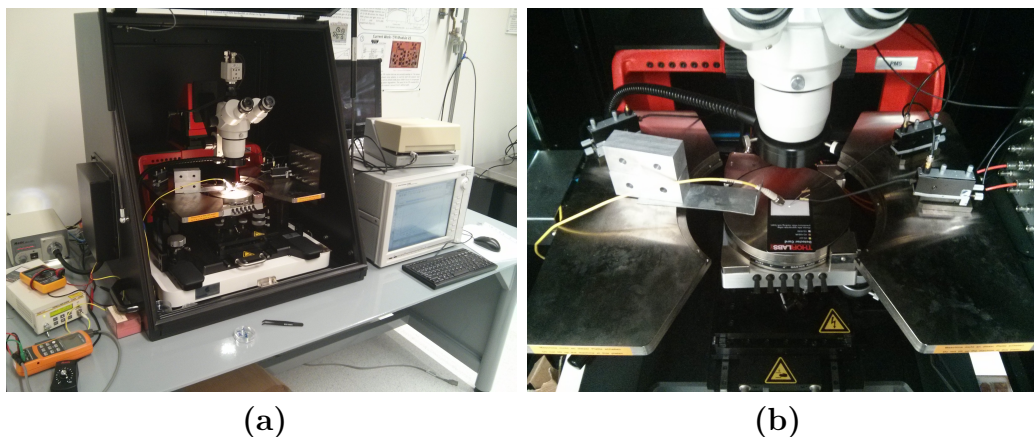


**Figure 37:** Measurement setup (a) EM shielded black box in the middle and semiconductor parameter analyzer on the right (b) DC needle probes

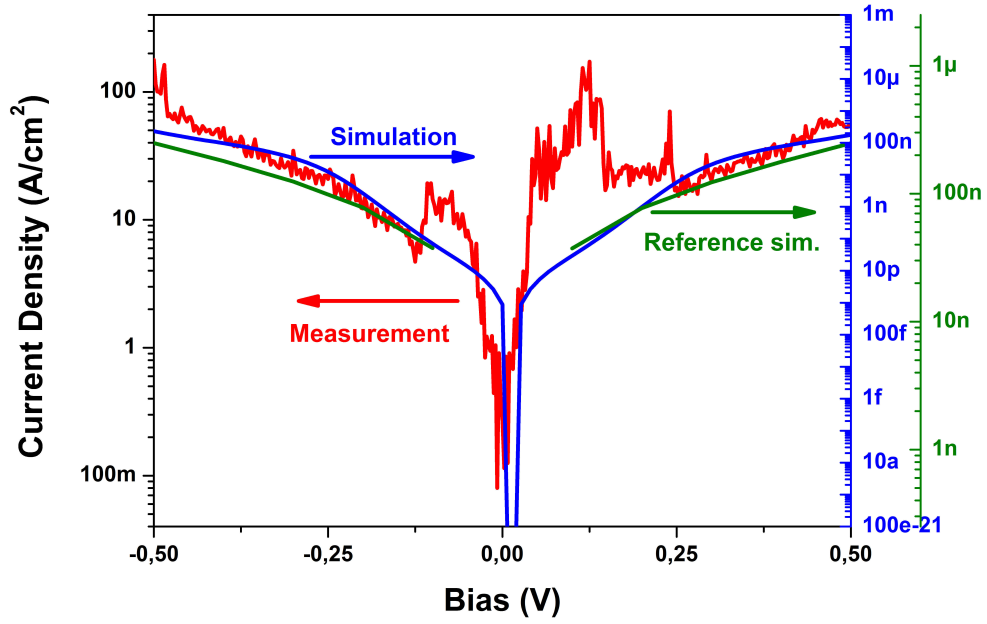


**Figure 38:**  $I-V$  characteristics of MM1:  $Al/Al_2O_3/Cr/Au$ , 2 nm insulator thick MIM diode, measurement is on the left scale and the simulations are on the right scale

## 4.2 Electrical DC Measurements

After the fabrication of MIM diodes, they are immediately measured. The measurements conducted in setup mentioned above. The samples which are shown in the Table 5 are measured. Measurement results from these samples are shown below.

### 4.2.1 MM1 Measurement Results

MM1 sample consists of  $Al/Al_2O_3/Cr/Au$  MIM diode. Thickness of insulator layer  $Al_2O_3$  is 2 nm. The  $I-V$  characteristics of this MIM diode can be seen in Fig. 38. In this diode, the noise is very high, due to the very thin insulator layer and the low uniformity and surface roughness of the insulator layer. Around  $\pm 0.1$  V applied voltage, there is a sharp behavior in the  $I-V$  curve, because the current density become very high for the thickness of the insulator and deformation of features lead to change in the current. Current density is goes up tp 100  $A/cm^2$  around 0.5 V applied voltage. The rectification of the MIM diode is not visible in this  $I-V$  characteristics.

The simulation result of the same MIM structure is also shown in the Fig. 38.

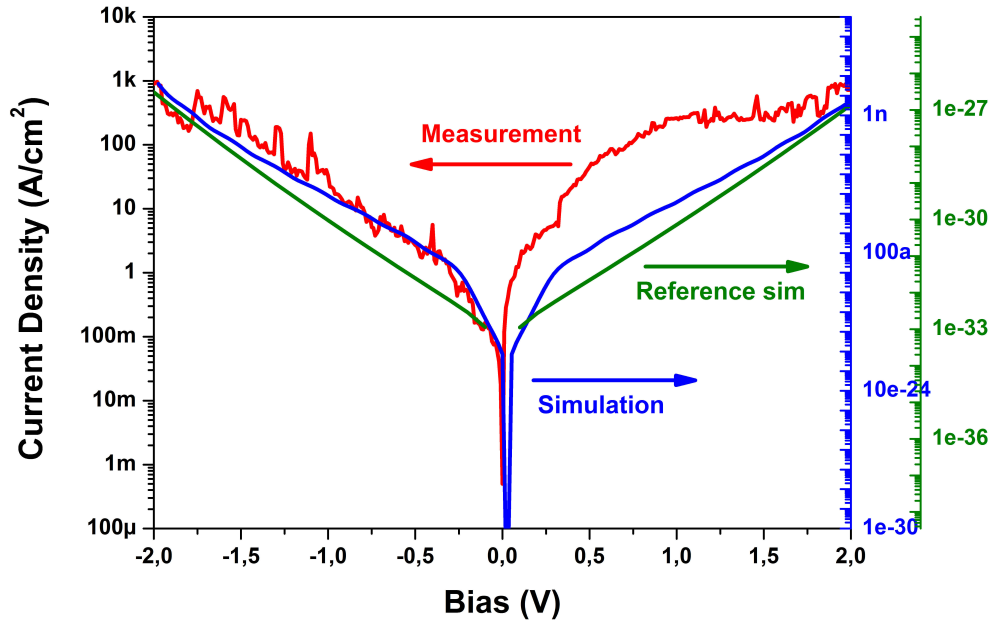


**Figure 39:**  $I-V$  characteristics of MM2:  $Al/Al_2O_3/Cr/Au$ , 5 nm insulator thick MIM diode, measurement is on the left scale and the simulations are on the right scale

The behavior of the simulation and the measurements are similar. However, the measured current density and the simulations have more than  $1 \times 10^{10}$  A/cm<sup>2</sup> difference. The reasons behind this are lacking of uniformity of the films and the change in the physical properties on the nm scale. Very similar behavior is observed simulation in literature [18] which is also in the figure. In this simulation, the difference between the current densities are higher.

#### 4.2.2 MM2 Measurement Results

The sample MM2 is having 5 nm of insulator thickness in  $Al/Al_2O_3/Cr/Au$  MIM structure.  $I-V$  measurements of MM2 is shown in Fig. 39. In this diode, current densities are going up to 1 kA/cm<sup>2</sup> around 2 V applied voltage. High rectification can be seen around  $\pm 0.5$  V applied voltage which is nearly 100 A/A. The noise of the current still there because of the uniformity of the film.

The simulation result's behavior is similar with the measurement results except +1V applied voltage. The difference between simulation and measurement results can be seen in the Fig. 39. Another difference between simulation and measurement results is the levels of current densities. In this case, the difference of current densities

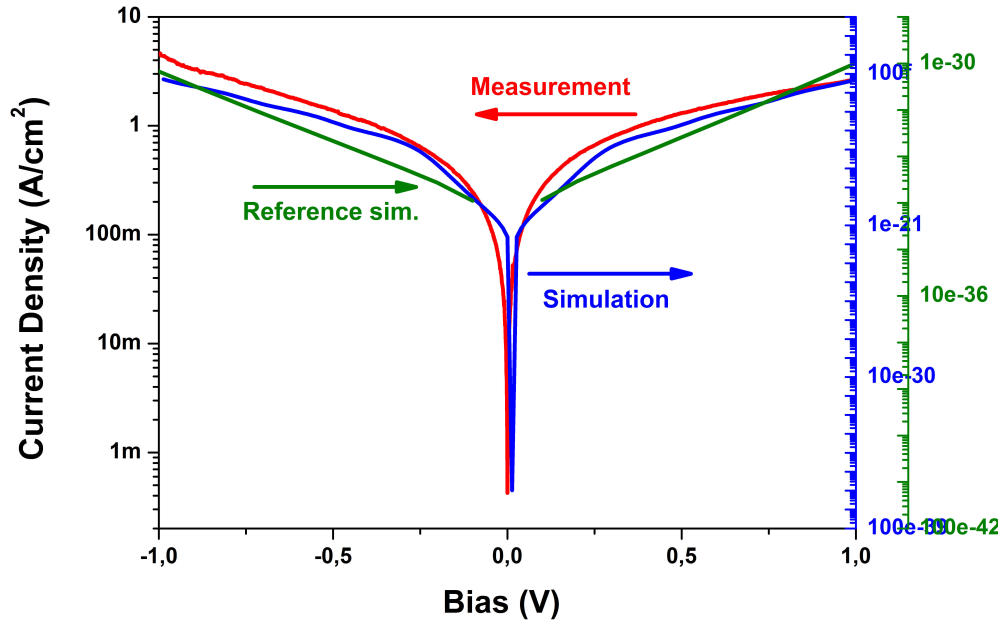


**Figure 40:**  $I - V$  characteristics of MM5:  $Au/Al_2O_3/Al$ , 5 nm insulator thick MIM diode, measurement is on the left scale and the simulations are on the right scale

between simulation and measurement become nearly  $1 \times 10^{12}$  A/cm<sup>2</sup>. other than that, the behavior of simulation and measurement are very similar to each other. Reference [18] simulation behavior is similar with difference on the current density levels

#### 4.2.3 MM5 Measurement Results

MM5 sample consists of  $Au/Al_2O_3/Al$  MIM diode. Thickness of the  $Al_2O_3$  insulator layer is 5 nm. Measurement result of this MIM diode is shown in Fig. 40. Around 1 V applied voltage, the current density level is around 2 A/cm<sup>2</sup>. The smoothness of the surface and the uniformity of the films lead to have smoother curve in this MIM diode different than MM1 and MM2 MIM diodes.

The simulation result is shown in Fig. 40 on the right scale. Beside the scale difference between measurement and simulation result, behavior of the simulation fits with the measurement result. Current density difference in the simulation of MIM diode is around  $1 \times 10^{12}$  A/cm<sup>2</sup>. As in the other diodes shown before, the difference on the current level is high on this type of diode in the simulation given in the literature [18].

#### 4.2.4 LM1 Measurement Results

In the sample LM1, the insulator is  $Cr_2O_3$  and the thickness of the insulator is 5 nm. The measurement results of LM1  $Au/Cr_2O_3/Cr$  MIM diode is shown in Fig. 41. The current density levels are increasing in fast manners, reach up to  $A/cm^2$  around +2 V applied voltage. Additionally, rectification of this MIM diode is approximately A/A in vicinity of  $\pm 1$  V applied bias. The asymmetry in this diode is more than  $Al_2O_3$  diodes in the measurement. The barrier formation in the  $Cr_2O_3$  MIM diode has lower asymmetry like in Fig. 22, however, turn on voltage is effective to give the asymmetry in this diodes which is also seen in the simulations of these two diodes. which is the reverse of the expectations.

Unlike MM1, MM2 and MM5, simulation of LM1 MIM diode does not fit with the measurement results. Measurement results are totally different than the simulation results. This difference caused by the physical properties in the fabricated diode difference. There is always a difference expected in the physical properties of materials between in the ones used in the simulations and the one after fabrication, but the difference in this sample is more than the margins. On the forward direction, the simulation given on the literature [18] shows similar behavior. But still the levels are not close to each other.

#### 4.2.5 LM2 Measurement Results

The sample LM2 is having 5 nm of insulator thickness in  $Au/TiO_2/Ti$  MIM structure.  $I - V$  measurements of LM2 is shown in Fig. 42. In this diode, current densities are going up to  $1 \text{ kA}/cm^2$  around 2 V applied voltage. There is nearly 100 A/A rectification ratio at  $\pm 0.5$  V. The lowest barrier formation which can be seen in Fig. 22 in fabricated MIM structures is in this sample.

The simulations of this type of MIM structure is on the right scale of Fig. 42. In the reverse biases, the simulation behavior and measurement behavior are similar to each other. But in the forward biases, there is visible difference between simulation and measurement. At 2 V applied voltage the current level difference between simulation and measurement is around  $1 \times 10^2 \text{ A}/cm^2$ . Behavior is not similar on simulation in literature [18]. In this simulation, the difference between the current densities are closer.

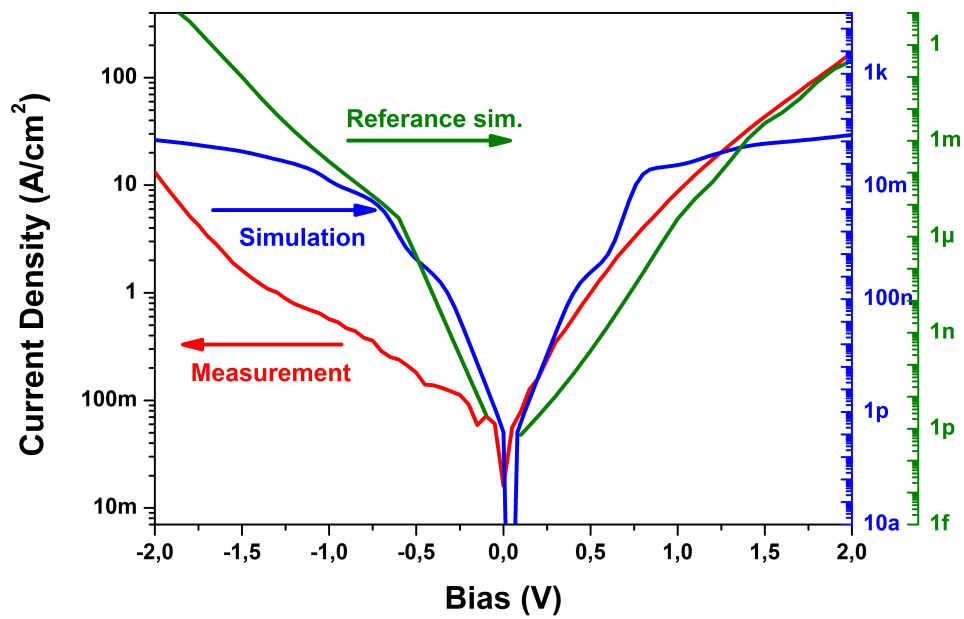


Figure 41:  $I - V$  characteristics of LM1:  $Au/Cr_2O_3/Cr$ , 5 nm insulator thick MIM diode, measurement is on the left scale and the simulations are on the right scale

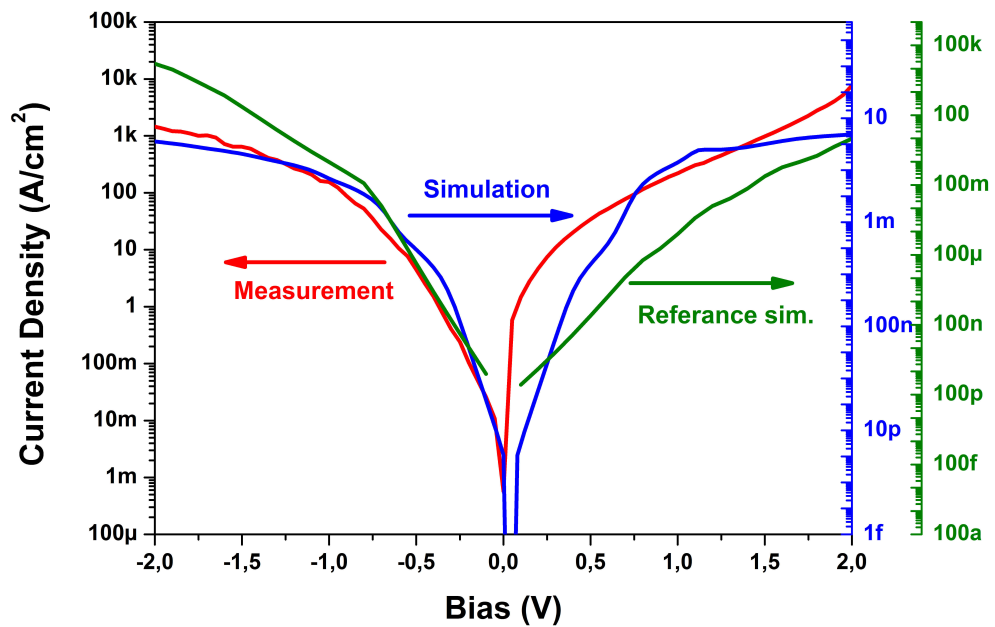
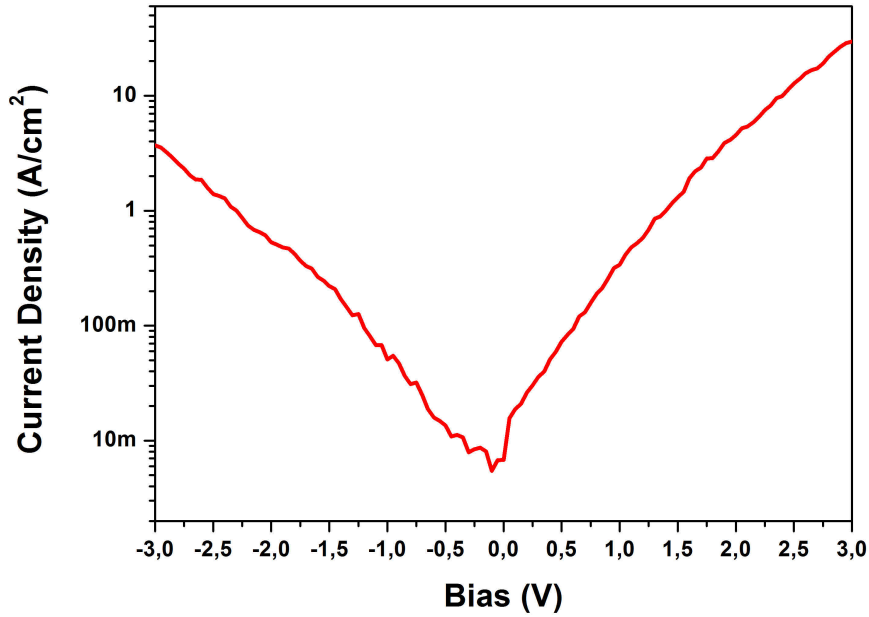


Figure 42:  $I - V$  characteristics of LM2:  $Au/TiO_2/Ti$ , 5 nm insulator thick MIM diode, measurement is on the left scale and the simulations are on the right scale



**Figure 43:**  $I - V$  characteristics of LM3:  $Au/Al_2O_3/TiO_2/Ti$ , 2.5/2.5 nm insulator thick MIIM diode. MIIM type of diode simulations are not available

#### 4.2.6 LM3 Measurement Results

LM3 sample is MIIM tunneling diode sample with materials  $Au/Al_2O_3/TiO_2/Ti$ . There are two different insulators stacked between metals and the thicknesses of the insulators are 2.5 nm and 2.5 nm. The measurement result of LM4 sample is shown in Fig. 43. In this sample it is tried to see the effect of the double insulator formation. It is expected that these type of the diodes are having more current than the other formations due to the step barrier and the resonance formation at the junction of two insulators. In this sample, it can be seen that the current density measured more than  $10 \text{ A/cm}^2$  at +3 V applied voltage. The rectification of this diode is lower than 10 A/A and it is lower with respect to the samples above.

#### 4.2.7 LM4 Measurement Results

The material set in LM4 sample is  $Au/Al_2O_3/Cr$ . The thickness of the insulator  $Al_2O_3$  is 5 nm. The measured  $I - V$  characteristics are shown in Fig. 44. At +3 V applied bias, the current density is around  $30 \text{ A/cm}^2$ . The rectification ratio of the MIM diode is not visible from the measurements. Around 0 V bias, noise in the

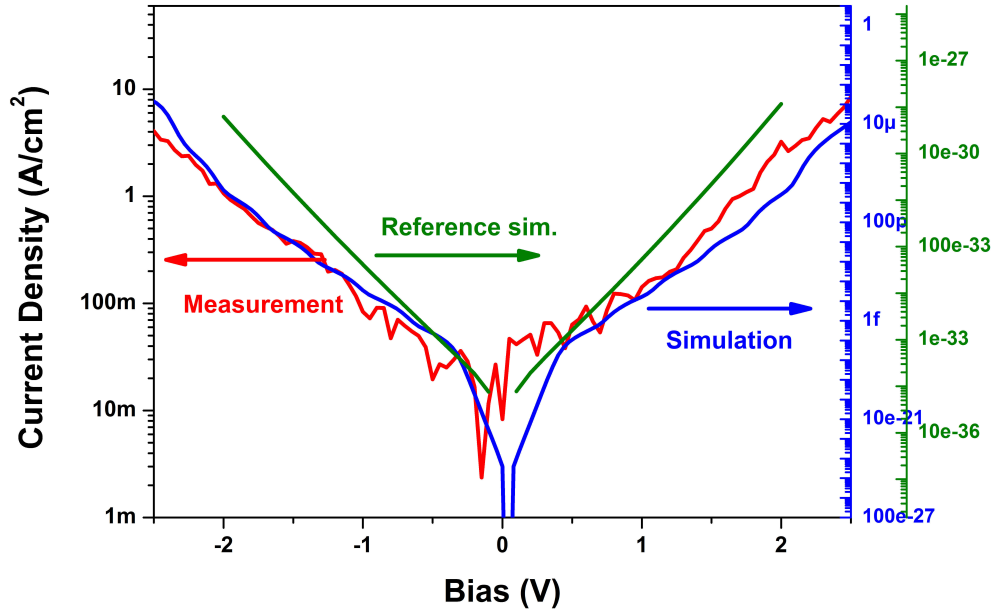


**Figure 44:**  $I - V$  characteristics of LM4:  $Au/Al_2O_3/Cr$ , 5 nm insulator thick MIM diode, measurement is on the left scale and the simulations are on the right scale

current density is high. At that region, the tunneling probability of an electron is low due to high energy barrier at the insulator which can be seen in the Fig. 22.

The simulation of the same MIM structure is also in Fig. 44. Except the current level difference which is more than  $1 \times 10^6$  A/cm<sup>2</sup>, the behavior in the simulation is similar to measurement. Turn on voltages of the MIM diode in the simulations and the measurements fit to each other. The current level in the simulation in [18] is nearly  $10^{30}$  A/cm<sup>2</sup> difference even though the behaviors are similar.

#### 4.2.8 LMC Measurement Results

LMC sample is another MIIM tunneling diode sample with materials  $Cr/Cr_2O_3/TiO_2/Ti$ . The insulators in this structure have 2.5 nm and 2.5 nm thicknesses. In Fig. 45, it is shown that the measurement results of the MIIM diode on LMC sample. The current density in this sample is higher than other fabricated diodes. Even in the +0.5 V applied bias to the MIM diode, the current density of the diode is around 20 kA/cm<sup>2</sup>. From the figure, it is seen that the diode is nearly symmetric due to the low barrier height. In low barrier structures like this MIM diode, asymmetry is low due to the high tunneling probabilities and easy overcoming to insulator barrier.

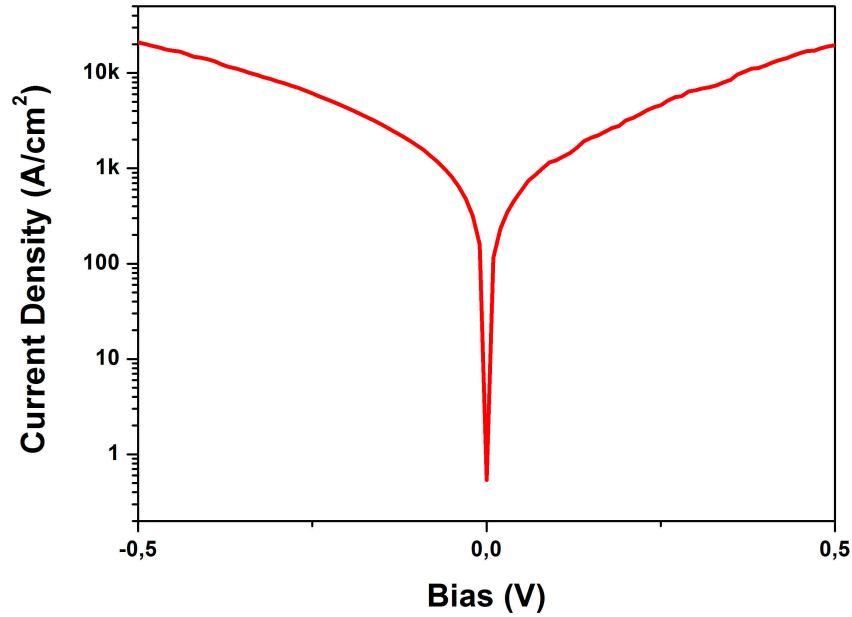


**Figure 45:**  $I - V$  characteristics of LMC:  $Cr/Cr_2O_3/TiO_2/Ti$ , 2.5/2.5 nm insulator thick MIIM diode. MIIM type of diode simulations are not available

It can be seen in the measurement results that the simulations are not in the range of the measurements. In thinner insulators, the current density tends to be high rather than thicker insulators. Additionally, higher barriers lead to high rectification ratios. But due to the low tunneling probabilities in the high barrier structures, current levels are low in these MIM diodes.

### 4.3 Electrical DC Characteristics

Electrical DC characteristics of the MIM diodes are extracted from their measured  $I - V$  curves. The DC characteristics of the MIM diodes which are resistance, non-linearity and responsivity are shown below.

#### 4.3.1 Resistance

Resistance of the MIM diodes are extracted from their  $I - V$  according to (10). It is important for a MIM diode to have low resistance to match to antenna for maximum power transfer. The matching also leads in the rectenna to have maximum

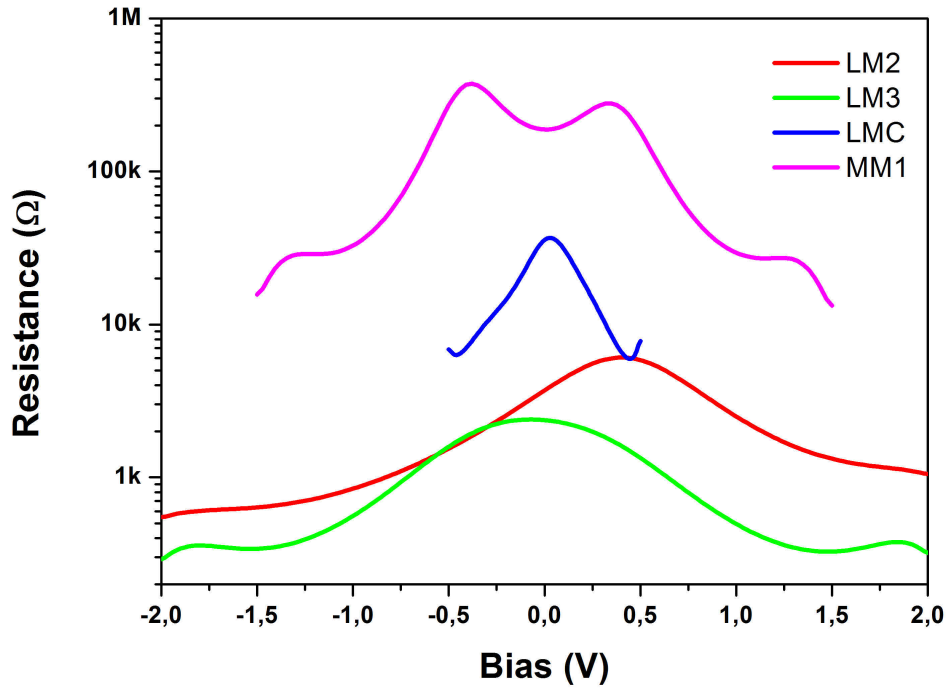


**Figure 46:** Resistance graph of lowest four resistive fabricated MIM diodes

efficiency. In the Fig. 46, resistance of lowest four resistive fabricated MIM diode is shown.

It is clear from the figure that, MIM diodes behave like other diodes and as applied bias increases, the resistance of the diode decreases. The highest resistance of the diodes is around 0 V applied bias. The lowest 0V applied bias is from LM3 sample which is  $Au/Al_2O_3/TiO_2/Ti$  MIIM diode. The 0 V resistance of this diode is around 2 kΩ.

Im LC sample which consists of  $Cr/Cr_2O_3/TiO_2/Ti$  MIIM structure have 35 kΩ 0 V resistance. It is not coincidence the fabricated two MIIM structures are shown in the four lowest resistive diodes. The step barrier increases the tunneling current and the decreases the resistance of the diode.

Additionally, the resistance decreases with the barrier height. In LM2 diode which consists of  $Au/TiO_2/Ti$  MIM structure have the lowest energy barrier at the insulator which can be seen in the Fig. 22. Therefore, the resistance of this MIM diode is also low in the order of 3 kΩ 0 V resistance.

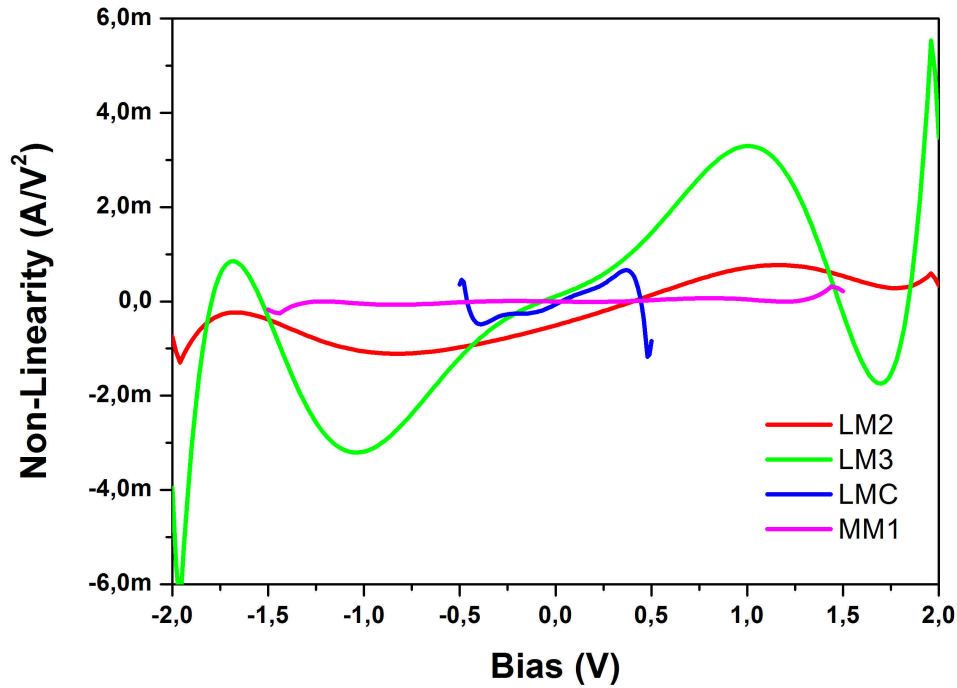


**Figure 47:** Non-linearity graph of lowest four resistive fabricated MIM diodes

### 4.3.2 Non-linearity

Non-linearity measures the non-linear behavior of a diode. This characteristics are extracted from  $I - V$  curve of fabricated MIM diode using (11). Highest non-linearity means highest rectification by the diode. Hence, high rectenna efficiencies can be reach only by highly non-linear MIM and MIIM diodes. The non-linearity of lowest four resistive fabricated MIM diodes are shown in Fig. 47.

It is seen from the graph that the non-linearity of the diodes are in the order of  $\text{mA}/\text{V}^2$ . The highest non-linearity is  $3.29 \text{ mA}/\text{V}^2$  at  $1.02 \text{ V}$  applied bias which is coming from LM3 sample. The step in the potential barriers of  $\text{Au}/\text{Al}_2\text{O}_3/\text{TiO}_2/\text{Ti}$  creates this non-linearity.

As the asymmetry of the energy levels increases, the non-linearity of the diode increases which can be seen in the difference in non-linearities of sample MM1 and LM2. The asymmetry in the LM2 is higher than MM1, hence the non-linearity of LM2 is higher. There is more than 10 times difference in the non-linearities of these two structures.

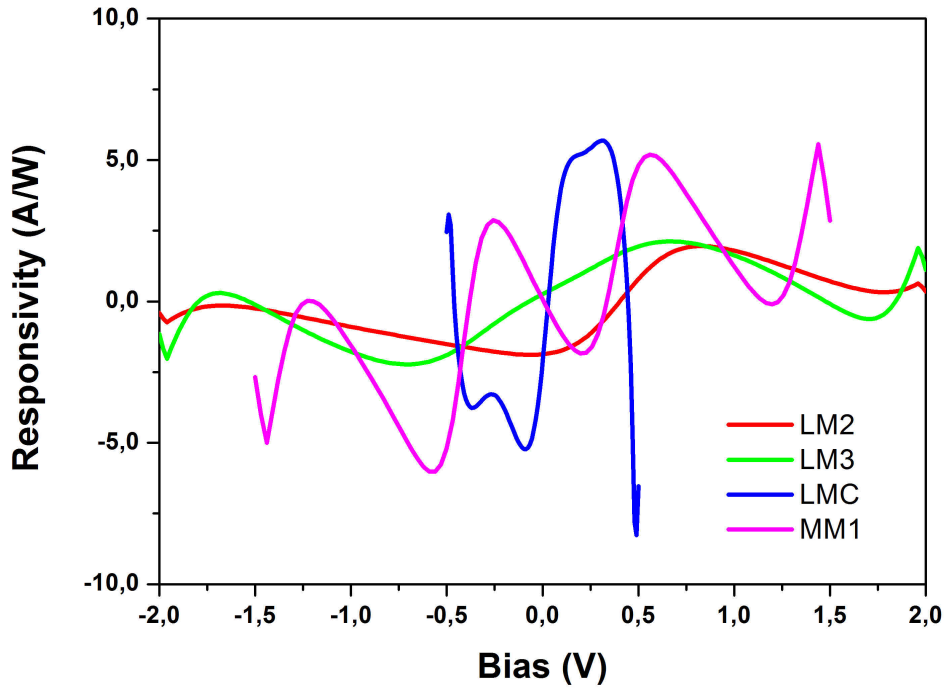


Figure 48: Responsivity graph of lowest four resistive fabricated MIM diodes

### 4.3.3 Responsivity

It is required for highly efficiency rectennas that to have highly responsive MIM diodes according to (18). The responsivity of MIM diodes are extracted from measured  $I - V$  curve by using (12). The extracted responsivity of values of lowest four resistive fabricated MIM diodes are shown in Fig. 48.

The responsivity of the MIM diodes are oscillating around 0 V applied bias. The highest responsivity is reached by MM1 diode at -0.56 V applied bias as -6.02 A/W. From (12) linear relation of resistance and responsivity can be seen. Hence, it is clear that the highest responsivity is reached by the highest resistive diode in these four.

Additionally, barrier formations play important role in the responsivity. In MM1, the MIM type is  $Al/Al_2O_3/Cr/Au$  which the potential barriers is high. The other diodes have lower insulator barriers.

The MIM diode characteristics can be seen in the Table 6. As a result of characteristic extractions, it can be said that the barrier formations play very crucial role

in MIM diode electrical DC characteristics. Higher barriers like in MM1 sample, result as higher resistance and higher responsivity. Non-linearity is directly affected by the asymmetry of the barrier formation.

#### 4.4 Efficiency Calculations

The efficiency of rectenna is calculated assuming that simulated antennas are coupled with the fabricated MIM diodes. In this assumption, it is neglected the  $f_c$  of the fabricated diodes. The efficiency of the rectenna is calculated at 60 THz ( $5\mu\text{m}$ ). Incident EM radiation is at direct angle with the antenna and the EM is coherent source.

The antenna that is coupled to the diode is taken to be the half-wave dipole antenna in Fig. 10. The efficiency of this antenna is 95%. Metal losses due to the conduction and high frequency components are taken as zero, therefore  $\eta_s=1$ . From (18), maximum calculated efficiency is 12% from LM3 MIIM diode. Other MIIM diode is having 3% efficiency which is LMC sample. Additionally, calculated efficiency of LM2 sample is 3.5%. These three diodes are the ones that can exceed 1% calculated efficiency. Other diodes have poor efficiencies which can be seen in the Table 6.

Similar to the diode characteristics, in the efficiency calculations, the effect of low barrier or step barrier is observable. The MIM structures with low insulator barrier heights have better characteristics and better efficiency. For example the sample LM2 has lower barrier heights than others, and the efficiency of this diode is high than many others. Likewise lower barriers, step barriers in double insulators increases the efficiency of the rectenna. In LM3 and LMC samples, it is clearly seen that the efficiency of the rectenna is higher. As it mentioned before, the reason behind this is first the step barrier and resonance formation at insulator-insulator junction which facilitates tunneling. Comparisons between single insulator, double insulator and barrier heights can be done from Table 6.

**Table 6:** Fabricated MIM diode characteristics and calculated efficiencies

Diode Name	MIM Type	MIM Area [ $\mu\text{m}^2$ ]	Insulator Thickness [nm]	0 V Responsivity [ $\text{V}^{-1}$ ]	Maximum Responsivity [ $\text{V}^{-1}$ ]	0V Resistance [ $\Omega$ ]	Calculated Maximum Efficiency
MM2	<i>Al/Al<sub>2</sub>O<sub>3</sub>/Cr/Au</i>	1.3	5	0.99	-4.36	1.46 G	<0.01%
MM5	<i>Au/Al<sub>2</sub>O<sub>3</sub>/Al</i>	1.3	5	-1.56	3.79	9.7 G	<0.01%
LM1	<i>Au/Cr<sub>2</sub>O<sub>3</sub>/Cr</i>	0.02	5	0.32	5.178	6.4 G	<0.1%
LM2	<i>Au/TiO<sub>2</sub>/Ti</i>	0.45	5	-1.87	1.95	3.6 k	3.5%
LM3	<i>Au/Al<sub>2</sub>O<sub>3</sub>/TiO<sub>2</sub>/Ti</i>	0.45	2.5+2.5	0.29	-2.23	2.3 k	12%
LM4	<i>Au/Al<sub>2</sub>O<sub>3</sub>/Cr</i>	0.02	5	1.8	4.1	79 G	<0.01%
LMC	<i>Cr/Cr<sub>2</sub>O<sub>3</sub>/TiO<sub>2</sub>/Ti</i>	0.212	2.5+2.5	-2.5	5.68	35 k	3%

## 5 Conclusion & Future Work

### 5.1 Summary of Work

Rectennas are one of the most potential candidate for future energy harvesting and detection applications. Easy fabrication, small size, fast response, high efficiency availability and cheaper costs are the reasons behind that. Harvesting applications require high efficiency in small areas with low cost. In detection applications, the tunability and the size of the rectennas are the main concerns. Additionally filling the THz gap is important for future high speed technologies. Therefore rectennas are the most potent candidate.

In this thesis, it is aimed to model, design and fabricate MIM diodes for infrared energy harvesting and detection applications with high rectenna efficiencies to fill the gap. Initially literature search on antennas which is working on the high frequency is conducted. Coupled of antennas are simulated at 60 THz, later efficiency and bandwidth of these antennas are collected. In order to use these antennas in harvesting applications, it is required wide band highly efficient antennas. Hence, the antenna characteristics tried to be improved. Most efficient simulated antenna has 95% efficiency over 10 THz bandwidth. This antenna is taken to be coupled with the MIM diode in rectenna element.

After the antennas, MIM diodes are modeled and simulated to observe the behavior of the diodes. Parametric analysis are conducted on the MIM diodes and the required physical property range is extracted according to the application of MIM diodes. Later material set for MIM structure is selected and these structures are conducted. In the selection procedure, beside the MIM diode performance, easy and well-known fabrication are considered as well as the IC compatibility of the materials.

Simulated MIM diodes are fabricated in Sabanci University cleanroom facilities.  $Al/Al_2O_3/Cr/Au$ ,  $Au/Cr_2O_3/Cr$  and  $Au/TiO_2/Ti$  MIM diodes are fabricated. Additionally  $Au/Al_2O_3/TiO_2/Ti$  and  $Cr/Cr_2O_3/TiO_2/Ti$  MIIM diode is also fabricated. The  $I - V$  characteristics are measured and the diode characteristics are extracted from these measurement results. -6.02 A/W and 5.68 A/W responsivities are reached from fabricated diodes. The 0 V resistances of the diodes are dropped

to 2.3 k $\Omega$ . With these characteristics, rectennas using these diodes reach to 12% efficiency in  $Au/Al_2O_3/TiO_2/Ti$  diode. These results show that these diodes are capable of operating as energy harvester and detectors.

## 5.2 Future Work

Fabricated diodes are based on the MIM diode modeling and simulations. In the simulations, the lacking of double insulator formation and limitations on the parametric analysis have to be improved in the first stage. Additionally, the most important improvement on the MIM diode simulations is fitting the measurement results to the simulation results. Still there is more than  $1 \times 10^{10}$  A/cm<sup>2</sup> difference between simulations and measurement results. There has to be a correlative coefficient to fix the problem. Other than that, the  $I - V$  behavior of the simulations are fitting with the measurement results.

It is seen in the measurement results and characteristics extraction that step barrier and low barrier are suitable for the rectenna elements. It has to be more fabrication on the low barrier MIM diodes and MIIM diodes in order to increase the efficiency. The reason behind this is the impedance matching between antenna and the diode has to be precise for high rectenna efficiencies.

On the long term plan, optical measurements of the rectennas have to be conducted. The efficiencies on this thesis only calculated values. The exact values can be found by optical measurements. Later, array formation of rectennas has to be investigated, fabricated and measured.

## References

- [1] N. M. Miskovsky, P. H. Cutler, A. Mayer, B. L. Weiss, B. Willis, T. E. Sullivan, and P. B. Lerner, “Nanoscale devices for rectification of high frequency radiation from the infrared through the visible: a new approach,” *Journal of Nanotechnology*, vol. 2012, 2012.
- [2] M. A. Green, “Third generation photovoltaics: Ultra-high conversion efficiency at low cost,” *Progress in Photovoltaics*, vol. 9, no. 2, pp. 123–135, 2001.
- [3] A. Rogalski, “Infrared detectors: status and trends,” *Progress in quantum electronics*, vol. 27, no. 2, pp. 59–210, 2003.
- [4] G. Moddel, *Will rectenna solar cells be practical?*, pp. 3–24. Springer, 2013.
- [5] M. R. Abdel-Rahman, B. Monacelli, A. R. Weeks, G. Zummo, and G. D. Boreman, “Design, fabrication, and characterization of antenna-coupled metal-oxide-metal diodes for dual-band detection,” *Optical Engineering*, vol. 44, no. 6, pp. 066401–066401–7, 2005.
- [6] S. Grover and G. Moddel, “Applicability of metal/insulator/metal (mim) diodes to solar rectennas,” *Photovoltaics, IEEE Journal of*, vol. 1, no. 1, pp. 78–83, 2011.
- [7] S. Krishnan, H. La Rosa, E. Stefanakos, S. Bhansali, and K. Buckle, “Design and development of batch fabricatable metal–insulator–metal diode and microstrip slot antenna as rectenna elements,” *Sensors and Actuators A: Physical*, vol. 142, no. 1, pp. 40–47, 2008.
- [8] M. Gadalla, M. Abdel-Rahman, and A. Shamim, “Design, optimization and fabrication of a 28.3 thz nano-rectenna for infrared detection and rectification,” *Scientific reports*, vol. 4, 2014.
- [9] Z. Zhu, S. Joshi, and G. Moddel, “High performance room temperature rectenna ir detectors using graphene geometric diodes,” *Selected Topics in Quantum Electronics, IEEE Journal of*, vol. 20, no. 6, pp. 70–78, 2014.
- [10] E. Okress, W. Brown, T. Moreno, G. Goubau, N. Heenan, and R. George, “Microwave power engineering,” *Spectrum, IEEE*, vol. 1, no. 10, pp. 76–76, 1964.
- [11] W. C. Brown, “The history of the development of the rectenna,” 1980.
- [12] S. Marchetti, P. Sandri, and R. Simili, “Theoretical and experimental responsivity of fir antenna coupled metal-insulator-metal detectors,” *International Journal of Infrared and Millimeter Waves*, vol. 18, no. 7, pp. 1395–1409, 1997.
- [13] E. Grossman, “Lithographic antennas for submillimeter and infrared frequencies,” 1995.
- [14] C. Fumeaux, W. Herrmann, F. Kneubühl, and H. Rothuizen, “Nanometer thin-film ni–nio–ni diodes for detection and mixing of 30 thz radiation,” *Infrared physics and technology*, vol. 39, no. 3, pp. 123–183, 1998.

- [15] K. Singh and S. Hammond, “Current-voltage characteristics and photoresponse of metal al<sub>2</sub>o<sub>3</sub> metal devices,” *Turkish Journal of Physics*, vol. 22, pp. 315–323, 1998.
- [16] B. J. Eliasson, *Metal-insulator-metal diodes for solar energy conversion*. Thesis, 2001.
- [17] S. Krishnan, E. Stefanakos, and S. Bhansali, “Effects of dielectric thickness and contact area on current–voltage characteristics of thin film metal–insulator–metal diodes,” *Thin Solid Films*, vol. 516, no. 8, pp. 2244–2250, 2008.
- [18] S. Grover and G. Moddel, “Engineering the current–voltage characteristics of metal–insulator–metal diodes using double-insulator tunnel barriers,” *Solid-State Electronics*, vol. 67, no. 1, pp. 94–99, 2012.
- [19] K. R. Jha and G. Singh, “Terahertz dipole antenna in fabry-perot cavity with two side-walls to enhance the directivity,” *35th International Conference on Infrared, Millimeter, and Terahertz Waves (Imm-THz 2010)*, 2010.
- [20] E. Briones, J. Alda, and F. J. González, “Conversion efficiency of broad-band rectennas for solar energy harvesting applications,” *Optics express*, vol. 21, no. 103, pp. A412–A418, 2013.
- [21] C. Feuillet-Palma, Y. Todorov, A. Vasanelli, and C. Sirtori, “Strong near field enhancement in thz nano-antenna arrays,” *Scientific Reports*, vol. 3, 2013.
- [22] M. Abdel-Rahman, F. Gonzalez, and G. Boreman, “Antenna-coupled metal-oxide-metal diodes for dual-band detection at 92.5 ghz and 28 thz,” *Electronics Letters*, vol. 40, no. 2, pp. 116–118, 2004.
- [23] J. W. Haus, L. Li, N. Katte, C. Deng, M. Scalora, D. de Ceglia, and M. A. Vincenti, “Nanowire metal-insulator-metal plasmonic devices,” 2013.
- [24] M. Bareiß, B. N. Tiwari, A. Hochmeister, G. Jegert, U. Zschieschang, H. Klauk, B. Fabel, G. Scarpa, G. Koblmüller, and G. H. Bernstein, “Nano antenna array for terahertz detection,” *Microwave Theory and Techniques, IEEE Transactions on*, vol. 59, no. 10, pp. 2751–2757, 2011.
- [25] A. M. Sabaawi, C. C. Tsimenidis, and B. S. Sharif, *Overview of Nanoantennas for Solar Rectennas*, pp. 231–256. Springer, 2013.
- [26] V. Varlamava, F. Palma, P. Nenzi, and M. Balucani, “Electric field enhancement in 3-d tapered helix antenna for terahertz applications,” *Terahertz Science and Technology, IEEE Transactions on*, vol. 4, no. 3, pp. 360–367, 2014.
- [27] C. Kim, D. J. Arenas, D. B. Tanner, and Y.-K. Yoon, “Micromachined air-lifted pillar arrays for terahertz devices,” *Electron Device Letters, IEEE*, vol. 35, no. 4, pp. 470–472, 2014.
- [28] C. A. Balanis, *Antenna theory: analysis and design*, vol. 1. John Wiley and Sons, 2005.

- [29] J. D. Livingston, *Electronic properties of engineering materials*. Wiley New York, NY, 1999.
- [30] F. Yesilkoy, S. Potbhare, N. Kratzmeier, A. Akturk, N. Goldsman, M. Peckerar, and M. Dagenais, *A Mid-IR Antenna Integrated with a Geometrically Asymmetrical Metal-Insulator-Metal Rectifying Diode*, pp. 163–188. Springer, 2013.
- [31] J. G. Simmons, “Electric tunnel effect between dissimilar electrodes separated by a thin insulating film,” *Journal of Applied Physics*, vol. 34, no. 9, pp. 2581–2590, 1963.
- [32] M. Dagenais, K. Choi, F. Yesilkoy, A. N. Chryssis, and M. C. Peckerar, “Solar spectrum rectification using nano-antennas and tunneling diodes,” *Optoelectronic Integrated Circuits Xii*, vol. 7605, 2010. Proceedings of SPIE.
- [33] J. F. Conley Jr and N. Alimardani, *Impact of Electrode Roughness on Metal-Insulator-Metal (MIM) Diodes and Step Tunneling in Nanolaminate Tunnel Barrier Metal-Insulator-Insulator-Metal (MIIM) Diodes*, pp. 111–134. Springer, 2013.
- [34] J. Bean, A. Weeks, and G. D. Boreman, “Performance optimization of antenna-coupled tunnel diode infrared detectors,” *Quantum Electronics, IEEE Journal of*, vol. 47, no. 1, pp. 126–135, 2011.
- [35] S. Krishnan, Y. Emirov, S. Bhansali, E. Stefanakos, and Y. Goswami, “Thermal stability analysis of thin film ni-niox-cr tunnel junctions,” *Thin Solid Films*, vol. 518, no. 12, pp. 3367–3372, 2010.
- [36] K. Choi, F. Yesilkoy, A. Chryssis, M. Dagenais, and M. Peckerar, “New process development for planar-type cic tunneling diodes,” *Electron Device Letters, IEEE*, vol. 31, no. 8, pp. 809–811, 2010.
- [37] S. Krishnan, S. Bhansali, E. Stefanakos, and Y. Goswami, “Thin film metal-insulator-metal junction for millimeter wave detection,” *Proceedings of the Eurosensors Xxiii Conference*, vol. 1, no. 1, pp. 409–412, 2009.
- [38] Z. X. Zhu, S. Joshi, S. Grover, and G. Moddel, “Graphene geometric diodes for terahertz rectennas,” *Journal of Physics D-Applied Physics*, vol. 46, no. 18, 2013. 127ZL Times Cited:11 Cited References Count:29.
- [39] J. G. Simmons, “Generalized formula for the electric tunnel effect between similar electrodes separated by a thin insulating film,” *Journal of Applied Physics*, vol. 34, no. 6, pp. 1793–1803, 1963.
- [40] A. S. Sedra and K. C. Smith, *Microelectronic Circuits*. New York: Oxford University Press, 2011.
- [41] D. V. Ragone, *Thermodynamics of Materials, Volume 1*, vol. 1 of *Materials Science and Engineering*. New Jersey: John Wiley and Sons, 1994.
- [42] P. Landsberg and G. Tonge, “Thermodynamics of the conversion of diluted radiation,” *Journal of Physics A: Mathematical and General*, vol. 12, no. 4, p. 551, 1979.

- [43] S. M. Sze, *Physics of Semiconductor Devices*. John Wiley and Sons, 2nd ed., 1981.
- [44] D. J. Griffiths, *Introduction to quantum mechanics*. Pearson Education, 2nd ed., 2005.
- [45] B. Jonsson and S. T. Eng, “Solving the schrodinger-equation in arbitrary quantum-well potential profiles using the transfer-matrix method,” *Ieee Journal of Quantum Electronics*, vol. 26, no. 11, pp. 2025–2035, 1990. Et605 Times Cited:144 Cited References Count:25.
- [46] O. M. Probst, “Tunneling through arbitrary potential barriers and the apparent barrier height,” *American Journal of Physics*, vol. 70, no. 11, pp. 1110–1116, 2002. 605KQ Times Cited:5 Cited References Count:15.

# Appendix

## A1 MATLAB Diode Model

```
1  clc ;
2  clear all ;
3  tic
4  global kb m h hJ hbar eps0 q kJ hbarJ ;
5  kb=8.6173324e-5;
6  m=9.109e-31;
7  h=4.135e-15;
8  hJ=6.62606957e-34;
9  hbar=h/(2*pi);
10 hbarJ=hJ/(2*pi);
11 eps0=8.854e-12;
12 q=1.6022176565e-19;
13 kJ=1.3806488e-23;
14
15 %%%
16 global thickness Ef num phileft phiright T eps;
17
18 %%%%%%%%%%%%%%%%%%%%%%%%%%%%%%%%%%%%%%%%%%%%%%%%%%%%%%%%%%%%%%%%%%%%%%%%%% ONLY CHANGE THESE PARAMS
19 %%%%%%%%%%%%%%%%%%%%%%%%%%%%%%%%%%%%%%%%%%%%%%%%%%%%%%%%%%%%%%%%%%%%%%%%%%
19 Vapplow=-3; % [v] lowest applied
20 % voltage
20 topdata=2*abs(Vapplow); % highest applied
21 % voltage abs. value of low
21 Vappx=Vapplow; % initialization of
22 % applied voltage
22 thickness=50e-10; % [m] thickness of the
23 % insulating layer
23 eps=90; % [#] relative
24 % dielectric constant of the insulating material
24 phileft=0.42; % [eV] left barrier
25 % height {(fermi nergy of the Metal 1) - (electron affinity
26 % of the insulator) }
25 phiright=1.2; % [eV] right barrier
26 % height {(fermi nergy of the Metal 2) - (electron affinity
27 % of the insulator) }
26 Ef=5.6; % [eV] Fermi energy of
27 % the Metal 1
27 T=300; % [K] temperature
28 num=25; % [#] barrier division
29 % number
30 %
31 %%%%%%%%%%%%%%%%%%%%%%%%%%%%%%%%%%%%%%%%%%%%%%%%%%%%%%%%%%%%%%%%%%%%%%%%%%
```

```

31 coeff=1e-14*(4*pi*m*q)/(hJ*h*h);
32 Jther=0;
33 datapoint=150;
34 for (a=1:datapoint)
35 %%%%%%%%%%%%%%%%%%%%%%%%%%%%%%%%%%%%%%%%%%uncomment for two sided
36 if (Vappx>=0)
37
38     J(a)=coeff*transfermatrix(Vappx);
39 else
40     J(a)=-coeff*transfermatrix(Vappx);
41 end
42     Vappx=Vappx+(topdata/datapoint);
43
44     VW(a)=Vappx;
45 end

```

## A1.1 MATLAB Transfer Matrix Method

```

1
2
3 function [prob] = transfermatrix(Vappx)
4 global m hbar thickness num Ef hbarJ;
5
6 %%%%%%%%%%%%%%%%%%%%%%%%%%%%%%%%%%%%%%%%%%uncomment for two sided
7 if (Vappx>=0)
8     Vappx1=Vappx;
9 else
10    Vappx1=-Vappx;
11 end
12 %%%%%%%%%%%%%%%%%%%%%%%%%%%%%%%%%%%%%%%%%%
13 Ex=0;
14 if (Ex==Ef)
15     Ex=Ef+0.0001;
16 end
17 rows=num*2;
18 cols=rows;
19 thickness2=thickness*1e9;
20 matnum=100;
21 dn=thickness2/num;
22 dtn(1)=0;
23 for (j=1:num)
24     dtn(j+1)=dtn(j)+dn;
25 end
26
27 for (j=1:matnum)
28
29     dEx=35/matnum;
30     k0=sqrt(((2*m/(hbar*hbar))*(Ex-Ef)));
31     kn=sqrt(((2*m/(hbar*hbar))*(Ex-Ef+Vappx1)));
32     for (l=1:num)
33         kk(l)=sqrt(((2*m/(hbar*hbar))*(barrier(j, l, Vappx)-
34             Ex+Ef)));
35
36     M=zeros(rows, cols);
37     X=zeros(rows, 1);
38     A=zeros(rows, 1);
39
40     for (n=1:num)
41         for (r=1:rows)
42             for (c=1:cols)
43                 if (r==2*n-1)&&(c==2*n)&&(n~=num)
44                     M(r, c)=-exp(-kk(n+1)*dtn(n));
45                 elseif (r==2*n-1)&&(c==2*n+1)&&(n~=num)

```

```

46         M(r , c)=-exp ( kk (n+1)*dtn (n) ) ;
47     elseif ( r==2*n)&&(c==2*n)&&(n~=num)
48         M(r , c)=(kk (n+1)) *exp (-kk (n+1)*dtn (n) ) ;
49     elseif ( r==2*n)&&(c==2*n+1)&&(n~=num)
50         M(r , c)=(-kk (n+1)) *exp ( kk (n+1)*dtn (n) ) ;
51     elseif ( r==2*n-1)&&(c==2*n-2)&&(n~=1)
52         M(r , c)=exp (-kk (n) *dtn (n) ) ;
53     elseif ( r==2*n-1)&&(c==2*n-1)&&(n~=1)
54         M(r , c)=exp ( kk (n) *dtn (n) ) ;
55     elseif ( r==2*n)&&(c==2*n-2)&&(n~=1)
56         M(r , c)=(-kk (n) ) *exp (-kk (n) *dtn (n) ) ;
57     elseif ( r==2*n)&&(c==2*n-1)&&(n~=1)
58         M(r , c)=(kk (n) ) *exp ( kk (n) *dtn (n) ) ;
59     end
60     end
61 end
62 end
63
64 M(1 , 1) =1;
65 M(2 , 1)=1i*k0 ;
66 M(rows -1, cols )=-exp (-1i*kn*thickness2) ;
67 M(rows , cols )=1i*kn*exp (-1i*kn*thickness2) ;
68
69 X(1 , 1) =-1;
70 X(2 , 1)=1i*k0 ;
71
72 A=inv (M) *X;
73
74 ff=fermicalc (Ex, Vappx) ;
75
76 TM(j)=(abs (kn/k0) ) *(abs (A(rows , 1) ) *abs (A(rows , 1) ) ) ;
77
78 TT(j)=TM(j) *dEx* ff ;
79
80 prob=sum (TT) ;
81 Ex=Ex+dEx ;
82
83 end
84 end

```

## A1.2 MATLAB Effective Potential Barrier Calculation

```

1 function [barrierreturn] = barrier (jet , ret , Vappx)
2 global thickness num q eps0 phileft phiright eps;
3
4 thickness1=thickness;
5 if (Vappx>=0) %
6     %%%%%%%%%%%%%%%%%%%%%%%%%%%%%%%%%%%%%%%%%%%%%%%%%%%%%%%%%%%%%%%%%%%%%%%%%%
7     phileft1=phileft;
8     phiright1=phiright;
9 else %THIS IS
10    FOR SYMMETRY%
11    phileft1=phiright;
12    phiright1=phileft;
13    Vappx=-Vappx;
14 end %
15    %%%%%%%%%%%%%%%%%%%%%%%%%%%%%%%%%%%%%%%%%%%%%%%%%%%%%%%%%%%%%%%%%%%%%%%%%%
16 dn=thickness1/num;
17 distance=0;
18
19 for (j=1:(num))
20    image(j)=-1.15*(q*0.6931/(8*pi*eps*eps0*thickness))*(
21        thickness1*thickness1/(distance*(thickness1-distance)
22    ));
23    distance=distance+dn;
24 end
25 distance=0;
26
27 for (j=1:(num))
28    barrier(j)=phileft1+((phiright1-phileft1-Vappx)*(
29        distance/thickness1))+image(j);
30    if (j<(num/4)) && (barrier(j)<0)
31        barrier(j)=0;
32    elseif (j>(3*num/4)) && (barrier(j)<=-Vappx)
33        barrier(j)=-Vappx;
34    end
35    distance=distance+dn;
36 end
37 barrierreturn=barrier(ret);
38 end

```